Simulation of the Flows of Incompressible Bingham Fluids using Macroscopic and Mesoscopic Methods

Isothermal and Non-Isothermal Problems

Gholamreza Kefayati

School of Computer Science, Engineering and Mathematics

Flinders University

This dissertation is submitted for the degree of

Doctor of Philosophy

December 2016

I would like to dedicate this thesis to my loving parents and my wife.

Declaration

I certify that this thesis does not incorporate without acknowledgment any material previously submitted for a degree or diploma in any university; and that to the best of my knowledge and belief it does not contain any material previously published or written by another person except where due reference is made in the text.

Gholamreza Kefayati

December 2016

Acknowledgements

I would like to express my deep gratitude to my supervisor, Professor Raja Huilgol, for his guidance, encouragement and supervision throughout my study. I would also like to point out that his help was essential for carrying out my PhD and the research for the scientific papers.
I am very grateful to Flinders University for supporting my PhD by an International Postgraduate Research Scholarship (IPRS) and Australian Postgraduate Award (APA). I also would like to thank the entire staff of Flinders University for their help and support.
I extend my sincere appreciation to Dr. Reza Hashemi Oskouei and Prof. Mark Taylor for their help, advice and useful discussions throughout my studies in Flinders University.
I am deeply grateful to my dear friends, Hamidreza Farhoudi, Khosro Fallahnezad and Asghar Moeini at Flinders University.
Finally and certainly very importantly, I wish to gratefully acknowledge my parents, my brothers and my loving wife for their endless love and their constant patience and support. Thank you all, it could not have happened without you.

Abstract

The incompressible Bingham fluid can be found in various chemical, metal, and food industries, e.g., margarine, mayonnaise and ketchup. The flow field of a Bingham fluid is divided into two regions: the first is an unyielded zone where the fluid is at rest or undergoes a rigid motion, and the second where the fluid flows like a viscous liquid. In the unyielded zone, the second invariant of the extra stress tensor is less than or equal to the yield stress and a constitutive relation does not exist. In the yielded region, this invariant exceeds the yield stress and a constitutive relation exists for the extra stress tensor. Thus, the location and shape of the yield surface(s), i.e., the interface between these two sets, is also a part of the solution of flow problems of such fluids. The hydrodynamic and thermal effects are two interesting aspects arising in the research of the flows of incompressible Bingham fluids. This thesis is concerned with macroscopic and mesoscopic numerical investigations of isothermal (lid-driven cavity, steady flow in a pipe) and non-isothermal (natural convection in an enclosure and mixed convection in a lid-driven cavity) problems of Bingham fluids. Firstly, a general mesoscopic method based on Lattice Boltzmann Method (LBM) is derived which can be applied to all fluids, whether they be Newtonian, or power law fluids, or viscoelastic or viscoplastic fluids. In fact, an innovative model for the distribution functions, which leads to the conservation of mass, momentum, and energy equations, and applicable to incompressible fluids without any drawbacks, is introduced. The Finite Difference Lattice Boltzmann Method (FDLBM) and the Thermal Difference Discrete Flux Method (TDDFM) are derived, using vector analysis and linear algebra. The applied algorithm for solving the main equations of

the discrete particle distribution function in the FDLBM and the internal energy distribution function in the TDDFM is explained. The required equations for compressible fluids are also derived and thereafter the method is extended to the flows of every type of fluid, compressible or incompressible, in three dimensions. In addition, the Courant-Friedrichs-Lewy (CFL) condition for the method is derived. The mesoscopic and macroscopic numerical methods for the cited isothermal and non-isothermal problems are described in detail, using the Bingham model and also a regularisation based on the Papanastasiou model. The lid-driven cavity flow and the steady flow in a pipe have been studied by other researchers before, employing ALM (Augmented Lagrangian Method) and OSM (Operator Splitting Method) respectively and the obtained results by the mesoscopic method in the problems are compared with them. In the case of the natural convection in a cavity, the problem had not been considered at the start of the thesis by other researchers and therefore this problem has been solved by applying the OSM to the Bingham model. Thereafter, the mesoscopic method has been applied to the non-isothermal problem to simulate the natural convection in a cavity and mixed convection in a lid-driven cavity, employing the Bingham and regularised Papanastasiou models.

Publications

The following is a list of publications related to the thesis; see Appendix B.

1. Huilgol, R. R., Kefayati. G. H. R., “Natural convection problem in a Bingham fluid using the operator-splitting method”. Journal of Non-Newtonian Fluid Mechanics 220 (2015) 22-32.

2. Huilgol, R. R., Kefayati. G. H. R., “From Mesoscopic Models to Continuum Mechanics: Newtonian and Non-Newtonian Fluids”. Journal of Non-Newtonian Fluid Mechanics 233 (2016) 146-154.

3. Kefayati. G. H. R., Huilgol, R. R. “Lattice Boltzmann Method for simulation of mixed convection of a Bingham fluid in a lid-driven cavity”. International Journal of Heat and Mass Transfer 103 (2016) 725-743.

Table of contents

List of figures

List of tables

Chapter 1

Introduction

1.1 Background

1.1.1 Extra stress tensor

Stress is a measure of the forces transmitted when external forces are applied to a continuous medium, whether it be a liquid or a solid. These forces are classified into two groups: body forces and surface forces (contact forces). Body forces are applied on the elements of mass like gravity and have the units force per mass. The contact forces act on the surface and are expressed in stresses, i.e., in force per unit area. As a result, there are nine stresses including three stresses (two shear stresses and a normal stress) in each of the x, y and z planes which form the stress tensor ($\mathbf{T}$); for example see Kennedy and Zheng (2013). Since there are no body couples and couple stresses, this tensor is symmetric. In an incompressible fluid at rest, the stress tensor is isotropic and given by (Huilgol (2009)):

$$\mathbf{T} = -p\mathbf{1} \ , \tag{1.1}$$

where p is the pressure.

Additional stresses are generated as the fluid moves and the extra stress term must be added to the pressure:

$$\mathbf{T} = -p\mathbf{1} + \boldsymbol{\tau}. \tag{1.2}$$

Note that $\mathbf{1} : \boldsymbol{\tau} = 0$ is true for all of the fluids studied in this thesis. Thus, the pressure is uniquely defined as follows:

$$p = -(1/3)\mathbf{1} : \mathbf{T}. \tag{1.3}$$

The tensor $\boldsymbol{\tau}$ is called the extra stress tensor in incompressible material and can depend on the unique pressure (p) as well (Huilgol (2009)). The extra stress tensor ($\boldsymbol{\tau}$) must be computed from the constitutive equation when the motion is known, and the traction is either prescribed or calculated from the momentum equations and the applied boundary conditions.

1.1.2 The rate of deformation tensor

The motion of a fluid is in three forms of velocity, deformation, and rotation. From the velocity vector, the deformation and rotation of the fluid are determined from the velocity gradient tensor. The velocity gradient tensor $\mathbf{L}$ is defined through

$$L_{ij} = \frac{\partial v_i}{\partial x_j}. \tag{1.4}$$

The velocity gradient tensor is decomposed into a symmetric part (The rate of deformation tensor ($\mathbf{D}$)), defined through

$$\mathbf{D} = \frac{1}{2}(\mathbf{L} + \mathbf{L}^T). \tag{1.5}$$

The anti-symmetric part, which is called the spin tensor ($\mathbf{W}$), is defined through

$$\mathbf{W} = \frac{1}{2}(\mathbf{L} - \mathbf{L}^T). \tag{1.6}$$

There is another kinematic tensor utilised in the extra tensor of some fluids. It is the first Rivlin-Ericksen tensor (Rivlin and Ericksen (1955)) and is equal to

$$\mathbf{A_1} = 2\mathbf{D} = \mathbf{L} + \mathbf{L}^T. \tag{1.7}$$

Later on, we will use the first Rivlin-Ericksen tensor in the definition of the constitutive equation of the Bingham fluid.

We study incompressible flows only here, and the velocity field and the Rivilin-Ericksen tensor must satisfy

$$\nabla \cdot \mathbf{v} = 0, \quad \text{tr}\, \mathbf{A_1} = \mathbf{A_1} : \mathbf{1} = 0. \tag{1.8}$$

1.1.3 Newtonian and non-Newtonian fluids

Generally, fluids are classified into two main groups: Newtonian and non-Newtonian fluids. In most fluids without memory, the main difference between Newtonian and non-Newtonian fluids is the relationship between the extra stress tensor ($\boldsymbol{\tau}$) and the rate of strain tensor ($\mathbf{D}$), or the first Rivlin-Ericksen tensor ($\mathbf{A_1} = 2\mathbf{D}$)). The constitutive equation of an incompressible Newtonian fluid is written in the following form:

$$\boldsymbol{\tau} = 2\eta\mathbf{D} = \eta\mathbf{A_1}\,, \tag{1.9}$$

where η is the viscosity. Eq.(1.9) shows that the extra tensor has a linear relation with the rate of deformation tensor or the first Rivlin-Ericksen tensor.

1.1.4 Bingham fluids

Viscoplastic fluids form a special sub-class of non-Newtonian fluids in which the flow field is divided into two regions: the first is an unyielded zone where the fluid is at rest or undergoes

a rigid motion, and the second where the fluid flows like a viscous liquid (Bingham (1922)). In the unyielded zone, the second invariant of the extra stress tensor is less than or equal to the yield stress and a constitutive relation is undefined. In the yielded region, this invariant exceeds the yield stress and a constitutive relation exists for the extra stress tensor. Thus, the location and shape of the yield surface(s), i.e. the interface between these two sets, is also a part of the solution of flow problems of such fluids. Viscoplastic fluids occur in various chemical, metal, and food industries, e.g., margarine, mayonnaise and ketchup. Viscoplastic models include the Bingham model, Herschel-Bulkley model, and the Casson model.

The constitutive equation of an incompressible Bingham fluid is based on the assumption that the fluid remains at rest or moves as a rigid body if the second invariant of the extra stress tensor $\boldsymbol{\tau}$ is less than or equal to the yield stress τ_y. If the second invariant exceeds the yield stress, the material flows like a fluid. The second invariants of the extra stress tensor $\boldsymbol{\tau}$ and the first Rivlin-Ericksen tensor $\mathbf{A}_1$ are defined through

$$II(\boldsymbol{\tau}) = (1/\sqrt{2})\sqrt{\boldsymbol{\tau} : \boldsymbol{\tau}}\,, \tag{1.10}$$

$$II(\mathbf{A}_1) = (1/\sqrt{2})\sqrt{\mathbf{A}_1 : \mathbf{A}_1}\,\cdot \tag{1.11}$$

Hence, using the first Rivlin-Ericksen tensor $\mathbf{A}_1$, the rigidity condition is given by

$$\mathbf{A}_1 = \mathbf{0}, \quad II(\boldsymbol{\tau}) \leq \tau_y. \tag{1.12}$$

When the second invariants of the extra stress tensor exceeds the yield stress, one defines the Bingham stress tensor $\boldsymbol{\tau}$ as a function of the tensor $\mathbf{A}_1$ leading to the following relation:

$$\boldsymbol{\tau} = \eta\mathbf{A}_1 + \frac{\tau_y}{II(\mathbf{A}_1)}\mathbf{A}_1, \quad II(\boldsymbol{\tau}) > \tau_y. \tag{1.13}$$

1.1.5 Different models of Bingham fluids

The simulation of the flows of a Bingham fluid is a challenging problem and researchers have proposed and applied various models (Mitsoulis (2007)) to simulate these flows and the studies into this topic continue to attract a great deal of interest. The models can be divided into using the strict Bingham model and several different modifications. In the strict Bingham model, there is a transition from solid to fluid behaviour; whereas in all other regularized models, it is replaced by a very viscous to viscous transition.

Bingham model for Dirichlet problems

Duvaut and Lions (1972, 1976) demonstrated that variational inequalities (VIs) are appropriate methods for steady and unsteady flow problems in incompressible Bingham fluids. They also proved the existence of a symmetric second order tensor field throughout the flow domain under Dirichlet boundary conditions. This tensor, called a multiplier (the $\mathbf{\Lambda}$ in (1.14)) , is such that its 'magnitude' is less than one where the Bingham fluid exhibits rigidity and equal to one where it has yielded. The solution of the flow problems employs the Augmented Lagrangian Method (ALM) (Fortin and Glowinski (1983); Glowinski (1984)), or the Operator Splitting Method (OSM) (Dean and Glowinski (2002); Huilgol and You (2009); Sanchez (1998)) to solve different flow problems in Bingham fluids. The constitutive equation of a Bingham fluid in this model is as follows:

$$\mathbf{T} = \eta \mathbf{A}_1 + \sqrt{2}\tau_y \mathbf{\Lambda}, \quad \mathbf{1} : \mathbf{\Lambda} = 0. \tag{1.14}$$

The properties and the application of the tensor $\mathbf{\Lambda}$ for different problems will be discussed in chapters 4 and 5 in detail.

Papanastasiou model

Papanastasiou (1987) proposed an exponential regularisation, by introducing a parameter m, which controls the exponential growth of stress and has the dimension of time. In addition, it is applicable in all regions, both in yielded and unyielded parts. In the Papanastasiou model, the constitutive equation of the incompressible Bingham fluid is replaced by that of a material with a non-Newtonian viscosity. That is,

$$\boldsymbol{\tau} = \eta(II(\mathbf{A}_1))\mathbf{A}_1, \tag{1.15}$$

where the viscosity η is the sum of the constant Newtonian viscosity η_0, and the parameter (m) dependent term. To be specific,

$$\eta(II(\mathbf{A}_1)) = \eta_0 + \frac{\tau_y}{II(\mathbf{A}_1)}\left[1 - \exp(-mII(\mathbf{A}_1))\right],\ m > 0, \tag{1.16}$$

where $m > 0$ is a parameter which can be chosen arbitrarily. Note that the viscosity function in Eq.(1.16) is a smooth function of its argument. As far as numerical modelling is concerned, one can employ Eq.(1.16) and choose an appropriate value for the parameter m. A search through the literature shows that m can be between 0.1 and 10^6.

Bercovier and Engelman model

Bercovier and Engelman (1980) analyzed a Bingham fluid in a two dimensional lid-driven cavity, applying a different type of regularisation. However, the model did not have the ability to define the yielded/unyielded sections clearly. They proposed a regularisation parameter (The e in 1.17) which is very small and prevents the denominator of the fraction to become zero. The proposed constitutive equation is

$$\boldsymbol{\tau} = \eta \mathbf{A}_1 + \frac{\tau_y}{II(\mathbf{A}_1) + e}\mathbf{A}_1, \quad II(\boldsymbol{\tau}) > \tau_y. \tag{1.17}$$

As $e \to 0$, this model turns into the Bingham fluid.

O'Donovan and Tanner model

O'Donovan and Tanner (1984) regularized the Bingham model with the so-called bi-viscosity model, having two finite viscosity slopes. The model is written as

$$\boldsymbol{\tau} = \eta_{yield}\mathbf{A}_1, \quad II(\mathbf{A}_1) \leq \frac{\tau_y}{\eta_{yield}}. \tag{1.18}$$

$$\boldsymbol{\tau} = \tau_y + \eta(\mathbf{A}_1 - \frac{\tau_y}{\eta_{yield}}), \quad II(\mathbf{A}_1) > \frac{\tau_y}{\eta_{yield}} \tag{1.19}$$

where η_{yield} and η are the yield stress and the plastic viscosity, respectively. In fact, this model replaces the unyielded material by a fluid of high viscosity. Thus, the nature of the solid - fluid transition is lost as well.

In this thesis, we study the Bingham model and the Papanastasiou model in isothermal and non-isothermal flow problems.

1.1.6 Lattice Boltzmann Method

Lattice Boltzmann Method (LBM), unlike macroscopic numerical methods; based on LBM, which are based on discretization of macroscopic continuum equations (FEM, FVM, FDM, and so on), and unlike molecular dynamics methods, which are based on atomic representation with molecular collision rules, is based both on microscopic models and mesoscopic kinetic equations. Currently, LBM is recognized as another powerful method in the Computational Fluid Dynamics (CFD) area. This method has been applied to various problems of fluid

dynamics and has delivered effective and appropriate results. Nevertheless, improvement in the method is continuing in order to augment its ability to solve more complicated problems. The derivation of the LBM is based on the Lattice Gas Cellular Automata (LGCA), first presented by Hardy et al. (1973). The LGCA contains two steps: streaming and collision. In streaming, each particle moves to the nearest node in the direction of its velocity. As particles arrive at a node, collisions occur and their velocities change directions according to scatter rules. However, this does not lead to Cauchy equations for a continuous medium in the macroscopic limit. This problem was resolved by Frisch et al. (1987, 1986) who proposed a higher symmetry hexagonal lattice model than the square lattice model of Hardy et al. (1973). Even so, the LGCA suffered from statistical noise which prevented researchers from employing it practically.

The nature of LBM is similar to LGCA and has been formed from the mentioned two steps of LGCA (streaming and collision). However, LBM differs from LGCA in that instead of Boolean variables representing particle occupation at the nodes, LBM uses a single-particle distribution. This particle distribution denotes the density or the number per unit volume of particles. LBM benefits from this replacement due to the elimination of statistical noise. The cited issues were identified and corrected by McNamara and Zanetti (1988) in their work on LBM. The equations and further studies in LBM are mentioned in the third chapter in detail.

1.2 Objective

The main objective of this thesis is to introduce a mesoscopic numerical method based on LBM which can solve a variety of isothermal and non-isothermal flow problems of a Bingham fluid. In addition, previous successful macroscopic numerical methods for Bingham fluids are also examined. The relations between the mesoscopic and macroscopic variables will be mentioned clearly and the main reason, in contrast with the previous applied LBM, that the new approach can be successful in the simulation of isothermal and non-isothermal

flows of Bingham fluids, is stated in this thesis. In addition, it is demonstrated that the mesoscopic numerical method has the ability to be applied to the Bingham model as well as the different regularised models. Hence, two important and widely studied isothermal problems (steady flow in a lid-driven cavity and in a pipe of square cross-section) and a non-isothermal problem (natural convection in a cavity) for Bingham fluids were selected to be scrutinized by both macroscopic and mesoscopic numerical methods. The previously solved isothermal Bingham fluid flow problems in a lid-driven cavity and in a pipe of square cross-section flows using the OSM (Operator Splitting Method) and the ALM (Augmented Lagrangian Method), respectively are studied and next, the mesoscopic method is applied to these problems, comparing the obtained results with the cited macroscopic methods. For the natural convection of Bingham fluids in a cavity, the macroscopic method based on the OSM, has been used for the first time in this thesis. It provides a validation of the mesoscopic results. In the next step, the results of the mesocopic simulation of isothermal and non-isothermal flows of Bingham fluids have been compared with the ALM and OSM results. Finally, the mixed convection of a Bingham fluid in a lid-driven cavity using the modified model of Papanastasiou is studied using the mesoscopic method.

1.3 Outline of the thesis

This thesis is divided into the following chapters:

Chapter Two

This chapter contains a review of the previous studies into four scrutinized problems in this thesis, using macroscopic and mesoscopic methods. First, the flow in a lid-driven cavity and that in a pipe using different macroscopic methods are discussed. In the next step, the work done on non-isothermal problems of natural convection of Bingham fluids in a cavity, utilising different numerical methods is mentioned as well as the previous work on mixed convection of Bingham fluid in a cavity. Finally, the simulations of the flows of Bingham fluids in several problems, applying mesoscopic methods, are reported to clarify the limited studies in this area.

Chapter Three

A brief introduction about the history of the Lattice Boltzmann equation and the Bhatnagar–Gross–Krook (BGK) approximation in order to derive Cauchy's equations of motion for a compressible medium is explained. In addition, the method of deriving the incompressible equations, using the BGK approximation and the main drawbacks of the method including the weakness in simulation of non-Newtonian fluids flows are described. Hence, an innovative model for the distribution functions, which leads to the conservation of mass, momentum, and energy equations, and applicable to incompressible fluids without the cited drawbacks, is introduced. The Finite Difference Lattice Boltzmann Method (FDLBM) and the Thermal Difference Discrete Flux Method (TDDFM) are derived, using vector analysis

and linear algebra. The applied algorithm for solving the main equations of the discrete particle distribution function in the FDLBM and the internal energy distribution function in the TDDFM is explained. The required equations for compressible fluids are also derived and thereafter the method is extended to the flows of every type of fluid, compressible or incompressible, in three dimensions. Finally, the Courant-Friedrichs-Lewy (CFL) condition for the method is derived.

Chapter Four

In this chapter, isothermal flows of Bingham fluids in two different problems are studied. In the first case, the flow inside a lid-driven cavity is simulated. First, the Newtonian fluid in the lid-driven cavity, employing the mesoscopic method, is scrutinized and the obtained results are compared with those of previous studies to confirm the accuracy of the mesoscopic method. Thereafter, the OSM for the simulation of the flow of the Bingham fluid in the lid-driven cavity, which had been investigated by others, is explained. This flow in the cavity, using the Bingham and the Papanastasiou models is simulated, applying the mesoscopic method and the results are verified by previous investigations for the both models. In the second case, the steady flow of a Bingham fluid in a pipe of square cross-section is studied. In the first step, the ALM, which was applied to solve the problem by other researchers, is defined. Then, the mesoscopic method is applied to simulate the problem, employing the Bingham model and the results are validated by those obtained by ALM.

Chapter Five

Non-isothermal flows of Bingham fluids are studied in two different problems. The first

problem is the natural convection of a fluid in a cavity. The flow of the Newtonian fluid is simulated, using the mesoscopic method and the accuracy of the method is confirmed by previous studies. Next, the OSM is employed to simulate the flows of Bingham fluids in the natural convection for a wide range of non-dimensional parameters where the Bingham model is applied. In the following part, the mesoscopic results in the natural convection of the Bingham fluid flow, using the Bingham and Papanastasiou models are compared with those derived by OSM. The second non-isothermal problem is the mixed convection of a Bingham fluid in a lid-driven cavity. The mesoscopic method is applied to study the mixed convection of the Bingham fluid, applying the Bingham and the Papanastasiou models.

Chapter 2

Literature Review

2.1 Introduction

In this chapter, a brief description of the previous studies into Bingham fluids for two isothermal (steady flow in a pipe and in a lid-driven cavity) and two non-isothermal (natural convection and mixed convection) problems are given.

The steady flow of a Bingham fluid in a pipe is important in understanding the effects of yielded/unyielded zones in the velocity profile. Hence, several studies into this topic have been conducted.

The lid-driven flow in a cavity is the motion of a fluid inside a rectangular cavity created by a constant translational velocity of one side while the other sides remain at rest. Such a flow has been the subject of extensive computational and experimental studies over the past few years and many studies into a lid-driven cavity filled with a Newtonian fluid have been conducted (Ghia et al. (1982), Botella and Peyret (1998), Bruneau and Jouron (1990), Deng et al. (1994), Sahin and Owens (2003), Hou et al. (1995)). The flow in a lid-driven cavity has been used as a benchmark problem for many numerical methods as it covers a wide range of complex hydrodynamics encompassing recirculation, different vortex structures, singularity, transition and instability.

Analysis of natural convection in enclosures has been extensively conducted using different numerical techniques and experiments because of its wide applications and interest in engineering such as nuclear energy, double pane windows, heating and cooling of buildings, solar collectors, electronic cooling, and so on. The wide range of studies into this topic has led to the natural convection in a cavity to become a common benchmark among researchers in the field of CFD (Computational Fluid Dynamics). It consists of a two-dimensional cavity and the temperature of the heated section on the left is maintained at a higher temperature and the right wall is held at a lower temperature. The horizontal walls are considered to be adiabatic and the density variation is approximated by the standard Boussinesq model. The natural convection flow of a Newtonian fluid has been studied numerically by de Vahl Davis (1983), Quéré and de Roquefort (1985), Quéré (1991).

Convection involving both free and forced convection is generally referred to as mixed convection, which occurs when the buoyancy effects are superposed on a forced flow. Mixed convection in a fluid-filled square cavity plays an important role in the area of heat and mass transfer and has also been given a considerable attention over the past several years due to the wide variety of its applications in science and engineering (Waheed (2009), Iwatsu et al. (1993), Khanafer and Chamkha (1999), Sharif (2007), Khanafer et al. (2007), Tiwari and Das (2007), Abdelkhalek (2008)). For example, the flow is present in materials processing, flow and heat transfer in solar ponds, dynamics of lakes, reservoirs and cooling ponds, crystal growing, float glass production, metal casting, food processing, galvanizing, and metal coating. However, most of the research has been limited to incompressible Newtonian fluids.

2.2 Macroscopic simulation of Bingham fluids

2.2.1 Steady flows of Bingham fluids in a pipe

Mosolov and Miasnikov (1965, 1966, 1967) analysed mathematically the steady flow of Bingham plastics in a pipe of arbitrary cross-section and proved several existence and uniqueness theorems for the solution. They established the existence of a rigid core region and those of stagnant regions near the corners with convex boundaries toward the corners. They also obtained interesting results for the shape of the unyielded zones in the flow field and the critical value of the pressure gradient below which the flow does not occur.

Atkinson and El-Ali (1992) carried out a local analysis of the pressure-driven Bingham flow near the corners and showed the possible existence of 'plug' regions in the neighbourhood of acute corners.

Huilgol and Panizza (1995) applied variational inequalities to solve the Poiseuille flow of a Bingham plastic through a duct of an L-shaped cross-section. They reported that the stagnant zones are near the acute-angled corners in agreement with the theoretical predictions of Mosolov and Miasnikov (1965, 1966, 1967) and Atkinson and El-Ali (1992).

Taylor and Wilson (1997) solved numerically the flow of a Bingham fluid in rectangular ducts by means of finite differences using the regularisation of the constitutive equation proposed by Bercovier and Engelman (1980). They noted, however, that their numerical scheme could not work for small values of the regularisation parameter. As a consequence, the computed yielded and unyielded regions were not accurate. In addition, they pointed out that in agreement with the theory, that there would be stagnant regions at the corners depending on the flow parameters.

Pham and Mitsoulis (1998) solved the flows of a Bingham plastic in ducts of various cross-sections using the Papanastasiou regularisation. However, their results for the flow in a

square duct were similar to those of Taylor and Wilson (1997) due to the low value of the regularisation parameter employed.

Wang (1998) studied the flow of generalized viscoplastic fluids in a square duct and in an eccentric annulus using the finite element method and tracking the yield surface by means of a regularisation technique based on the theory of variational inequalities. He reported that the plug zones are almost identical for various plastic models despite their different shear-thinning behavior.

Frigaard (1998) considered the buoyancy driven flows of two Bingham fluids in an inclined slot, providing a simplified model for the plug cementing process. These flows were supposed to be near uniaxial and stratified, with the heavier fluid (cement) initially placed above the lighter fluid (mud). Under the action of gravity, the cement slides down the lower wall of the slot displacing the mud upwards, against the upper wall of the slot. The fluids were assumed to be miscible, but not mixed. The perturbation solutions were utilised to analyze the axial propagation of the interface height profile along the slot.

Accurate solutions of the steady Poiseuille flow of a Bingham fluid in a square duct were obtained by Saramito and Roquet (2001) by means of a new mixed anisotropic auto-adaptive finite element method, coupled with the Augmented Lagrangian Method (ALM). It was found that calculating the location of the yield surface was not precise.

Huilgol and You (2005) applied the Augmented Lagrangian Method to the steady flow problems of Bingham, Casson and Herschel-Bulkley fluids in pipes of circular and square cross-sections.The plug flow velocity, the flow rate, the flow pattern, the velocity profile, the locations of yielded/unyielded surfaces, the stopping criteria and the friction factor were presented.

Huilgol (2006) developed a systematic procedure to determine the critical pressure gradient for the initiation of viscoplastic flow as well as the shape of the yield surface when the flow is about to commence in pipes of symmetric cross-section, such as a rectangle.

It was also shown that the Mosolov–Miasnikov approach (Mosolov and Miasnikov (1965, 1966, 1967)) can be applied to all viscoplastic fluids with a constant yield stress, such as Herschel-Bulkley and Casson fluids.

Moyers-Gonzalez and Frigaard (2004) studied the numerical solution of the flows in a duct of multiple visco-plastic fluids using both the regularisation technique and the Augmented Lagrangian Method (ALM). They demonstrated that the ALM was superior for the studied problem.

Damianou and Georgiou (2014) solved numerically the Poiseuille flow of a Herschel Bulkley fluid in a duct of rectangular cross section under the assumption that slip occurs along the wall, using a slip law involving a non-zero slip yield stress. The constitutive equation was regularized as proposed by Papanastasiou (1987). They studied four different flow regimes defined by three critical values of the pressure gradient. Both Newtonian and Bingham fluid flows were investigated. They compared their results with theoretical and numerical results in the literature obtained with both the regularisation and the Augmented Lagrangian Method. They reported that the unyielded regions were found accurately using the Papanastasiou model, but the regularisation parameter should be sufficiently high, of the order of 10^6 or higher.

Damianou et al. (2015) simulated numerically the cessation of the pressure driven Poiseuille flow of a Bingham plastic under the assumption that slip occurs along the wall following a generalized Navier-slip law involving a non-zero slip yield stress.The constitutive and the slip equations were regularized by using the Papanastasiou model.

2.2.2 Lid-Driven cavity flows of Bingham fluids

Sanchez (1998) employed a first order operator splitting method (OSM) for the solution of the time dependent variational inequality modeling of Bingham fluids in a lid-driven cavity. This work included acceleration terms as well and is a benchmark study.

Mitsoulis and Zisis (2001) studied the same problem. The Bingham constitutive equation was modified by the Papanastasiou model (Papanastasiou (1987)). The constitutive equation was solved together with the conservation equations using the finite element method (FEM) as the Bingham number varied between Bn = 0 and 1000. It should be noted that just the creeping flow of the fluid (Re = 0) was conducted in this study.

Dean and Glowinski (2002) studied computational methods for numerical simulation of the unsteady flow of Bingham viscoplastic fluids in a lid-driven cavity. The operator splitting method was utilised for the time-discretization.

Neofytou (2005) investigated the flow of non-Newtonian fluids with generalised Newtonian constitutive equations using a numerical scheme based on the finite volume formulation. Among the studied non-Newtonian fluids, the modified and regularized Bingham model based on the Papanastasiou model (Papanastasiou (1987)) was analysed in a lid-driven cavity.

Vola et al. (2003) proposed a numerical method to calculate the unsteady flows of Bingham fluids without any regularisation of the constitutive law in a lid-driven cavity. The strategy was based on the combination of the characteristic/Galerkin method to cope with convection and of the Fortin–Glowinski decomposition/coordination method (Fortin and Glowinski (1983)) to deal with the non-differentiable and nonlinear terms that derive from the constitutive law. The results were presented for both creeping and non-creeping flows.

Huilgol and You (2009) studied the flows of incompressible and compressible Bingham fluids in a lid-driven cavity, using the Bingham model for the constitutive equation and the operator-splitting method was applied to solve the problem. Here, variational inequalities for incompressible viscoplastic fluids depending largely on the existence of the viscoplastic constraint tensor were used.

Olshanskii (2009) applied the semi-staggered finite-difference method to simulate the flow of a Bingham fluid in a lid-driven cavity using the Bingham model. A special stabilization was introduced to achieve optimal approximation properties of the scheme.

Zhang (2010) applied the Augmented Lagrangian Method for Bingham fluid flows in a lid-driven square cavity. Equal-order piecewise linear finite element spaces were employed for both the velocity and pressure approximations. A mesh adaptive strategy was also proposed based on the regularity of the numerical solutions.

Aposporidis et al. (2011) studied and simulated the Bingham fluid flow problem, considering both the Bingham and a regularized model in a lid-driven cavity. They introduced a new formulation for the regularized Bingham flow equations. In addition, their applied mixed formulation was compared to a non-regularized solver based on the Augmented Lagrangian Method.

Santos et al. (2011) investigated the effect of inertia and rheology parameters on the flow of viscoplastic fluids inside a lid-driven cavity using a stabilized finite element approximation. The viscoplastic material behavior was simulated through the de Souza Mendes and Dutra model (Mendes and Dutra (2004)) which is called the SMD fluid. The SMD model is essentially based on a regularized viscosity function involving the rheological properties of the material. The balance equations were coupled with the non-linear SMD model and were approximated by a multi-field Galerkin least-squares method in terms of extra-stresses, pressure and velocity. The numerical simulations were validated through the comparison with the results in the literature for the flows of Bingham fluids.

Syrakos et al. (2013) studied the creeping flow of a Bingham plastic in a lid-driven square cavity as the test case and the constitutive equation was regularised by the Papanastasiou model. They utilised the the standard SIMPLE pressure-correction algorithm, which was used to solve the algebraic system of equations produced by the finite volume discretisation. It was shown that using the SIMPLE algorithm in a multigrid context dramatically improved the convergence, although the multigrid convergence rates were much worse than those for Newtonian fluids. The numerical results were compared with the reported results of other methods. However, they noted that the convergence of the method becomes slow at high

values of the Bingham number and the regularisation parameter. In addition, with the use of a modified multigrid method, convergence was accelerated considerably compared to the single-grid SIMPLE method.

Syrakos et al. (2014) extended their previous work on the creeping flow of a Bingham fluid in a lid-driven cavity to include inertial effects, using a finite volume method and the Papanastasiou regularisation of the Bingham constitutive model. They emphasized that the equations become stiffer and more difficult to solve, while the discontinuity at the yield surfaces causes large truncation errors using the finite volume method (FVM). It was added that by regularising the Bingham constitutive equation, it was easy to extend such a solver to other flows since all that this requires is a modification of the viscosity function. In this study, they attempted to investigate the strengths and weaknesses of this method by applying it to the lid-driven cavity problem for a wide range of Bingham and Reynolds numbers (up to 100 and 5000 respectively). By employing techniques such as multigrid, local grid refinement, and an extrapolation procedure, they reduced the effect of the regularisation parameter on the calculation of the yield surfaces. Nevertheless, it was reported that the weakness of FVM becomes more noticeable with the rise of the Bingham number.

Muravleva (2015) implemented the Uzawa-like algorithm to simulate the flows of a Bingham fluid in a lid-driven cavity and the Bingham model was applied in the simulation. In addition, the operator-splitting method was used, employing different time-discretization and space-discretization. The results for the steady flow problem were verified by comparison with those in the literature for the shape and locations of the yield surface.

2.2.3 Natural convection of Bingham fluids in a cavity

Vola et al. (2003) studied the natural convection in a cavity filled with a Bingham fluid using the Bingham model without any regularisation of the constitutive law. They applied a numerical method based on the combination of the characteristic/Galerkin method to cope

with convection and of the Fortin–Glowinski decomposition/coordination method (Fortin and Glowinski (1983)) to deal with the non-differentiable and nonlinear terms that derive from the constitutive law. However, the streamlines and isotherms for various yield stress values were limited to one value of the Rayleigh number (Ra = 10^4).

Turan et al. (2010) conducted a study into the simulations of natural convection in square enclosures filled with an incompressible Bingham fluid. The considered flow was laminar and steady. The commercial package FLUENT was utilised to solve the problem. In this study, a second-order central differencing scheme was used for the diffusive terms and a second order up-wind scheme for the convective terms. Coupling of the pressure and velocity fields was achieved using the SIMPLE algorithm. It should be noted that the default Bingham model in FLUENT is a bi-viscosity model (O'Donovan and Tanner (1984)). The heat transfer and the flow velocities were investigated over a wide range of Rayleigh and Prandtl numbers. They found that the average Nusselt number augments with the rise of the Rayleigh number for both Newtonian and Bingham fluids, whereas the Nusselt numbers of Bingham fluids were smaller than those in Newtonian fluids for a fixed nominal Rayleigh number. They also mentioned that the mean Nusselt number of Bingham fluids decreased with an increase in the Bingham number. Moreover, it was observed that the conduction dominated regime occurs at large values of Bingham numbers. Finally, they reported that for low Bingham numbers, the mean Nusselt number increases with the enhancement of the Prandtl number; by contrast, the opposite behaviour was observed for large values of Bingham numbers.

Turan et al. (2011) continued their studies with analysing the effect of different aspect ratios (the ratio of the height to the length) of the cavity, adding to their previous results that the average Nusselt number follows a non-monotonic pattern with the aspect ratio for specific values of the Rayleigh and Prandtl numbers for both Newtonian and Bingham fluids. At small aspect ratios, the conduction is dominant whereas convection remains predominantly responsible for the heat transfer for large values of aspect ratios. In addition, it was found

that the conduction dominated regime occurred at higher values of the Bingham numbers for increasing values of the aspect ratio for a given value of the Rayleigh number.

Turan et al. (2012) scrutinised the laminar Rayleigh-Bénard convection of yield stress fluids in a square enclosure. The applied method and the achieved results were similar to the two previous studies.

2.2.4 Mixed convection of Bingham fluids in a lid-driven cavity

No studies into this topic have been found in the literature.

2.3 Mesoscopic simulation of the flows of Bingham fluids

Wang and Ho (2008) presented a lattice Boltzmann method for viscoplastic materials. The technique of the Chapman Enskog multiscale expansion was employed to demonstrate that the proposed method macroscopically matches the governing equations for the flows of a Bingham plastic to the second order. The continuum-based Bingham constitute equation was modified by the Papanastasiou model (Papanastasiou (1987)) with an exponential growth term to make the continuous transitions between both the yielded and unyielded regions. The benchmark problem of an expansion flow in planar channels was studied. However, the relation between the relaxation time and the viscosity limited the study to a specific range of viscosities.

Tang et al. (2011) studied the flow of a Bingham fluid numerically using the Lattice Boltzmann method by incorporating the Papanastasiou regularisation (Papanastasiou (1987)). They employed an incompressible Lattice Boltzmann model based on the proposed model of He-Luo (He and Luo (1997)). They analysed the effect of the regularisation parameter (m) on the simulation of the flow of a Bingham fluid. However, the relationship between the viscosity and the relaxation time restricted the studied viscosity to a limited range.

Ohta et al. (2011) analysed the results of the Lattice Boltzmann (LB) simulations for the planar-flow of viscoplastic fluids through complex shaped channels. The Papanastasiou model was employed in the LB simulations. First, the simple problem of the channel flow between the parallel plates was considered to verify the effectiveness of the LBM with modified viscoplastic models and the validity of the LBM was established for both of the viscoplastic models. Fluid-solid boundary conditions at circular obstacles were handled through the linearly interpolated bounceback scheme.

Vikhansky (2010) considered the problem of the initiation of thermal convection in rectangular cavities filled with viscoplastic material. A two-sided asymptotic expansion was combined with numerical modelling in order to obtain an expression for the critical yield number. In this work, the mass and momentum equations were solved using a Lattice–Boltzmann (LB) method combined with a finite difference method for the energy equation. Nevertheless, the method was not explained in detail and limited results were illustrated since the paper was a short communication.

2.4 Concluding Remarks

The literature review reveals that there are many studies into isothermal problems of Bingham fluids using macroscopic methods. However, in several publications, regularized Bingham models have been usually applied instead of the Bingham model. When the thesis was begun in 2013, no studies into non-isothermal problem of natural convection existed using the Bingham model, while there were some researches into the natural convection of Bingham fluids, employing the bi-viscosity model. Hence, we have studied the natural convection of a Bingham fluid in a cavity, employing the Operator Splitting Method based on the Finite Element Method (Huilgol and Kefayati (2015)) and the Bingham model was used. Thereafter, Karimfazli et al. (2015) analysed the same problem, introducing a novel regulation of heat transfer across a cavity. In addition, the literature review has demonstrated that mesoscopic

simulations of Bingham fluids are rare and limited to some isothermal problems and in all of them regularized models have been employed. As a result, the new mesoscopic method has been applied to simulate the isothermal and non-isothermal flow problems (steady flow in a pipe, lid-driven cavity, natural convection), employing both the Bingham and regularized models and validated by comparison with the previous results of the cited macroscopic methods. Finally, after proving the accuracy of the mesoscopic method, it has been used to solve the mixed convection flow of Bingham fluids using the regularized model.

Chapter 3

From mesoscopic models to continuum mechanics

In this chapter, a review of the BGK approximation to obtain the equations of motion for an incompressible fluid is presented and its drawbacks are revealed. In order to overcome these inherent problems, new models for the particle distribution functions are needed. Using the Finite Difference Lattice Boltzmann Method (FDLBM) due to Fu and So (2009) and the Thermal Difference Discrete Flux Method (TDDFM) proposed by Fu et al. (2012), it is shown that the newer distribution functions lead to the mass conservation equation, the equations of motion and the energy balance equation for incompressible fluids in two dimensions, employing the D2Q9 lattice as the model. This derivation is extended to compressible fluids as well. Next, using the D3Q15 lattice as an example, the three dimensional equations of continuum mechanics are derived. Since no restrictions are placed on the constitutive equations, the theoretical development applies to all fluids, whether they be Newtonian, or power law fluids, or viscoelastic and viscoplastic fluids. Finally, some comments are offered regarding the numerical scheme to calculate the particle distribution functions to determine the velocity and temperature fields.

3.1 Introduction

From the Lattice Boltzmann equation, it is possible to derive the continuity equation and Cauchy's equations of motion for a compressible medium, when one uses the Bhatnagar-Gross-Krook (BGK) approximation. From this, one can obtain equations relevant to incompressible fluids. However, these require that the pressure be proportional to the density and the viscosity be dependent on the collision relaxation time (Guo et al. (2000)); see Section 3.2 below. Clearly, these restrictions on the pressure and the viscosity are unacceptable in modelling the flows of non-Newtonian, incompressible fluids.

In order to overcome these inherent problems, new models for the particle distribution functions are needed. In the Finite Difference Lattice Boltzmann Method (FDLBM) due to Fu and So (2009) , the particle distribution function leads to the conservation of mass and the equations of motion applicable to incompressible fluids, when the flows are assumed to occur in a two dimensional setting underpinned by a D2Q9 lattice. Our derivation of these results is succinct and is more transparent, for it uses vector analysis and linear algebra. In addition, the energy equation is also obtained from the Thermal Difference Discrete Flux Method (TDDFM) proposed by Fu et al. (2012) ; once again, simple results from vector analysis and linear algebra are employed. The important point to note is that the previous restrictions on the pressure and the viscosity are eliminated in these derivations, meaning that one is free to choose a constitutive equation. That is, one can model a Newtonian fluid, or power law fluids, or viscoelastic and viscoplastic fluids. Moreover, we point out in section 3.3 that it is quite easy to incorporate Dirichlet type boundary conditions into the numerical scheme to determine the particle distribution functions for the velocity and temperature fields.

In Section 3.4, the method is extended to the flows of all fluids in three dimensions, using the D3Q15 lattice as an example. Once again, the particle distribution functions are such that every type of fluid, compressible or incompressible, can be employed.

Finally, in Section 3.5, some remarks are offered on the numerical scheme employed to determine the particle distribution functions for the velocity and the temperature fields. The CFL condition for the stability of the numerical scheme is also derived.

3.2 BGK approximation to continuum mechanics

Beginning in 1986, Lattice Boltzmann equation (LBE) models evolved from their Boolean counterparts, viz., the lattice-gas-automata (LGA). The theoretical framework of the LBE was underpinned by the Chapman-Enskog analysis of the LGA models (Frisch et al. (1987, 1986); Wolfram (1986)). That is, the statistical mechanics of the LGA played a crucial role in these developments. A decade later, He and Luo (1997) proved that the LBE is a specific discretised form of the continuous Boltzmann equation using the Bhatnagar-Gross-Krook (BGK) approximation Bhatnagar et al. (1954). As an application, He and Luo (1997) derived the Lattice Boltzmann BGK (LBGK) equation for the D2Q9 lattice model. It is worth noting that Welander (1954) published an approximation to the Boltzmann equation at the same time as BGK and applied it to a rarefied monatomic gas exchanging heat with an adjacent wall. In several aspects, his treatment of this problem is exemplary and anticipates by several decades the subsequent Lattice formulation. However, we shall use the more commonly used acronym LBGK equation in the sequel.

From the LBGK equation, Cauchy's equations of motion for compressible fluids can be derived under the assumption that the Mach number is small and that the density variation is small. Attempts to derive the equations for incompressible fluids from the foregoing end in physically unacceptable requirements, viz., that the pressure be proportional to the density and that the viscosity depends on the collision relaxation time (Guo et al. (2000)).

To render these remarks transparent, let $f = f(\mathbf{x}, \boldsymbol{\xi}, t)$ be the probability of finding a particle with the velocity $\boldsymbol{\xi}$ near the point $\mathbf{x}$ at time t. The Boltzmann equation for this distribution function, in the absence of external forces, is given by

$$\frac{\partial f}{\partial t} + (\nabla f \cdot \boldsymbol{\xi}) + \frac{1}{\lambda} f = N(f), \tag{3.2.1}$$

where $\boldsymbol{\xi}$ is the microscopic velocity, λ is the relaxation time due to collision and $N(f)$ is a measure of the net number of molecules which disappear from the region due to intermolecular collisions; see Welander (1954), for example. This is not applied to the problem at hand, for it depends upon an approximation to this measure of collisions; see Eq.(3.2.3) below.

The macroscopic variables are the density of mass ρ, the velocity field $\mathbf{u}$ and the absolute temperature T. These are related to the distribution function f through the following integrals in momentum space:

$$\rho = \int f \, d\boldsymbol{\xi}, \quad \rho \mathbf{u} = \int \boldsymbol{\xi} f \, d\boldsymbol{\xi}, \quad \rho \varepsilon = \frac{1}{2} \int |\boldsymbol{\xi} - \mathbf{u}|^2 f \, d\boldsymbol{\xi}, \tag{3.2.2}$$

where $\varepsilon = DRT/2$, with D being the number of degrees of freedom of a particle and R is the ideal gas constant. Note that we have used $d\boldsymbol{\xi} = d\xi_1 \cdots d\xi_D$, where $D \in [2,3]$ stands for the dimension of the physical space.

In the BGK approximation, the collision operator is assumed to be given by $N(f) = g(\mathbf{u}, \boldsymbol{\xi})/\lambda$, where the collision function $g(\mathbf{u}, \boldsymbol{\xi})$ has the form:

$$g(\mathbf{u}, \boldsymbol{\xi}) = \frac{\rho}{(2\pi RT)^{D/2}} \exp\left[-\frac{|\boldsymbol{\xi} - \mathbf{u}|^2}{2RT} \right]. \tag{3.2.3}$$

Next, using (3.2.3) and integrating (3.2.1) formally over a time interval $\triangle t$ with e^t/λ as the integrating factor, one obtains He and Luo (1997):

$$\begin{aligned} f(\mathbf{x} + \boldsymbol{\xi} \triangle t, \boldsymbol{\xi}, t + \triangle t) &= e^{-\triangle t/\lambda} f(\mathbf{x}, \boldsymbol{\xi}, t) \\ &+ \frac{1}{\lambda} e^{-\triangle t/\lambda} \int_0^{\triangle t} e^{t'/\lambda} g(\mathbf{x} + \boldsymbol{\xi} t', \boldsymbol{\xi}, t + t') \, dt'. \end{aligned} \tag{3.2.4}$$

Assuming that the time interval $\triangle t$ is small enough and linearising in terms of this time interval, one has:

$$f(\mathbf{x}+\boldsymbol{\xi}\triangle t,\boldsymbol{\xi},t+\triangle t)-f(\mathbf{x},\boldsymbol{\xi},t)=-\frac{1}{\tau}[f(\mathbf{x},\boldsymbol{\xi},t)-g(\mathbf{u},\boldsymbol{\xi})], \tag{3.2.5}$$

where $\tau=\lambda/\triangle t$ is the non-dimensional relaxation time. Next, suppose that the collision function $g(\mathbf{u},\boldsymbol{\xi})$ can be expanded as a Taylor series in $\mathbf{u}$, retaining terms up to order $|\mathbf{u}|^2$. Identifying this as the equilibrium distribution function $f^{(0)}$, the following can be derived from (3.2.1):

$$f^{(0)}=\frac{\rho}{(2\pi RT)^{D/2}}\exp(-|\boldsymbol{\xi}|^2/2RT)\left[1+\frac{\boldsymbol{\xi}\cdot\mathbf{u}}{RT}+\frac{(\boldsymbol{\xi}\cdot\mathbf{u})^2}{2(RT)^2}-\frac{|\mathbf{u}|^2}{2RT}\right]. \tag{3.2.6}$$

To derive Cauchy's equations of motion for a continuous medium, exact evaluation of the following momentum integrals

$$I=\int|\boldsymbol{\xi}|^m f^{(0)}\,d\boldsymbol{\xi}=\int\exp(-|\boldsymbol{\xi}|^2/2RT)\psi(\boldsymbol{\xi})\,d\boldsymbol{\xi},\quad m=0,1,2, \tag{3.2.7}$$

is required. Using a Cartesian coordinate system and noting that the physical dimension of the space $D=2$, one can express the microscopic velocity as $\boldsymbol{\xi}=(\xi_x,\xi_y)$. Using this, $\psi(\boldsymbol{\xi})$ is expressed as a polynomial of the form $\psi(\boldsymbol{\xi})=\xi_x^r\xi_y^s$.

The integrals in (3.2.7) can be evaluated through a Gaussian-type quadrature (Davis and Rabinowitz (1984)) and lead to

$$I=\sum_\alpha W_\alpha\exp(-|\boldsymbol{\xi}_\alpha|^2/2RT)\psi(|\boldsymbol{\xi}_\alpha|), \tag{3.2.8}$$

where W_α are the weights and $\boldsymbol{\xi}_\alpha$ are the discrete velocities of the quadrature. In the D2Q9 model, there are nine discrete velocities: $\{\boldsymbol{\xi}_\alpha,\ \alpha=0,1,\cdots,8\}$. The configuration space is discretised into a square lattice with a lattice constant $\triangle x=\sqrt{3RT}\ \triangle t$. In fact, in an

isothermal problem, the temperature T has no physical significance and thus, one can choose $\triangle x$ as a fundamental quantity instead, leading to $\sqrt{3RT} = c = \triangle x/\triangle t$, where the lattice speed c is related to the speed of sound c_s through $c^2 = 3c_s^2$. Thus, $RT = c_s^2 = c^2/3$.

The nine lattice points are located at the centre of the lattice, at the four midpoints of the edges of the square and at the four vertices. One identifies $\alpha_0 = (0,0)$ as the centre of the lattice, $\{\alpha_1, \alpha_3, \alpha_5, \alpha_7\}$ as the midpoints of the four sides: $(\pm 1, 0), (0, \pm 1)$, and $\{\alpha_2, \alpha_4, \alpha_6 \alpha_8\} = (\pm 1, \pm 1)$ as the vertices. The lattice velocity vector at the centre is given by $\boldsymbol{\xi}_0 = \mathbf{0}$. Next, the velocities for $\alpha = 1,3,5,7$, have the form $c(\pm 1, 0), c(0, \pm 1)$, and for $\alpha = 2,4,6,8$, they have the form $c(\pm 1, \pm 1)$. In other words, except at the centre, at each lattice point $\alpha_j, j = 1, \cdots, 8$, the velocity vector points away from the lattice in the direction from α_0 to α_j.

The weights W_α in (3.2.8) can now be computed through quadrature and one obtains (He and Luo (1997)):

$$W_\alpha = 2\pi RT \exp(|\boldsymbol{\xi}_\alpha|^2/2RT) w_\alpha, \tag{3.2.9}$$

where

$$w_\alpha = \begin{cases} 4/9, & \alpha = 0, \\ 1/9, & \alpha = 1,3,5,7, \\ 1/36, & \alpha = 2,4,6,8. \end{cases} \tag{3.2.10}$$

The equilibrium distribution function for the D2Q9 model is given by

$$f_\alpha^{(0)} = \rho w_\alpha + \rho \mathbf{s}_\alpha(\mathbf{u}(\mathbf{x}, t)), \tag{3.2.11}$$

where

$$s_\alpha(\mathbf{u}) = w_\alpha \left[\frac{3(\boldsymbol{\xi}_\alpha \cdot \mathbf{u})}{c^2} + \frac{9(\boldsymbol{\xi}_\alpha \cdot \mathbf{u})^2}{c^4} - \frac{3|\mathbf{u}|^2}{2c^2} \right], \tag{3.2.12}$$

with

$$\boldsymbol{\xi}_\alpha = \begin{cases} (0,0), & \alpha = 0, \\ c(\cos\theta_\alpha, \sin\theta_\alpha) & \alpha = 1,3,5,7, \\ c\sqrt{2}(\cos\theta_\alpha, \sin\theta_\alpha), & \alpha = 2,4,6,8. \end{cases} \tag{3.2.13}$$

Here, the angles θ_α are defined through $\theta_\alpha = (\alpha-1)\pi/4,\ \alpha = 1,\cdots,8.$

Introducing a Mach number $\mathrm{M} = |\mathbf{u}|/c_s$, one can see that the equilibrium distribution function can be written in the form:

$$f_\alpha^{(0)} = f_\alpha^0 + \mathrm{M} f_\alpha^1 + \mathrm{M}^2 f_\alpha^2, \tag{3.2.14}$$

where

$$f_\alpha^0 = \rho w_\alpha, \quad f_\alpha^1 = \rho w_\alpha. \tag{3.2.15}$$

Assuming that the distribution function f_α can be found from the equation corresponding to (3.2.5), the momentum space integrals in (3.2.2) lead to the following results for the macroscopic variables:

$$\rho = \sum_\alpha f_\alpha, \quad \rho\mathbf{u} = \sum_\alpha f_\alpha \boldsymbol{\xi}_\alpha, \quad \rho\varepsilon = \frac{1}{2}\sum_\alpha f_\alpha |\boldsymbol{\xi}_\alpha - \mathbf{u}|^2. \tag{3.2.16}$$

When multi-scaling using the Mach number is employed, these equations lead to Cauchy's equations for a compressible continuous medium of the following form:

$$\frac{\partial \rho}{\partial t} + \nabla\cdot(\rho\mathbf{u}) = 0, \tag{3.2.17}$$

$$\frac{\partial(\rho\mathbf{u})}{\partial t} + \nabla\cdot(\rho\mathbf{u}\otimes\mathbf{u}) = -\nabla p + \nu[\nabla^2(\rho\mathbf{u}) + \nabla(\nabla\cdot(\rho\mathbf{u}))]. \tag{3.2.18}$$

While the first equation delivers the correct form of the equation for the conservation of mass, the second leads to the equations of motion for an artificial compressible fluid because the pressure $p = \rho c_s^2$ has a thermodynamic form only, with c_s being the speed of sound. Of

course, this form of the pressure is not surprising due to the absence of any external forces in the original formulation (3.2.1). However, the expression for the kinematic viscosity is unusual for it is given by $\nu = (2\tau - 1)c^2 \triangle t/6$, and depends on the non-dimensional relaxation time τ and the time step $\triangle t$.

Turning to incompressible fluids, we note that the pressure p must be independent of the density. To derive such a model, Guo et al. (2000) found that a new type of distribution function $g_\alpha(\mathbf{x},t)$ is required. The important point is that this new distribution function is patterned along the lines of the BGK model; however, there is no statistical mechanical basis for this formulation. To understand this, one notes that the new equilibrium distribution function $g_\alpha^{(0)}(\mathbf{x},t)$is defined through

$$g_\alpha^{(0)} = \begin{cases} -4\sigma(p/c^2) + s_\alpha(\mathbf{u}), & \alpha = 0, \\ \lambda(p/c^2) + s_\alpha(\mathbf{u}) & \alpha = 1,3,5,7, \\ \gamma(p/c^2) + s_\alpha(\mathbf{u}), & \alpha = 2,4,6,8, \end{cases} \tag{3.2.19}$$

where σ, λ and γ are parameters satisfying

$$\lambda + \gamma = \sigma, \quad \lambda + 2\gamma = 1/2. \tag{3.2.20}$$

This new distribution function satisfies the following conservation laws:

$$\sum_{\alpha=0}^{8} g_\alpha = \sum_{\alpha=0}^{8} g_\alpha^{(0)}, \tag{3.2.21}$$

$$\sum_{\alpha=0}^{8} c\mathbf{e}_\alpha g_\alpha = \sum_{\alpha=0}^{8} c\mathbf{e}_\alpha g_\alpha^{(0)}. \tag{3.2.22}$$

The evolution equation for the system is given by

$$g_\alpha(\mathbf{x} + c\mathbf{e}_\alpha \triangle t, t + \triangle t) - g_\alpha(\mathbf{x},t) = -\frac{1}{\tau}[g_\alpha(\mathbf{x},t) - g_\alpha^{(0)}(\mathbf{x},t)]. \tag{3.2.23}$$

The velocity and pressure of the flow are given by

$$\mathbf{u} = \sum_{\alpha=0}^{8} c\mathbf{e}_\alpha g_\alpha, \tag{3.2.24}$$

$$p = \frac{c^2}{4\sigma}\left[\sum_{\alpha=1}^{8} g_\alpha + s_0(\mathbf{u})\right]. \tag{3.2.25}$$

From the chosen distribution function, a multi-scale expansion as described in full in the Appendix of the paper by Guo et al. (2000), leads to the following set of equations applicable to an incompressible fluid:

$$\nabla \cdot \mathbf{u} = 0, \tag{3.2.26}$$

$$\frac{\partial \mathbf{u}}{\partial t} + \nabla \cdot (\mathbf{u} \otimes \mathbf{u}) = -\nabla p + \nu \nabla^2 \mathbf{u}. \tag{3.2.27}$$

While p can now be arbitrary, the kinematic viscosity ν is still relaxation time and grid-dependent, for it is given by

$$\nu = \frac{(2\tau - 1)}{6} \cdot \frac{(\triangle x)^2}{\triangle t}. \tag{3.2.28}$$

In this context, it is necessary to recall that in addition to the work cited earlier (Frisch et al. (1987, 1986)), attempts to derive the Navier-Stokes equations for compressible or incompressible fluids have been made (Dubois (2008, 2009); Dubois and Lallemand (2009); Guo et al. (2002); Junk et al. (2005); Junk and Yong (2003)). In addition, thermal stability of the hydrodynamic equations has also been investigated (Lallemand and Luo (2003)). It is important to note that hydrodynamic equations deal, at most, with a restricted class of fluids, viz., the ideal gas or fluids with constant viscosity. Secondly, to obtain the equations for a Newtonian fluid, second and higher order lattice Boltzmann schemes have to employed (Dubois (2009); Dubois and Lallemand (2009)). The derivations given here in Section 3 are based on the results in (Fu and So (2009); Fu et al. (2012)) and are applicable to all fluids, compressible or incompressible. Secondly, the equations of continuum mechanics appear at

the expansion of the particle distribution functions at the first order, as described in full in (3.3) - (3.50) below.

Turing our attention to non-Newtonian fluids, we note that the relationship between the relaxation time and the viscosity means that the relaxation time has to be prescribed over a specific range only; hence, the viscosity function is restricted and cannot describe a wide range of non-Newtonian fluid models. This is clear from the previous studies employing LBM for non-Newtonian fluids; for example, see the work on power-law fluids (Boyd et al. (2006); Buick (2009); Gabbanelli et al. (2005); Nejat et al. (2011); Psihogios et al. (2007); Sullivan et al. (2006, 2007); Yoshino et al. (2007)) and Bingham fluids (Ohta et al. (2011); Tang et al. (2011); Wang and Ho (2008)). Even though a second order LBM scheme has been proposed in (Boyd et al. (2006)) to solve problems in power-law fluids, the kinematic viscosity is still related to the relaxation time. Hence, a new approach to deriving the equations of continuum mechanics applicable to all fluids is needed, and we turn to this next, employing the TDDFM due to Fu et al. (2012).

3.3 Thermal Difference Discrete Flux Method (TDDFM) to continuum mechanics

First of all, the lattice counterpart of (3.2.1) with the assumption that the collision term $N(f) = f^{eq}/\lambda$ can be written as follows:

$$\frac{\partial f_\alpha}{\partial t} + \boldsymbol{\xi}_\alpha \cdot \nabla_{\mathbf{x}} f_\alpha = -\frac{1}{\varepsilon\,\tau}(f_\alpha - f_\alpha^{eq}), \tag{3.3.1}$$

where ε is a small parameter to be prescribed when numerical simulations are considered and f^{eq} is the equilibrium lattice function. To proceed, one assumes that f_α has the following expansion:

$$f_\alpha = f_\alpha^{eq} + \varepsilon f_\alpha^{(1)} + \varepsilon^2 f_\alpha^{(2)} + O(\varepsilon^3). \tag{3.3.2}$$

The novelty of the approach by Fu and So (2009) lies in expanding the equilibrium lattice function f_α^{eq} as a quadratic in the particle velocity $\boldsymbol{\xi}_\alpha$:

$$f_\alpha^{eq} = A_\alpha + \boldsymbol{\xi}_\alpha \cdot \mathbf{B}_\alpha + (\boldsymbol{\xi}_\alpha \otimes \boldsymbol{\xi}_\alpha) : \mathbf{C}_\alpha, \tag{3.3.3}$$

where $\mathbf{B}_\alpha$ is a vector and $\mathbf{C}_\alpha$ is a 2×2 symmetric matrix. Before defining these entities, the following relations must hold (cf. (3.2.16)):

$$\sum_{\alpha=0}^{8} f_\alpha^{eq} = \rho, \tag{3.3.4}$$

$$\sum_{\alpha=0}^{8} f_\alpha^{eq}\boldsymbol{\xi}_\alpha = \rho\mathbf{u}, \quad \mathbf{u} = u\mathbf{i} + v\mathbf{j}, \tag{3.3.5}$$

$$\sum_{\alpha=0}^{8} f_\alpha^{eq}\boldsymbol{\xi}_\alpha \otimes \boldsymbol{\xi}_\alpha = \mathbf{M}, \tag{3.3.6}$$

$$\sum_{\alpha=0}^{8} f_\alpha^{(n)} = 0, \quad n \geq 1, \tag{3.3.7}$$

$$\sum_{\alpha=0}^{8} f_\alpha^{(n)}\boldsymbol{\xi}_\alpha = \mathbf{0}, \quad n \geq 1. \tag{3.3.8}$$

In (3.3.6), $\mathbf{M}$ has the matrix form

$$\mathbf{M} = \begin{bmatrix} \rho u^2 + p - \tau_{xx} & \rho uv - \tau_{xy} \\ \rho uv - \tau_{xy} & \rho v^2 + p - \tau_{yy} \end{bmatrix}. \tag{3.3.9}$$

In the above set, ρ is the density, u and v are the components of the velocity field $\mathbf{u}$ in the x and y directions respectively, $\tau_{xx}, \tau_{xy} = \tau_{yx}, \tau_{yy}$ are the stresses which can be defined through any relevant constitutive relation.

For a D2Q9 lattice, in (3.3.3), there are nine coefficients: $A_\alpha, \mathbf{B}_\alpha$, and $\mathbf{C}_\alpha$. However, when $\alpha = 0$, only the coefficient A_0 is required. Regarding the others, one makes the assumption that the coefficients having the same energy shell of the lattice velocities are equal. Thus, $A_\alpha = A_1,\ \alpha = 1,3,5,7;\ A_\alpha = A_2,\ \alpha = 2,4,6,8$.

Since $\mathbf{B}_0$ and $\mathbf{C}_0$ do not affect the value of f_0^{eq} in (3.3.3), they can be put equal to zero. By the just mentioned assumption about certain coefficients being equal, we see that $\mathbf{B}_\alpha = \mathbf{B}_1,\ \alpha = 1,3,5,7;\ \mathbf{B}_\alpha = \mathbf{B}_2,\ \alpha = 2,4,6,8$. Similarly, $\mathbf{C}_\alpha = \mathbf{C}_1,\ \alpha = 1,3,5,7;\ \mathbf{C}_\alpha = \mathbf{C}_2,\ \alpha = 2,4,6,8$. Keeping in mind that the matrices are symmetric, there are thirteen

independent quantities: three scalars in $A_0,\ A_1,\ A_2$; four components of the vectors $\mathbf{B}_1,\ \mathbf{B}_2$; three components each in $\mathbf{C}_1,\ \mathbf{C}_2$. Looking at (3.3.4) - (3.3.6), it is obvious that the number of available constraints is six only. Thus, there is a lot of latitude in choosing the variables.

Following Fu and So (2009), we shall assume that

$$A_0 = \rho - \frac{2p}{\sigma^2} - \frac{\rho|\mathbf{u}|^2}{\sigma^2} + \frac{\tau_{xx}+\tau_{yy}}{\sigma^2}, \quad A_1 = A_2 = 0, \tag{3.3.10}$$

and

$$\mathbf{B}_1 = \frac{\rho\mathbf{u}}{2\sigma^2}, \quad \mathbf{B}_2 = \mathbf{0}. \tag{3.3.11}$$

Next,

$$\mathbf{C}_1 = \begin{bmatrix} C_{11} & 0 \\ 0 & C_{22} \end{bmatrix}, \quad C_{11} = \frac{1}{2\sigma^4}(p+\rho u^2 - \tau_{xx}), \quad C_{22} = \frac{1}{2\sigma^4}(p+\rho v^2 - \tau_{yy}), \tag{3.3.12}$$

and

$$\mathbf{C}_2 = \begin{bmatrix} 0 & C_{12} \\ C_{21} & 0 \end{bmatrix}, \quad C_{12} = C_{21} = \frac{1}{8\sigma^4}(\rho uv - \tau_{xy}). \tag{3.3.13}$$

Here, σ is a constant to be determined keeping in mind that the vectors $\boldsymbol{\xi}_\alpha$ have been redefined so that in (3.2.13), $c = \sigma$, the lattice speed. Since the value of σ affects numerical stability, its choice depends on the problem at hand. For instance, in their solution to the Stokes second problem, Fu and So (2009) recommend varying it at every iteration step. This matter is briefly addressed in Section 5 below.

Before deriving the macroscopic equations of continuum mechanics for incompressible fluids, we note that in several fluids, such as viscoplastic fluids, the pressure p has to be defined uniquely. This requires that the trace of the extra stress tensor should be zero. For a proof, see Rajagopal and Srinivasa (2005), Huilgol (2009) and Huilgol (2015). Thus, in

(3.3.10), $\tau_{xx}+\tau_{yy}=0$, and, in these models, the coefficient A_0 has the simple form:

$$A_0=\rho-\frac{2p}{\sigma^2}-\frac{\rho|\mathbf{u}|^2}{\sigma^2}. \tag{3.3.14}$$

We shall now demonstrate that the macroscopic equations for an incompressible continuous medium can be derived from (3.3.1) - (3.3.9). To make the calculations more transparent, it is helpful to note that

$$f_0^{eq} = A_0, \quad f_1^{eq}=\frac{\rho}{2\sigma}u+\sigma^2C_{11}, \quad f_5^{eq}=-\frac{\rho}{2\sigma}u+\sigma^2C_{11}, \tag{3.3.15}$$

$$f_3^{eq} = \frac{\rho}{2\sigma}v+\sigma^2C_{22}, \quad f_7^{eq}=-\frac{\rho}{2\sigma}v+\sigma^2C_{22}, \tag{3.3.16}$$

$$f_2^{eq} = f_6^{eq}=C_{12}, \quad f_4^{eq}=f_8^{eq}=-C_{12}. \tag{3.3.17}$$

Hence, Eqs. (3.3.4) - (3.3.9) follow from the substitution of (3.3.10) - (3.3.13) into (3.3.4) - (3.3.6), which is as expected. Secondly, substituting the expression for f_α in (3.3.2) into (3.3.1), we find that

$$\frac{\partial f_\alpha^{eq}}{\partial t}+\boldsymbol{\xi}_\alpha\cdot\nabla_{\mathbf{x}}f_\alpha^{eq}=-\frac{1}{\tau}f_\alpha^{(1)}+O(\varepsilon). \tag{3.3.18}$$

Since the velocity vectors $\boldsymbol{\xi}_\alpha$ do not depend on the spatial coordinates, one sees that

$$\nabla\cdot(f_\alpha^{eq}\boldsymbol{\xi}_\alpha)=\boldsymbol{\xi}_\alpha\cdot\nabla_{\mathbf{x}}f_\alpha^{eq}. \tag{3.3.19}$$

Hence, (3.3.18) can be rewritten as

$$\frac{\partial f_\alpha^{eq}}{\partial t}+\nabla\cdot(f_\alpha^{eq}\boldsymbol{\xi}_\alpha)=-\frac{1}{\tau}f_\alpha^{(1)}+O(\varepsilon). \tag{3.3.20}$$

Summing the equation above, we obtain

$$\frac{\partial}{\partial t}\left(\sum_{\alpha=0}^{8} f_{\alpha}^{eq}\right)+\nabla\cdot\left(\sum_{\alpha=0}^{8} f_{\alpha}^{eq}\boldsymbol{\xi}_{\alpha}\right)=-\frac{1}{\tau}\sum_{\alpha=0}^{8} f_{\alpha}^{(1)}+O(\varepsilon). \tag{3.3.21}$$

Appealing to (3.3.4), (3.3.5), (3.3.7) and recalling that ρ is a constant, the above equation reduces to

$$\rho(\nabla\cdot\mathbf{u})=O(\varepsilon), \tag{3.3.22}$$

or the continuity equation for an incompressible medium is satisfied to $O(\varepsilon)$. Next,

$$\nabla\cdot(f_{\alpha}^{eq}\boldsymbol{\xi}_{\alpha}\otimes\boldsymbol{\xi}_{\alpha})=(\boldsymbol{\xi}_{\alpha}\cdot\nabla_{\mathbf{x}}f_{\alpha}^{eq})\boldsymbol{\xi}_{\alpha}. \tag{3.3.23}$$

Hence, multiplying (3.3.18) throughout by $\boldsymbol{\xi}_{\alpha}$, summing over α, and appealing to (3.3.5) - (3.3.8), one obtains to $O(\varepsilon)$.

$$\rho\frac{\partial\mathbf{u}}{\partial t}+\nabla\cdot\mathbf{M}=O(\varepsilon). \tag{3.3.24}$$

Rearranging, one obtains the equations of motion for an incompressible fluid:

$$\rho\mathbf{a}+\nabla p-\nabla\cdot\boldsymbol{\tau}=O(\varepsilon),\quad \mathbf{a}=\frac{\partial\mathbf{u}}{\partial t}+(\mathbf{u}\cdot\nabla)\mathbf{u}. \tag{3.3.25}$$

Thus, the set of equations (3.3.1) - (3.3.13) deliver Cauchy's equations of motion for an incompressible medium to $O(\varepsilon)$. Clearly, one can specify the material through a chosen constitutive equation for the extra stress tensor $\boldsymbol{\tau}$, whether the fluid be Newtonian, or non-Newtonian. At this juncture, it has to be noted that in the equations of motion (3.3.25), the body force term is missing. It is possible to do so by altering the evolution equation, suggested in the work by Fu et al. (2012).

If the body force is given by $\rho\mathbf{b}$, it has to be incorporated into the evolution equation (3.3.1) in such a way that (3.3.4) - (3.3.9) are unaffected. Since we are dealing with a D2Q9

lattice, the following modification is made:

$$\frac{\partial f_\alpha}{\partial t} + \boldsymbol{\xi}_\alpha \cdot \nabla_{\mathbf{x}} f_\alpha - F_\alpha = -\frac{1}{\varepsilon\,\tau}(f_\alpha - f_\alpha^{eq}). \tag{3.3.26}$$

The new set of functions F_α must be such that

$$\sum_{\alpha=0}^{8} F_\alpha = 0, \tag{3.3.27}$$

which guarantees that the mass conservation equation (3.3.22) is unchanged. Next, one requires that

$$\sum_{\alpha=0}^{8} F_\alpha \boldsymbol{\xi}_\alpha = \rho \mathbf{b}, \tag{3.3.28}$$

so that the momentum equation (3.3.25) has the form

$$\rho \mathbf{a} + \nabla p - \nabla \cdot \boldsymbol{\tau} - \rho \mathbf{b} = O(\varepsilon). \tag{3.3.29}$$

Thus, one choice for the set of F_α is:

$$F_0 = 0, \quad F_1 = \frac{1}{2\sigma^2}\rho \mathbf{b}\cdot\boldsymbol{\xi}_1, \quad F_3 = \frac{1}{2\sigma^2}\rho \mathbf{b}\cdot\boldsymbol{\xi}_3, \tag{3.3.30}$$

$$F_5 = \frac{1}{2\sigma^2}\rho \mathbf{b}\cdot\boldsymbol{\xi}_5, \quad F_7 = \frac{1}{2\sigma^2}\rho \mathbf{b}\cdot\boldsymbol{\xi}_7, \tag{3.3.31}$$

$$F_\alpha = 0, \quad \alpha = 2,4,6,8. \tag{3.3.32}$$

To verify (3.3.27) - (3.3.28), one observes that $F_1 = -F_5,\ F_3 = -F_7$.

The Energy Equation

In order to obtain the energy equation, an internal energy distribution function g_α is introduced and it is assumed to satisfy an evolution equation similar to that for f_α. Thus,

$$\frac{\partial g_\alpha}{\partial t} + \boldsymbol{\xi}_\alpha \cdot \nabla_{\mathbf{x}} g_\alpha - G_\alpha = -\frac{1}{\varepsilon\tau}(g_\alpha - g_\alpha^{eq}). \tag{3.3.33}$$

Here, g_α^{eq} has a linear form in the lattice velocity vector as follows:

$$g_\alpha^{eq} = D_\alpha + \boldsymbol{\xi}_\alpha \cdot \mathbf{E}_\alpha. \tag{3.3.34}$$

And,

$$g_\alpha = g_\alpha^{eq} + \varepsilon g_\alpha^{(1)} + \varepsilon^2 g_\alpha^{(2)} + O(\varepsilon^3), \tag{3.3.35}$$

with the requirement that

$$\sum_{\alpha=0}^{8} g_\alpha^{(n)} = 0, \quad n \geq 1. \tag{3.3.36}$$

The energy equation applicable to an incompressible continuous media is given by

$$\rho \frac{de}{dt} = \frac{1}{2}\boldsymbol{\tau} : \mathbf{A}_1 - \nabla \cdot \mathbf{q} + \rho r, \tag{3.3.37}$$

where e is the internal energy, $\mathbf{A}_1$ is the first Rivlin-Ericksen tensor (Rivlin and Ericksen (1955)), $\mathbf{q}$ is the heat efflux vector and r is the external supply. The derivation of this equation can be found in standard books on continuum mechanics and rheology; for example, see Tanner (2000).

In order to derive the above equation from the internal energy distribution function, it is assumed that e_t is the total energy given by the sum of the internal and kinetic energies, i.e.,

$$e_t = e + \frac{1}{2}|\mathbf{u}|^2. \tag{3.3.38}$$

Next, the following consistency relations must hold:

$$\sum_{\alpha=0}^{8} g_\alpha^{eq} = \rho e_t, \tag{3.3.39}$$

$$\sum_{\alpha=0}^{8} g_\alpha^{eq} \boldsymbol{\xi}_\alpha = \left(p+\rho e+\frac{1}{2}\rho|\mathbf{u}|^2\right)\mathbf{u}-\boldsymbol{\tau}\mathbf{u}+\mathbf{q}, \tag{3.3.40}$$

$$\sum_{\alpha=0}^{8} G_\alpha = \rho\mathbf{b}\cdot\mathbf{u}-\rho r. \tag{3.3.41}$$

One way of satisfying the above is to assume, as before, that $D_\alpha = D_1,\ \alpha = 1,3,5,7$, and $D_\alpha = D_2,\ \alpha = 2,4,6,8$, and set

$$D_0 = \rho e_t, \quad D_1 = 0, \quad D_2 = 0. \tag{3.3.42}$$

In addition, it is assumed that $\mathbf{E}_0 = \mathbf{0},\ \mathbf{E}_\alpha = \mathbf{E}_1,\ \alpha = 1,3,5,7; \mathbf{E}_\alpha = \mathbf{E}_2,\ \alpha = 2,4,6,8$, where

$$\mathbf{E}_1 = \frac{1}{2\sigma^2}\left(p+\rho e+\frac{1}{2}\rho|\mathbf{u}|^2\right)\mathbf{u}-\boldsymbol{\tau}\mathbf{u}+\mathbf{q}, \quad \mathbf{E}_2 = \mathbf{0}. \tag{3.3.43}$$

Finally, $G_0 = 0$, and

$$G_\alpha = \frac{1}{2\sigma^2}\rho\mathbf{b}\cdot(\boldsymbol{\xi}_\alpha\otimes\boldsymbol{\xi}_\alpha)\mathbf{u}-\frac{1}{4\sigma^2}\rho r(\boldsymbol{\xi}_\alpha\otimes\boldsymbol{\xi}_\alpha):\mathbf{1}, \quad \alpha = 1,3,5,7, \tag{3.3.44}$$

$$G_\alpha = 0,\ \alpha = 2,4,6,8. \tag{3.3.45}$$

Letting $\mathbf{b} = b_x\mathbf{i}+b_y\mathbf{j}$, it is easy to verify that

$$\mathbf{b}\cdot(\boldsymbol{\xi}_1\otimes\boldsymbol{\xi}_1)\mathbf{u} = \mathbf{b}\cdot(\boldsymbol{\xi}_5\otimes\boldsymbol{\xi}_5)\mathbf{u} = \sigma^2 b_x u, \tag{3.3.46}$$

$$\mathbf{b}\cdot(\boldsymbol{\xi}_3\otimes\boldsymbol{\xi}_3)\mathbf{u} = \mathbf{b}\cdot(\boldsymbol{\xi}_7\otimes\boldsymbol{\xi}_7)\mathbf{u} = \sigma^2 b_y v, \tag{3.3.47}$$

$$(\boldsymbol{\xi}_\alpha\otimes\boldsymbol{\xi}_\alpha):\mathbf{1} = \sigma^2, \quad \alpha = 1,3,5,7, \tag{3.3.48}$$

which means that (3.3.41) is satisfied.

Finally, summing Eq. (3.3.33) over all α, and using (3.3.34) - (3.3.36), one finds that

$$\rho\frac{de}{dt}+\rho\frac{\partial \mathbf{u}}{\partial t}\cdot\mathbf{u}+\nabla\cdot\left(\sum_{\alpha=0}^{8} g_{\alpha}^{eq}\boldsymbol{\xi}_{\alpha}\right)-\rho\mathbf{b}\cdot\mathbf{u}=O(\varepsilon). \tag{3.3.49}$$

Next,

$$\nabla\cdot\left(p+\rho e+\frac{1}{2}\rho|\mathbf{u}|^2\right)\mathbf{u}=\left(\nabla p+\rho\nabla e+\rho(\mathbf{u}\cdot\nabla)\mathbf{u}\right)\cdot\mathbf{u}, \tag{3.3.50}$$

because $\nabla\cdot\mathbf{u}=0$. Finally, using indicial notation for convenience and noting the symmetry of the stress tensor,

$$(\tau_{ij}u_j)_{,i}=\tau_{ij,i}u_j+\tau_{ij}u_{i,j}=\tau_{ji,j}u_i+\frac{1}{2}\tau_{ij}(A_1)_{ij}. \tag{3.3.51}$$

Thus,

$$\nabla\cdot(\boldsymbol{\tau}\mathbf{u})=(\nabla\cdot\boldsymbol{\tau})\cdot\mathbf{u}+\frac{1}{2}\boldsymbol{\tau}:\mathbf{A}_1. \tag{3.3.52}$$

Combining all of the above, we obtain

$$\rho\frac{de}{dt}+\left(\rho\mathbf{a}+\nabla p-\nabla\cdot\boldsymbol{\tau}-\rho\mathbf{b}\right)\cdot\mathbf{u}-\frac{1}{2}\boldsymbol{\tau}:\mathbf{A}_1+\nabla\cdot\mathbf{q}-\rho r=O(\varepsilon), \tag{3.3.53}$$

which reduces to (3.3.37) when one appeals to the equations of motion (3.3.29).

Algorithm

The main equations of the discrete particle distribution function and the internal energy distribution function are solved by the splitting method of Toro (1999). Hence, the equations can be separated into two parts. The first one is the streaming section which is written as

$$\frac{\partial f_{\alpha}}{\partial t}+\boldsymbol{\xi}_{\alpha}\cdot\nabla_{\mathbf{x}}f_{\alpha}-F_{\alpha}=0. \tag{3.3.54}$$

$$\frac{\partial g_\alpha}{\partial t} + \boldsymbol{\xi}_\alpha \cdot \nabla_{\mathbf{x}} g_\alpha = 0. \tag{3.3.55}$$

Eqs.(3.3.54) and (3.3.55) have been solved with the method of Lax and Wendroff (1960) and the following equations are used.

$$\begin{aligned} f_\alpha^{n+1}(i,j) = f_\alpha^n(i,j) &- \frac{\Delta t}{2\Delta x}\xi_\alpha(i)\left[f_\alpha^n(i+1,j) - f_\alpha^n(i-1,j)\right] \\ &- \frac{\Delta t}{2\Delta y}\xi_\alpha(j)\left[f_\alpha^n(i,j+1) - f_\alpha^n(i,j-1)\right] + \\ \frac{\Delta t^2}{2\Delta x^2}{\xi_\alpha}^2(i)&\left[f_\alpha^n(i+1,j) - 2f_\alpha^n(i,j) + f_\alpha^n(i-1,j)\right] + F_\alpha(i)\Delta t + \\ \frac{\Delta t^2}{2\Delta y^2}{\xi_\alpha}^2(j)&\left[f_\alpha^n(i,j+1) - 2f_\alpha^n(i,j) + f_\alpha^n(i,j-1)\right] + F_\alpha(j)\Delta t\ , \end{aligned} \tag{3.3.56}$$

and

$$\begin{aligned} g_\alpha^{n+1}(i,j) = g_\alpha^n(i,j) &- \frac{\Delta t}{2\Delta x}\xi_\alpha(i)\left[g_\alpha^n(i+1,j) - g_\alpha^n(i-1,j)\right] \\ &- \frac{\Delta t}{2\Delta y}\xi_\alpha(j)\left[g_\alpha^n(i,j+1) - g_\alpha^n(i,j-1)\right] + \\ \frac{\Delta t^2}{2\Delta x^2}{\xi_\alpha}^2(i)&\left[g_\alpha^n(i+1,j) - 2g_\alpha^n(i,j) + g_\alpha^n(i-1,j)\right] + \\ \frac{\Delta t^2}{2\Delta y^2}{\xi_\alpha}^2(j)&\left[g_\alpha^n(i,j+1) - 2g_\alpha^n(i,j) + g_\alpha^n(i,j-1)\right] \end{aligned} \tag{3.3.57}$$

In Eqs.(3.3.56) and (3.3.57), we have put

$$\xi_\alpha(i) = \boldsymbol{\xi}_\alpha \cdot \mathbf{i}, \quad \xi_\alpha(j) = \boldsymbol{\xi}_\alpha \cdot \mathbf{j}, \quad F_\alpha(i) = \mathbf{F}_\alpha \cdot \mathbf{i}, \quad F_\alpha(j) = \mathbf{F}_\alpha \cdot \mathbf{j}. \tag{3.3.58}$$

The second part is the collision section which is as follows:

$$\frac{\partial f_\alpha}{\partial t} = -\frac{1}{\tau}(f_\alpha(\mathbf{x},t) - f_\alpha^{eq}(\mathbf{x},t)), \tag{3.3.59}$$

$$\frac{\partial g_\alpha}{\partial t} = -\frac{1}{\tau}(g_\alpha(\mathbf{x},t) - g_\alpha^{eq}(\mathbf{x},t)). \tag{3.3.60}$$

Eqs.(3.3.59) and (3.3.60) can be solved by using the Euler method and the choice of τ is taken as the time step (Δt). That is

$$\frac{f_\alpha(\mathbf{x},t+\Delta t) - f_\alpha(\mathbf{x},t)}{\Delta t} = -\frac{1}{\tau}(f_\alpha(\mathbf{x},t) - f_\alpha^{eq}(\mathbf{x},t)), \tag{3.3.61}$$

$$\frac{g_\alpha(\mathbf{x},t+\Delta t) - g_\alpha(\mathbf{x},t)}{\Delta t} = -\frac{1}{\tau}(g_\alpha(\mathbf{x},t) - g_\alpha^{eq}(\mathbf{x},t)), \tag{3.3.62}$$

from which one obtains

$$f_\alpha(\mathbf{x},t+\Delta t) = f_\alpha^{eq}(\mathbf{x},t), \tag{3.3.63}$$

and

$$g_\alpha(\mathbf{x},t+\Delta t) = g_\alpha^{eq}(\mathbf{x},t). \tag{3.3.64}$$

The numerical procedures are summarised below.

Initial stage

(a) Initial conditions for all macroscopic quantities (u_0, v_0, p_0) including the boundary points are given. The initial values of $f_\alpha^{0,eq}$ and $g_\alpha^{0,eq}$ including the boundary points are determined using Eqs.(3.3.3 - 3.3.13) and Eqs. (3.3.34 - 3.3.45) respectively. These are used as initial values to start the calculation.

Streaming stage

(b) With f_α and g_α at time t (including the boundary points) known, intermediate values f_α^I and g_α^I are calculated by solving Eqs.(3.3.56) and (3.3.57) respectively.
(c) Using these f_α^I and g_α^I, the corresponding macroscopic quantities (u_I, v_I, p_I, T_I) for all interior grid points are calculated.
(d) The boundary conditions for the macroscopic level are then set as in any finite difference method.
(e) Using the macroscopic quantities thus determined over the complete domain including the boundary points and invoking Eqs.(3.3.3 - 3.3.13) and Eqs. (3.3.34 - 3.3.45), the corresponding $f_\alpha^{I,eq}$ and $g_\alpha^{I,eq}$ are obtained, including all of the boundary points.

Collision stage

(f) Due to Eqs.(3.3.63) and (3.3.64), the collision step is completed by setting the new value at time $t+\Delta t$ as $f_\alpha^{I,eq}$. Since each set of macroscopic quantities will map uniquely to an equilibrium distribution function and vice versa, the macroscopic quantities thus obtained are, in fact, the values at time $t+\Delta t$, i.e., $(u, v, p, T)_{t+\Delta t} = (u_I, v_I, p_I, T_I)$.

(g) Time marching proceeds by repeating steps (b)-(f).

Compressible Fluids

The continuity, the equations of motion and the energy equations for compressible fluids can be derived quite easily. First of all, Eqs. (3.3.4) - (3.3.8) remain unchanged, while the

matrix $\mathbf{M}$ in Eq. (3.3.9) has the form:

$$\mathbf{M} = \begin{bmatrix} \rho u^2 - T_{xx} & \rho uv - T_{xy} \\ \rho uv - T_{xy} & \rho v^2 - T_{yy} \end{bmatrix}, \tag{3.3.65}$$

where T_{xx}, T_{xy}, T_{yy} are the components of the total stress tensor. A glance at Eqs. (3.3.10) - (3.3.13) shows that $A_1, A_2, \mathbf{B}_1, \mathbf{B}_2$ are unchanged, while one needs the following:

$$A_0 = \rho - \frac{\rho|\mathbf{u}|^2}{\sigma^2} + \frac{T_{xx}+T_{yy}}{\sigma^2}, \tag{3.3.66}$$

$$C_{11} = \frac{1}{2\sigma^4}(\rho u^2 - T_{xx}), \quad C_{22} = \frac{1}{2\sigma^4}(\rho v^2 - T_{yy}), \tag{3.3.67}$$

$$C_{12} = C_{21} = \frac{1}{8\sigma^4}(\rho uv - T_{xy}). \tag{3.3.68}$$

Next, the energy equation (3.3.37) is now given by

$$\rho \frac{de}{dt} = \frac{1}{2}\mathbf{T} : \mathbf{A}_1 - \nabla \cdot \mathbf{q} + \rho r. \tag{3.3.69}$$

Thus, one requires the following changes be made:

$$\sum_{\alpha=0}^{8} g_\alpha^{eq} \boldsymbol{\xi}_\alpha = \left(\rho e + \frac{1}{2}\rho|\mathbf{u}|^2 - \mathbf{T}\right)\mathbf{u} + \mathbf{q}, \tag{3.3.70}$$

$$\mathbf{E}_1 = \frac{1}{2\sigma^2}\left(\rho e + \frac{1}{2}\rho|\mathbf{u}|^2 - \mathbf{T}\right)\mathbf{u} + \mathbf{q}. \tag{3.3.71}$$

Boundary conditions

One of the main advantages of the current approach is that boundary conditions can be incorporated in a manner similar to macroscopic methods, in contrast with other methods utilised for solving LBM equations. The latter employ complicated special relationships for the discrete particle distribution function (f_α) and the internal energy distribution function (g_α) for each kind of boundary conditions and problems (Guo et al. (2002); Zou and He

(1997)). For example, methods such as on-grid and mid-grid bounce back are used when the velocity is zero on the boundary; when the boundary is in motion, bounce-back is used along with a set of linear equations to determine the boundary values f_α. In the method used here, the boundary conditions of f_α and g_α can be obtained directly from the macroscopic values on the boundaries due to the relationships of the macroscopic values with f_α as seen from (3.3.3) - (3.3.7); in the case of g_α, see (3.3.34), (3.3.38)) - (3.3.41). As a result, in this method, boundary conditions, especially the Dirichlet conditions, can be included in various problems similar to macroscopic methods and no special equations for f_α and g_α are needed to incorporate the boundary conditions.

3.4 Three dimensional equations for continua

In order to derive the equations of continuum mechanics applicable to motions in three dimensions, one can employ a D3Q15 lattice (Fu et al. (2012)). Of course, any space-filling, symmetric lattice can be used for the derivation of the equations of continuum mechanics, since the method relies on the expansion of the particle distribution function as a polynomial in the particle velocity; see (3.4.2) below. In the case of the D3Q15 lattice, there are 15 nodes and one lies at the centre of a cube with a side of 2 units each; six are chosen from the midpoints of the faces of the cube and the remaining eight are the vertices. In the Table, the positions of the nodes and the corresponding microscopic velocities $\boldsymbol{\xi}_\alpha$, divided by σ for convenience, are given.

In order to obtain the continuity equation and the equations of motion, we observe that Eqs. (3.3.2) and (3.3.3) hold and the evolution equation for the particle distribution function is once again given by (cf. (3.3.26)):

$$\frac{\partial f_\alpha}{\partial t} + \boldsymbol{\xi}_\alpha \cdot \nabla_{\mathbf{x}} f_\alpha - F_\alpha = -\frac{1}{\varepsilon\,\tau}(f_\alpha - f_\alpha^{eq}), \tag{3.4.1}$$

with the following quadratic form:

$$f_\alpha^{eq} = A_\alpha + \boldsymbol{\xi}_\alpha \cdot \mathbf{B}_\alpha + (\boldsymbol{\xi}_\alpha \otimes \boldsymbol{\xi}_\alpha) : \mathbf{C}_\alpha, \tag{3.4.2}$$

Table of Nodes and Microscopic Velocities

Node	Location	$\boldsymbol{\xi}_\alpha/\sigma$
α_0	(0, 0, 0)	$\mathbf{0}$
α_1	(1, 0, 0)	$\mathbf{i}$
α_2	(0, 1, 0)	$\mathbf{j}$
α_3	(-1, 0, 0)	$-\mathbf{i}$
α_4	(0, -1, 0)	$-\mathbf{j}$
α_5	(0, 0, 1)	$\mathbf{k}$
α_6	(0, 0, -1)	$-\mathbf{k}$
α_7	(1, 1, 1)	$\mathbf{i}+\mathbf{j}+\mathbf{k}$
α_8	(-1, 1, 1)	$-\mathbf{i}+\mathbf{j}+\mathbf{k}$
α_9	(-1, -1, 1)	$-\mathbf{i}-\mathbf{j}+\mathbf{k}$
α_{10}	(1, -1, 1)	$\mathbf{i}-\mathbf{j}+\mathbf{k}$
α_{11}	(1, 1, -1)	$\mathbf{i}+\mathbf{j}-\mathbf{k}$
α_{12}	(-1 , 1, -1)	$-\mathbf{i}+\mathbf{j}-\mathbf{k}$
α_{13}	(-1, -1, -1)	$-\mathbf{i}-\mathbf{j}-\mathbf{k}$
α_{14}	(1, -1, -1)	$\mathbf{i}-\mathbf{j}-\mathbf{k}$

Next, Eqs. (3.3.3) - (3.3.9) are modified as follows:

$$\sum_{\alpha=0}^{14} f_\alpha^{eq} = \rho, \tag{3.4.3}$$

$$\sum_{\alpha=0}^{14} f_\alpha^{eq} \boldsymbol{\xi}_\alpha = \rho \mathbf{u}, \quad \mathbf{u} = u\mathbf{i} + v\mathbf{j} + w\mathbf{k}, \tag{3.4.4}$$

$$\sum_{\alpha=0}^{14} f_\alpha^{eq} \boldsymbol{\xi}_\alpha \otimes \boldsymbol{\xi}_\alpha = \mathbf{M}, \tag{3.4.5}$$

$$\sum_{\alpha=0}^{14} f_\alpha^{(n)} = \mathbf{0}, \quad n \geq 1, \tag{3.4.6}$$

$$\sum_{\alpha=0}^{14} f_\alpha^{(n)} \boldsymbol{\xi}_\alpha = \mathbf{0}, \quad n \geq 1. \tag{3.4.7}$$

In (3.4.5), $\mathbf{M}$ has the matrix form

$$\mathbf{M} = \begin{bmatrix} \rho u^2 - T_{xx} & \rho uv - T_{xy} & \rho uw - T_{xz} \\ \rho uv - T_{xy} & \rho v^2 - T_{yy} & \rho vw - T_{yz} \\ \rho uw - T_{xz} & \rho vw - T_{yz} & \rho w^2 - T_{zz} \end{bmatrix}. \tag{3.4.8}$$

In the above set, ρ is the density, u, v and w are the components of the velocity field $\mathbf{u}$ in the x, y and z directions respectively, $T_{xx}, T_{xy}, T_{xz}, T_{yy}, T_{yz}, T_{zz}$ are the stresses which can be defined through any relevant constitutive relation for the continuous medium. The body force distribution functions now satisfy

$$\sum_{\alpha=0}^{14} F_\alpha = 0, \tag{3.4.9}$$

and

$$\sum_{\alpha=0}^{14} F_\alpha \boldsymbol{\xi}_\alpha = \rho \mathbf{b}. \tag{3.4.10}$$

As before, one choice for the set of F_α is:

$$F_0 = 0, \quad F_1 = \frac{1}{2\sigma^2}\rho\mathbf{b}\cdot\boldsymbol{\xi}_1 = -F_3, \tag{3.4.11}$$

$$F_2 = \frac{1}{2\sigma^2}\rho\mathbf{b}\cdot\boldsymbol{\xi}_2 = -F_4, \tag{3.4.12}$$

$$F_5 = \frac{1}{2\sigma^2}\rho\mathbf{b}\cdot\boldsymbol{\xi}_5 = -F_6, \tag{3.4.13}$$

$$F_\alpha = 0, \quad \alpha = 7,\cdots,14. \tag{3.4.14}$$

Finally, in (3.4.2), one has to specify the scalars A_α, the vectors $\mathbf{B}_\alpha$ and the matrices $\mathbf{C}_\alpha$. We assume that $A_1 = A_\alpha,\ \alpha = 1,\cdots 6; A_2 = A_\alpha = 7,\cdots 14$, and define

$$A_0 = \rho - \frac{\rho|\mathbf{u}|^2}{\sigma^2} + \frac{T_{xx}+T_{yy}+T_{zz}}{\sigma^2}, \quad A_1 = A_2 = 0. \tag{3.4.15}$$

Next, $\mathbf{B}_0 = \mathbf{0}$, and $\mathbf{B}_1 = \mathbf{B}_\alpha,\ \alpha = 1,\cdots 6; \mathbf{B}_2 = \mathbf{B}_\alpha = 7,\cdots 14$, and

$$\mathbf{B}_1 = \frac{\rho\mathbf{u}}{2\sigma^2}, \quad \mathbf{B}_2 = \mathbf{0}. \tag{3.4.16}$$

Next, once again, $\mathbf{C}_0 = \mathbf{0}$, and $\mathbf{C}_1 = \mathbf{C}_\alpha,\ \alpha = 1,\cdots 6; \mathbf{C}_2 = \mathbf{C}_\alpha = 7,\cdots 14$, and

$$\mathbf{C}_1 = \begin{bmatrix} C_{11} & 0 & 0 \\ 0 & C_{22} & 0 \\ 0 & 0 & C_{33} \end{bmatrix}, \quad C_{11} = \frac{1}{2\sigma^4}(\rho u^2 - T_{xx}), \tag{3.4.17}$$

$$C_{22} = \frac{1}{2\sigma^4}(\rho v^2 - T_{yy}), \quad C_{33} = \frac{1}{2\sigma^4}(\rho w^2 - T_{zz}). \tag{3.4.18}$$

Finally,

$$\mathbf{C}_2 = \begin{bmatrix} 0 & C_{12} & C_{13} \\ C_{21} & 0 & C_{23} \\ C_{31} & C_{32} & 0 \end{bmatrix}, \quad C_{12} = C_{21} = \frac{1}{16\sigma^4}(\rho uv - T_{xy}), \tag{3.4.19}$$

$$C_{23} = C_{32} = \frac{1}{16\sigma^4}(\rho vw - T_{yz}), \quad C_{13} = C_{31} = \frac{1}{16\sigma^4}(\rho uw - T_{xz}). \tag{3.4.20}$$

Repeating the calculations employed in Section 3, one can now derive the continuity equation and the equations of motion for a continuous medium, valid in three dimensions.

In order to obtain the energy equation, one begins with

$$\frac{\partial g_\alpha}{\partial t} + \boldsymbol{\xi}_\alpha \cdot \nabla_{\mathbf{x}} g_\alpha - G_\alpha = -\frac{1}{\varepsilon\tau}(g_\alpha - g_\alpha^{eq}), \tag{3.4.21}$$

where g_α^{eq} has a linear expansion:

$$g_\alpha^{eq} = D_\alpha + \boldsymbol{\xi}_\alpha \cdot \mathbf{E}_\alpha. \tag{3.4.22}$$

And,

$$g_\alpha = g_\alpha^{eq} + \varepsilon g_\alpha^{(1)} + \varepsilon^2 g_\alpha^{(2)} + O(\varepsilon^3), \tag{3.4.23}$$

with the requirement that

$$\sum_{\alpha=0}^{14} g_\alpha^{(n)} = 0, \quad n \geq 1. \tag{3.4.24}$$

The energy equation applicable to a continuous media is given by

$$\rho \frac{de}{dt} = \frac{1}{2}\mathbf{T} : \mathbf{A}_1 - \nabla \cdot \mathbf{q} + \rho r. \tag{3.4.25}$$

In order to derive the above equation from the internal energy distribution function, it is assumed that e_t is the total energy given by the sum of the internal and kinetic energies, i.e.,

$$e_t = e + \frac{1}{2}|\mathbf{u}|^2. \tag{3.4.26}$$

Next, the following consistency relations must hold:

$$\sum_{\alpha=0}^{14} g_\alpha^{eq} = \rho e_t, \tag{3.4.27}$$

$$\sum_{\alpha=0}^{14} g_\alpha^{eq} \boldsymbol{\xi}_\alpha = \left(\rho e + \frac{1}{2}\rho|\mathbf{u}|^2\right)\mathbf{u} - \mathbf{T}\mathbf{u} + \mathbf{q}, \tag{3.4.28}$$

$$\sum_{\alpha=0}^{14} G_\alpha = \rho \mathbf{b}\cdot\mathbf{u} - \rho r. \tag{3.4.29}$$

One way of satisfying the above is to assume, as before, that $D_\alpha = D_1,\ \alpha = 1,\cdots,6$, and $D_\alpha = D_2,\ \alpha = 7,\ldots 14$, and set

$$D_0 = \rho e_t, \quad D_1 = 0, \quad D_2 = 0. \tag{3.4.30}$$

In addition, it is assumed that $\mathbf{E}_0 = \mathbf{0},\ \mathbf{E}_\alpha = \mathbf{E}_1,\ \alpha = 1,\cdots,6; \mathbf{E}_\alpha = \mathbf{E}_2,\ \alpha = 7,\cdots,14$, where

$$\mathbf{E}_1 = \frac{1}{2\sigma^2}\left(\rho e + \frac{1}{2}\rho|\mathbf{u}|^2\right)\mathbf{u} - \mathbf{T}\mathbf{u} + \mathbf{q}, \quad \mathbf{E}_2 = \mathbf{0}. \tag{3.4.31}$$

Finally, $G_0 = 0$, and

$$G_\alpha = \frac{1}{2\sigma^2}\rho\mathbf{b}\cdot(\boldsymbol{\xi}_\alpha\otimes\boldsymbol{\xi}_\alpha)\mathbf{u} - \frac{1}{6\sigma^2}\rho r(\boldsymbol{\xi}_\alpha\otimes\boldsymbol{\xi}_\alpha):\mathbf{1}, \quad \alpha = 1,\cdots,6, \tag{3.4.32}$$

$$G_\alpha = 0,\ \alpha = 7,\cdots,14. \tag{3.4.33}$$

Once again, repeating the calculations in Section 3, the energy equation (3.4.25) can be derived.

3.5 Concluding remarks

Using an evolution equation for the modified particle distribution functions, equations of continuum mechanics in two and three dimensions have been derived. It is obvious that the choice of the constitutive equation for the incompressible or compressible fluid is unrestricted. Focussing attention on two-dimensional flows for convenience, it can be seen from the definition of the matrix $\mathbf{M}$ in (3.3.9) that the extra stresses $\tau_{xx}, \tau_{xy}, \tau_{yy}$, in an incompressible fluid, can be chosen at will. That is, the fluid model can be Newtonian or non-Newtonian. Similar observations apply to the matrix $\mathbf{M}$ in (3.4.8). The derivations given here, based on that in (Fu and So (2009); Fu et al. (2012)), are applicable to all fluids, compressible or incompressible. Secondly, the equations of continuum mechanics appear at the expansion of the particle distribution functions at the first order, as described in full in (3.3.3) - (3.3.53) and (3.4.1) - (3.4.33).

Next, some remarks regarding the numerical scheme are in order. As is well known, there are two main categories of flows in fluid mechanics. One is where the pressure gradient is specified, which occurs in the case of the flow in a pipe. The second is where the pressure field has to be determined as a part of the solution; consider the flow in a lid-driven cavity as an example. Both types of problems have to be solvable with the chosen numerical scheme for the determination of the distribution functions f_α and g_α.

For instance, consider the evolution equation for f_α in (3.2.23). This is solved by using the splitting method of Toro (1999) and explained in detail in Fu and So (2009); Fu et al. (2012). Briefly, the evolution equation is split into two parts. The first one is called the streaming section, equivalent to solving the homogeneous equation:

$$\frac{\partial f_\alpha}{\partial t} + \boldsymbol{\xi}_\alpha \cdot \nabla_{\mathbf{x}} f_\alpha - F_\alpha = 0. \tag{3.5.1}$$

In order to solve this equation, an initial value for f_α^{eq} is required. To determine this, one begins with an assumed velocity distribution in the domain, say $\mathbf{u}_0$, from which one determines the initial stress field through the designated constitutive equation. If the pressure field is prescribed, this can be used to calculate the matrix $\mathbf{M}$ from (3.3.9) and the initial value of f_α^{eq} from (3.3.3). If the pressure has to be determined as a part of the solution, one assumes that, in addition to $\mathbf{u}_0$, a value of f_α^{eq} is given. From (3.3.9), the pressure p can be determined from the trace of the matrix $\mathbf{M}$ in (3.3.9).

Next, using the initial value of f_α^{eq}, determined from the given initial macroscopic variables as in (3.3.3)- (3.3.9), the intermediate value of f_α^I is calculated by solving the homogeneous equation; for instance, the Lax-Wendroff scheme can be employed. Using this, the intermediate macroscopic value of the velocity field $\mathbf{u}^I$ is determined from (3.3.5).

The second one is called the collision section, equivalent to solving the time-dependent equation:

$$\frac{\partial f_\alpha}{\partial t} = -\frac{1}{\varepsilon\tau}(f_\alpha(\mathbf{x},t) - f_\alpha^{eq}(\mathbf{x},t)). \tag{3.5.2}$$

Using the previously determined f_α^I as the initial condition, the collision equation is now solved; for instance, the Euler method can be used.

To reiterate, considering two-dimensional flows for convenience, we note that the matrix $\mathbf{M}$ in (3.3.9) can be used in two different ways. If the pressure p is specified and the initial velocity vector $\mathbf{u}_0$ is known, one uses the relevant constitutive equation in this matrix to find the initial value of f_α^{eq}. On the other hand, if the pressure field has to be determined, the trace of the matrix can be employed; see Eqs. (18a) - (18c) in Fu and So (2009). Clearly, the constant density assumption is met, for it is inherent in the Eqs. (3.3.3) - (3.3.13). Moreover, at each iteration, a new value of the lattice speed σ is chosen employing (3.5.8) or (3.5.9) below.

Next, we shall discuss the stability of the numerical scheme. Multiplying (3.3.26) with $|\boldsymbol{\xi}|^2/2$ and the utilisation of (3.3.4) leads to

$$\sum_{\alpha=0}^{8} \frac{1}{2} f_\alpha |\boldsymbol{\xi}_\alpha|^2 = p + \frac{1}{2}\rho\,|\mathbf{u}|^2 - \frac{\tau_{xx}+\tau_{yy}}{2}. \tag{3.5.3}$$

Next, it is easy to verify from (3.3.27) - (3.3.28) that

$$\sum_{\alpha=0}^{8} F_\alpha |\boldsymbol{\xi}_\alpha|^2 = 0. \tag{3.5.4}$$

Hence, (3.3.26) becomes

$$\frac{\partial}{\partial t}\left[p + \frac{1}{2}\rho|\mathbf{u}|^2 - \frac{\tau_{xx}+\tau_{yy}}{2}\right] + \frac{\sigma^2}{2}\rho(\nabla\cdot\mathbf{u}) = O(\varepsilon). \tag{3.5.5}$$

The Courant-Friedrichs-Lewy (CFL) condition states that (Blazek (2001) and Cebeci et al. (2005))

$$K = \frac{u\Delta t}{\Delta x} + \frac{v\Delta t}{\Delta y} \leq 1. \tag{3.5.6}$$

This can be used in (3.5.5) and we obtain

$$\left[|\mathbf{u}|^2 + \frac{2p - \tau_{xx} - \tau_{yy}}{\rho}\right] + \sigma^2 K = O(\varepsilon) \tag{3.5.7}$$

Thus, the lattice speed σ must satisfy

$$\sigma = K_c\sqrt{\left|\frac{\tau_{xx}+\tau_{yy}-2p}{\rho} - |\mathbf{u}|^2\right|}, \quad K_c = \frac{1}{\sqrt{K}} \geq 1. \tag{3.5.8}$$

If the pressure p has to be uniquely defined, one requires that $\tau_{xx} + \tau_{yy} = 0$; see (3.3.14). Thus, in these fluid models, (3.5.8) reduces to

$$\sigma = K_c\sqrt{\left|\frac{-2p}{\rho} - |\mathbf{u}|^2\right|}, \quad K_c = \frac{1}{\sqrt{K}} \geq 1 \tag{3.5.9}$$

As a result, the value σ is modified and changes in each iteration as defined through (3.5.9).

Finally, in the Finite Difference Lattice Boltzmann Method (FDLBM) adopted here, the iteration and recovery of the pressure field is similar to the SIMPLE method of Patankar and Spalding (Patankar (1981); Patankar and Spalding (1972)). As is well known, the SIMPLE method is a guess-and-correct procedure for the calculation of the pressure field. In each iteration, the velocity field is obtained from the first guessed pressure field. Next, using the corrected velocity field, it is possible to find the corrected pressure and this process continues till a very small or zero mass residual is obtained, since the zero mass residual demonstrates that the divergence of the velocity vector field is zero. In FDLBM, the criteria, which is the mass residual in the SIMPLE method, is the difference between the sum of the distribution functions and the fixed density; see Eq. (3.3.4). Thus, the correction of the pressure field and the subsequent correction of the velocity field continues till a small or zero difference exists between this sum and the density.

Chapter 4

Isothermal flows of Bingham fluids: steady flow in a lid-driven cavity and in a pipe of square cross-section

4.1 Simulation of the flow of a Newtonian fluid in a lid-driven cavity with FDLBM

Flows of fluids inside lid driven cavities have been the subject of extensive computational and experimental studies over several decades (Ghia et al. (1982), Botella and Peyret (1998), Bruneau and Jouron (1990), Deng et al. (1994), Sahin and Owens (2003), Hou et al. (1995)). The lid-driven square cavity flow has been used as a benchmark problem for many numerical methods as it covers a wide range of complex hydrodynamics encompassing recirculation, different vortices structures, singularity, transition, and instability. The lid-driven cavity flow is the motion of a fluid inside a square cavity created by a constant translational velocity of one side while the other sides remain at rest (Fig.4.1). In the present analysis, we have taken

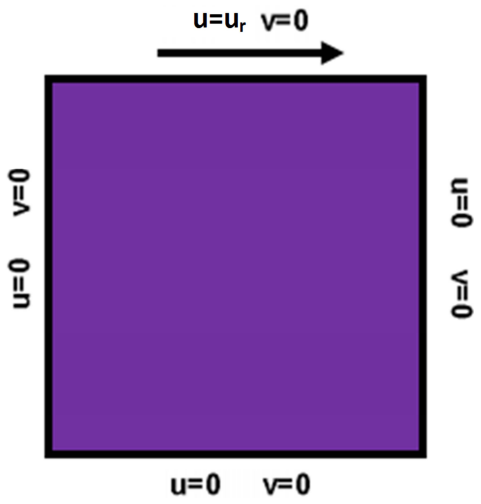

Fig. 4.1 Geometry of lid-driven cavity

the fluid to be the incompressible Newtonian fluid and the flow as laminar. Further, the flow is steady, isothermal, two dimensional and the velocity field is divergence free.

4.1.1 Dimensional equations

Based on the above assumptions, denoting by $\bar{\mathbf{u}} = u\mathbf{i} + v\mathbf{j}$ the velocity field, ρ the density, τ_{ij} the stresses and p is the pressure, Cauchy's equations for an incompressible fluid are:

$$\frac{\partial u}{\partial x} + \frac{\partial v}{\partial y} = 0 \ , \tag{4.1.1}$$

$$\rho\left(u\frac{\partial u}{\partial x} + v\frac{\partial u}{\partial y}\right) = -\frac{\partial p}{\partial x} + \left(\frac{\partial \tau_{xx}}{\partial x} + \frac{\partial \tau_{xy}}{\partial y}\right) \ , \tag{4.1.2}$$

$$\rho\left(u\frac{\partial v}{\partial x} + v\frac{\partial v}{\partial y}\right) = -\frac{\partial p}{\partial y} + \left(\frac{\partial \tau_{xy}}{\partial x} + \frac{\partial \tau_{yy}}{\partial y}\right) + \rho g\cdot \tag{4.1.3}$$

Now, let pressure (p) be written as the sum $p = p_s + p_d$, where the static part p_s accounts for gravity alone, and p_d is the dynamic part. Thus,

$$-\frac{\partial p_s}{\partial y} = \rho g \cdot \tag{4.1.4}$$

The extra stresses are obtained as follows:

$$\tau_{xx} = 2\eta\left(\frac{\partial u}{\partial x}\right),\ \tau_{yy} = 2\eta\left(\frac{\partial v}{\partial y}\right),\ \tau_{xy} = \eta\left(\frac{\partial u}{\partial y} + \frac{\partial v}{\partial x}\right)\ , \tag{4.1.5}$$

where η is the dynamic viscosity.

4.1.2 Dimensional boundary conditions

The flow domain is given by $\Omega = (0,L)\times(0,L)$, and the boundary $\Gamma = \partial\Omega$. Γ_1 is the subset $\Gamma_1 = \{\mathbf{x}|\mathbf{x} = \{x,y\}, x = 0\,\text{or}\,L, 0 \le y \le L\}$. $\Gamma_2 = \{\mathbf{x}|\mathbf{x} = \{x,y\}, 0 \le x \le L, y = 0\}$ and $\Gamma_3 = \{\mathbf{x}|\mathbf{x} = \{x,y\}, 0 \le x \le L, y = L\}$. The boundary condition for the velocity is straightforward: $\mathbf{u}|_{\Gamma_1} = \mathbf{u}|_{\Gamma_2} = 0$ and $\mathbf{u}|_{\Gamma_3} = u_r\mathbf{i}\cdot$

4.1.3 Non-Dimensional equations

In order to proceed to the numerical solution of the system (Eqs.(4.1.1),(4.1.2), and (4.1.3)) with the boundary conditions, the following non dimensional variables are introduced:

$$\bar{x} = \frac{x}{L},\ \bar{y} = \frac{y}{L},\ \bar{u} = \frac{u}{u_r},\ \bar{v} = \frac{v}{u_r},\ \bar{p_d} = \frac{p_d}{\rho u_r^2}\ , \tag{4.1.6}$$

where u_r is the the speed of the upper wall. By substitution of Eq.(4.1.6) in Eqs.(4.1.1),(4.1.2), (4.1.3), and dropping the bar notation for convenience, the following system of non-dimensional equations is derived:

$$\frac{\partial u}{\partial x}+\frac{\partial v}{\partial y}=0\ , \tag{4.1.7}$$

$$\left(u\frac{\partial u}{\partial x}+v\frac{\partial u}{\partial y}\right)=-\frac{\partial p_d}{\partial x}+\frac{1}{\mathrm{Re}}\left(\frac{\partial^2 u}{\partial x^2}+\frac{\partial^2 u}{\partial y^2}\right)\ , \tag{4.1.8}$$

$$\left(u\frac{\partial v}{\partial x}+v\frac{\partial v}{\partial y}\right)=-\frac{\partial p_d}{\partial y}+\frac{1}{\mathrm{Re}}\left(\frac{\partial^2 v}{\partial x^2}+\frac{\partial^2 v}{\partial y^2}\right)\ . \tag{4.1.9}$$

The Reynolds number is given by:

$$\mathrm{Re}=\frac{\rho\, u_r\, L}{\eta}\cdot \tag{4.1.10}$$

4.1.4 Non-Dimensional boundary conditions

The flow domain is given by $\Omega=(0,1)\times(0,1)$, and the boundary $\Gamma=\partial\Omega$. Γ_1 is the subset $\Gamma_1=\{\mathbf{x}|\mathbf{x}=\{x,y\},x=0\,\text{or}\,1,0\leq y\leq 1\}$. $\Gamma_2=\{\mathbf{x}|\mathbf{x}=\{x,y\},0\leq x\leq 1,y=0\}$ and $\Gamma_3=\{\mathbf{x}|\mathbf{x}=\{x,y\},0\leq x\leq 1,y=1\}$. The boundary condition for the velocity is straightforward: $\mathbf{u}|_{\Gamma_1}=\mathbf{u}|_{\Gamma_2}=0$ and $\mathbf{u}|_{\Gamma_3}=1\cdot$

4.1.5 Results and validation

The FDLBM has been utilised to simulate the lid-driven cavity flow problem at different Reynolds numbers (Re = 100, 400 and 1000). An extensive mesh testing procedure has also been conducted to guarantee a grid independent solution. Four different mesh combinations were explored for the case of Re = 1000. It was confirmed that the grid size (200*200) ensures a grid independent solution as portrayed in Fig.4.2. To check the accuracy of the present results, the code was validated with published studies in the literature on the lid-driven cavity flow (Ghia et al. (1982) - Hou et al. (1995)). The results in Table 4.1 show a good agreement to within 2-3 significant figures in all cases. Finally, the streamlines for the studied Reynolds numbers have been presented in Fig.4.3.

4.2 Simulation of the flow of a Bingham fluid in a lid driven cavity using the FDLBM

In this section, the flow of a Bingham fluid in the cavity is simulated, using the Bingham and Papanastasiou models. The main difference between Newtonian and non-Newtonian fluids is observed in the stresses. However, the dimensional and the non-dimensional variables as well as non-dimensional equations are similar to those for Newtonian fluids. As a result, the forms of the constitutive equations and stresses of the Bingham and Papanastasiou models are explained in the following part.

The constitutive equation for an incompressible Bingham fluid is based on the assumption that the fluid remains at rest or moves as a rigid body if the second invariant of the extra stress tensor $\boldsymbol{\tau}$ is less than or equal to the yield stress τ_y. If the second invariant exceeds the yield stress, the material flows like a fluid. This second invariant is defined through

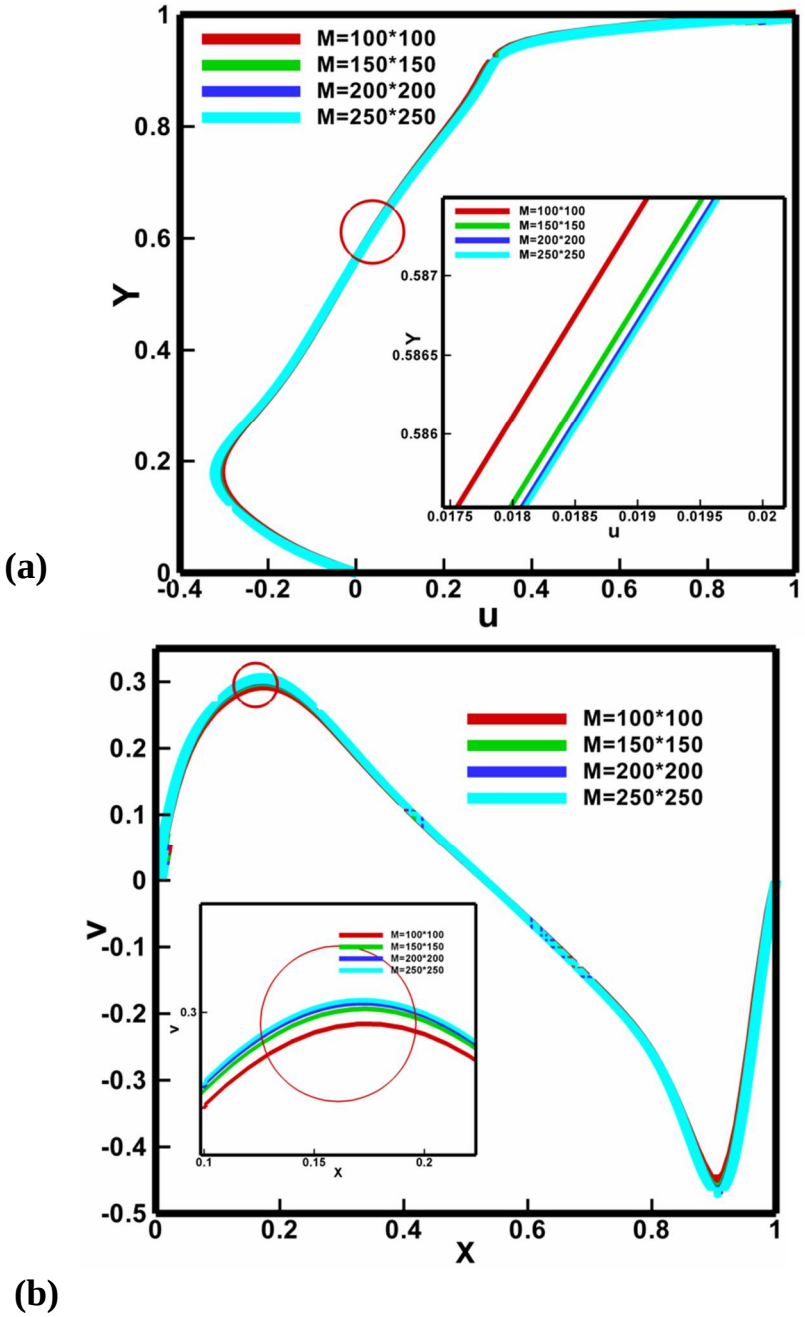

Fig. 4.2 Comparison of velocity distribution for Newtonian fluids at $x = 0.5$ and $y = 0.5$ at different mesh combinations for (a) u and (b) v respectively.

Table 4.1 (a) minimum values of u computed along $x = 0.5$ and the corresponding ordinate y_{min}, (b) maximum values of v computed along $y = 0.5$ and the corresponding abscissa x_{max}, (c) minimum values of v computed along $y = 0.5$ and the corresponding abscissa x_{min}, (d) minimum values of stream function and the corresponding coordinates x_{min}, y_{min} for Newtonian fluids.

Reference	u_{min}	y_{min}	v_{max}	x_{max}	v_{min}	x_{min}	ψ_{min}
Re=100							
Present	-0.2111	0.4591	0.1802	0.2358	-0.2571	0.8121	-0.1031
Ghia et al. (1982)	-0.2109	0.4598	0.1809	0.2354	-0.2566	0.8127	-0.1035
Botella and Peyret (1998)	-0.2140	0.4581	0.1796	0.2370	-0.2538	0.8104	-
Bruneau and Jouron (1990)	-0.2106	0.4531	0.1786	0.2344	-0.2521	0.8125	-0.1026
Deng et al. (1994)	-0.2131	-	-	0.2354	-	-	-
Sahin and Owens (2003)	-0.2139	0.4598	0.1808	0.2354	-0.2566	0.8127	-0.1035
Hou et al. (1995)	-	-	-	-	-	-	-0.1030
Re=400							
Present	-0.3296	0.2882	0.3083	0.2291	-0.4601	0.8911	-0.1162
Ghia et al. (1982)	-0.3273	0.2813	0.3020	0.2266	-0.4499	0.8594	-0.1139
Hou et al. (1995)	-	-	-	-	-	-	-0.1121
Deng et al. (1994)	-0.3275	-	0.3027	-	-0.4527	-	-
Sahin and Owens (2003)	-0.3283	0.2815	0.3044	0.2253	-0.4563	0.8621	-0.1139
Re=1000							
Present	-0.3840	0.1721	0.3765	0.1586	-0.5279	0.9105	-0.1184
Sahin and Owens (2003)	-0.38810	0.1727	0.3769	0.1573	-0.5285	0.9087	-0.1188
Ghia et al. (1982)	-0.3829	0.1719	0.3709	0.1563	-0.5155	0.9063	-0.1179
Botella and Peyret (1998)	-0.3886	0.1717	0.3769	0.1578	-0.5271	0.9092	-0.1189
Hou et al. (1995)	-	-	-	-	-	-	-0.1178
Bruneau and Jouron (1990)	-0.3764	0.1602	0.3665	0.1523	-0.5208	0.9102	-0.1163
Deng et al. (1994)	-0.38511	-	0.3769	-	-0.5228	-	-

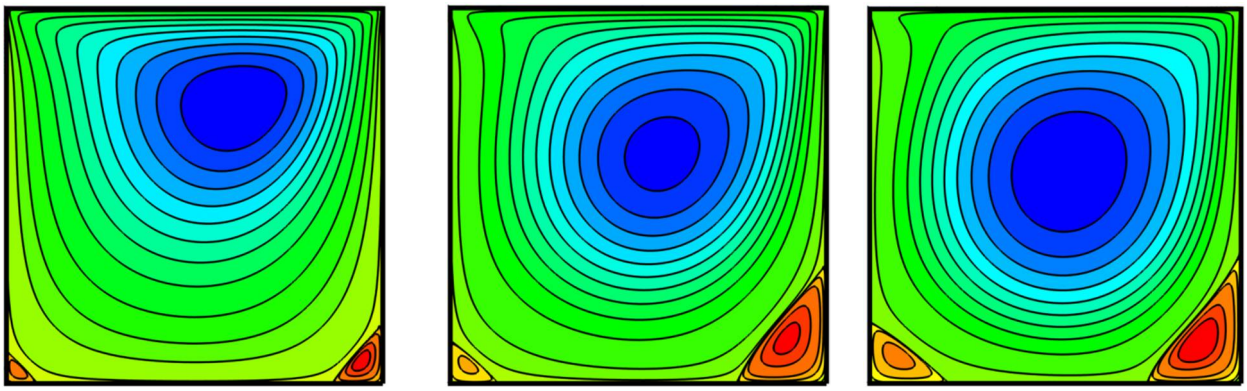

Re=100 **Re=400** **Re=1000**

Fig. 4.3 Comparison of streamlines at different Reynolds numbers

$$II(\boldsymbol{\tau}) = (1/\sqrt{2})\sqrt{\boldsymbol{\tau} : \boldsymbol{\tau}}. \tag{4.2.1}$$

Hence, using the first Rivlin-Ericksen tensor $\mathbf{A}_1$ (Rivlin and Ericksen (1955)), the rigidity condition is given by

$$\mathbf{A}_1 = \mathbf{0}, \quad II(\boldsymbol{\tau}) \leq \tau_y. \tag{4.2.2}$$

When the second invariant of the extra stress tensor exceeds the yield stress, one defines $\boldsymbol{\tau}$ as a function of the tensor $\mathbf{A}_1$ leading to the following relation:

$$\boldsymbol{\tau} = \eta \mathbf{A}_1 + \frac{\tau_y}{II(\mathbf{A}_1)}\mathbf{A}_1, \quad II(\boldsymbol{\tau}) > \tau_y \ , \ II(\mathbf{A_1}) = (1/\sqrt{2})\sqrt{\mathbf{A_1} : \mathbf{A_1}}\,. \tag{4.2.3}$$

In the Papanastasiou model, which is of interest here, the constitutive equation for the incompressible Bingham fluid is replaced by that of a material with a non-Newtonian viscosity. That is,

$$\boldsymbol{\tau} = \eta(II(\mathbf{A}_1))\mathbf{A}_1, \tag{4.2.4}$$

where the viscosity η is the sum of the constant Newtonian viscosity η_0, and a parameter dependent term. To be specific,

$$\eta(II(\mathbf{A}_1)) = \eta_0 + \frac{\tau_y}{II(\mathbf{A}_1)}\left[1 - \exp(-mII(\mathbf{A}_1))\right], \tag{4.2.5}$$

where $m > 0$ is the parameter which can be chosen arbitrarily. Note that the viscosity function in Eq.(4.2.5) is a smooth function of its argument. As far as numerical modelling is concerned, one can employ Eq.(4.2.5) and choose an appropriate value for the parameter m. A search through the literature shows that m can be as large as 10^6. Here, we examine the consequences of m = 1000 only.

Under Dirichlet boundary conditions for the velocity field which applies to the flow in a cavity, a new constitutive equation for a Bingham fluid fully equivalent to the original form can be used. This idea is due to Duvaut and Lions (1972) and Glowinski (2003) and the constitutive equation takes the form

$$\boldsymbol{\tau} = \eta\mathbf{A}_1 + \sqrt{2}\,\tau_y\,\boldsymbol{\Lambda}, \quad \mathbf{1}:\boldsymbol{\Lambda} = 0, \tag{4.2.6}$$

where one may call the second order, symmetric, tensor $\boldsymbol{\Lambda}$ the *viscoplasticity constraint tensor* (Huilgol (2015)). Note that the traceless condition $\mathbf{1}:\boldsymbol{\Lambda} = 0$ has been imposed on this tensor so that the stress tensor $\boldsymbol{\tau}$ satisfies the condition tr $\boldsymbol{\tau} = 0$. In order to demarcate the flow field into unyielded/yielded zones, one requires that the tensor $\boldsymbol{\Lambda}$ meet the following conditions:

$$\boldsymbol{\Lambda}:\boldsymbol{\Lambda} = \begin{cases} < 1, & \mathbf{A}_1 = \mathbf{0}, \\ 1, & \mathbf{A}_1 \neq \mathbf{0}. \end{cases} \tag{4.2.7}$$

These conditions are equivalent to those imposed on the stress tensor, viz., $II(\boldsymbol{\tau}) \leq \tau_y$ when $\mathbf{A}_1 = \mathbf{0}$, and $\tau_y < II(\boldsymbol{\tau})$ when $\mathbf{A}_1 \neq \mathbf{0}$. The problem of determining where the flow is rigid and where it is liquid-like has been shifted to finding the tensor $\boldsymbol{\Lambda}$ in the flow field such

that is satisfies Eq.(4.2.7). Moreover, just as the magnitude of the shear stress σ satisfies $0 \leq \sigma < \tau_y$ in the rigid core in a shearing flow, it is found that $0 \leq ||\mathbf{\Lambda}|| < 1$ in the rigid core regions. What has been proposed is important for the following reasons:

1. The constitutive equations Eqs.(4.2.6) - (4.2.7) are defined over the entire flow domain, not just where the fluid has yielded.

2. One searches for the solution velocity field $\mathbf{u}$ and the viscoplasticity constraint tensor $\mathbf{\Lambda}$ to determine the yielded/unyielded regions. There are no singularities because one is not trying to find the location of the yield surface(s) through the limit of $\mathbf{A_1}/II(\mathbf{A_1})$ as $\mathbf{A_1} \to \mathbf{0}$.

3. However, the equations of motion now involve two unknown fields: a vector field $\mathbf{u}$, and a symmetric tensor field $\mathbf{\Lambda}$. The latter requires that there should exist a connection between the velocity field $\mathbf{u}$ and $\mathbf{\Lambda}$. Under Dirichlet boundary conditions, it is possible to prove such a relation; see Duvaut and Lions (1972), Glowinski (2003), Huilgol (2015). Here, we provide a summary of the results. First, we define a set $\mathscr{M} = \left\{\boldsymbol{\mu} | \boldsymbol{\mu} = \boldsymbol{\mu}^T, \quad \boldsymbol{\mu} = (\mu_{ij})_{1\leq i,j\leq 2} \in (L^2(\Omega))^2, ||\boldsymbol{\mu}|| \leq 1 \text{ a.e. on } \Omega\right\}$ and a projection operator $P_{\mathscr{M}}$ through

$$P_{\mathscr{M}}(\mathbf{q}) = \frac{\mathbf{q}}{\max(1, ||\mathbf{q}||)}, \quad \text{a. e. in } \Omega, \quad \forall \mathbf{q} \in (L^2(\Omega))^2. \tag{4.2.8}$$

Thus, let $\mathbf{\Lambda}^0$ be given, say it is $\mathbf{0}$. If $\mathbf{\Lambda}^n$ is known, use the constitutive relation Eq.(4.2.7) to solve for the velocity field $\mathbf{u}^n$, and find $\mathbf{\Lambda}^{n+1}$ through the projection:

$$\mathbf{\Lambda}^{n+1} = P_{\mathscr{M}}\left(\mathbf{\Lambda}^n + r\tau_y \mathbf{A}_1^n\right), \tag{4.2.9}$$

where $r > 0$ is a real number to be specified (It should be noted that the acceptable values of r were reported between $0 < r < \eta/2\tau_y^2$ in Dean et al. (2007) and $0 < r < 2\eta/\tau_y^2$ in Muravleva (2015)). Successive iterations are performed till convergence is achieved to the desired level

of accuracy. Note that the yield surface is the boundary between $||\mathbf{\Lambda}|| < 1$ and $||\mathbf{\Lambda}|| = 1$. Hence, the solution of the boundary value problem delivers in the limit both the velocity field as well as the shape and location of the yield surface.

In the case of the Papanastasiou model (Papanastasiou (1987)), the non-dimensional apparent viscosity is given by

$$\eta = 1 + \frac{\mathrm{Bn}}{II(\mathbf{A}_1)}\left[1 - \exp(-mII(\mathbf{A}_1))\right], \tag{4.2.10}$$

Hence, the stresses are:

$$\tau_{xx} = 2\eta\left(\frac{\partial u}{\partial x}\right),\ \tau_{yy} = 2\eta\left(\frac{\partial v}{\partial y}\right),\ \tau_{xy} = \eta\left(\frac{\partial u}{\partial y} + \frac{\partial v}{\partial x}\right), \tag{4.2.11}$$

where

$$II(\mathbf{A}_1) = \left\{2\left[\left(\frac{\partial u}{\partial x}\right)^2 + \left(\frac{\partial v}{\partial y}\right)^2\right] + \left(\frac{\partial v}{\partial x} + \frac{\partial u}{\partial y}\right)^2\right\}^{\frac{1}{2}}. \tag{4.2.12}$$

In the case of the Bingham model (Huilgol (2015)), the non-dimensional stresses are given by

$$\tau_{xx} = \left[2\left(\frac{\partial u}{\partial x}\right) + \sqrt{2}\ \mathrm{Bn}\Lambda_{xx}\right]\ , \tag{4.2.13a}$$

$$\tau_{yy} = \left[2\left(\frac{\partial v}{\partial y}\right) + \sqrt{2}\ \mathrm{Bn}\Lambda_{yy}\right]\ , \tag{4.2.13b}$$

$$\tau_{xy} = \left[\left(\frac{\partial u}{\partial y} + \frac{\partial v}{\partial x}\right) + \sqrt{2}\ \mathrm{Bn}\Lambda_{xy}\right]\ , \tag{4.2.13c}$$

The non-dimensional parameters for the problem are as follows:

Reynolds number:

$$\mathrm{Re} = \frac{\rho\, u_r L}{\eta}, \tag{4.2.14}$$

Bingham number:

$$\mathrm{Bn} = \frac{\tau_y L}{\eta\, u_r}. \tag{4.2.15}$$

4.2.1 Simulation of the flow of a Bingham fluid in a lid driven cavity using the OSM

The lid-driven cavity filled with a Bingham fluid using the Bingham model was solved by several researchers (Sanchez (1998), Dean and Glowinski (2002), Huilgol and You (2009)) by applying the Operator Splitting Method (OSM) to solve the problem. Here, a brief explanation about the OSM is given here.

The equations of motion for an incompressible Bingham fluid are:

$$-\nabla p + \eta \triangle \mathbf{u} + \sqrt{2}\tau_y \nabla \cdot \mathbf{\Lambda} + \rho \mathbf{b} = \rho \mathbf{a}\,, \tag{4.2.16}$$

where $\triangle$ is the two-dimensional laplacian. Let U and L be the velocity and length scales respectively. Then, set $\mathbf{u} = U\mathbf{u}^*$, $\mathbf{x} = L\mathbf{x}^*$, $t = (L/U)t^*$, the Reynolds number $\mathrm{Re} = \rho UL/\eta$ and the Bingham number $\mathrm{Bn} = \sqrt{2}\tau_y L/\eta U$, with the pressure term $p = (\eta U/L)p^*$, and the body force term $\mathbf{b} = (U^2/L)\mathbf{b}^*$. After inserting these into the equations of motion, drop the asterisks. On noting that the tensor $\mathbf{\Lambda}$ is non-dimensional, and dividing both sides of Eq. (4.2.16) through by $\eta U/L^2$, one obtains:

$$\mathrm{Re}\left(\frac{\partial \mathbf{u}}{\partial t} + (\mathbf{u}\cdot\nabla)\mathbf{u}\right) - \triangle \mathbf{u} - \mathrm{Bn}\ \nabla \cdot \mathbf{\Lambda} + \nabla p = \mathrm{Re}\ \mathbf{b}, \tag{4.2.17}$$

where $\mathbf{\Lambda} \in \mathscr{M}(4.2.9)$, and

$$\mathscr{M} = \{\mu_{ij} = \mu_{ji},\ \mu_{ii} = 0,\ ||\mu|| = \sqrt{\mu_{ij}\mu_{ij}} \leq 1\}. \tag{4.2.18}$$

In Eq. (4.2.17), we have three unknowns: the velocity field $\mathbf{u}$, the tensor $\mathbf{\Lambda}$ and the pressure term p. So, it is best to decompose this into three separate problems for numerical computation. In order to simplify these further, we replace p by p/Re in what follows.

In the numerical scheme, we divide the time interval from $n\triangle t$ to $(n+1)\triangle t$ into three subintervals of equal length $\triangle t/3$. Let $\mathbf{u}^0 = \mathbf{u}_0, \mathbf{\Lambda}_0, p_0$ be given, with $\nabla \cdot \mathbf{u}^0 = 0$. For $n \geq 0$, compute the following set $\{\mathbf{u}^{n+1/3},\ p^{n+1}\}$, $\{\mathbf{u}^{n+2/3}\}$ and $\{\mathbf{u}^{n+1}, \mathbf{\Lambda}^{n+1}\}$ through

$$\frac{\mathbf{u}^{n+1/3} - \mathbf{u}^n}{\triangle t} - \frac{1}{3\mathrm{Re}}\triangle \mathbf{u}^{n+1/3} + \nabla p^{n+1} = \mathbf{f}^{n+1}, \tag{4.2.19}$$

$$\nabla \cdot \mathbf{u}^{n+1/3} = 0, \tag{4.2.20}$$

$$\frac{\mathbf{u}^{n+2/3} - \mathbf{u}^{n+1/3}}{\triangle t} - \frac{1}{3\mathrm{Re}}\triangle \mathbf{u}^{n+2/3} + \left(\mathbf{u}^{n+2/3} \cdot \nabla\right)\mathbf{u}^{n+2/3} = \mathbf{0}, \tag{4.2.21}$$

$$\frac{\mathbf{u}^{n+1} - \mathbf{u}^{n+2/3}}{\triangle t} - \frac{1}{3\mathrm{Re}}\triangle \mathbf{u}^{n+1} - \frac{\mathrm{Bn}}{\mathrm{Re}}\nabla : \mathbf{\Lambda}^{n+1} = \mathbf{0},, \tag{4.2.22}$$

$$\Lambda_{ij}^{n+1}(A_1)_{ij}\left(\mathbf{u}^{n+1}\right) = \left[(A_1)_{ij}\left(\mathbf{u}^{n+1}\right)(A_1)_{ij}\left(\mathbf{u}^{n+1}\right)\right]^{1/2}. \tag{4.2.23}$$

It is important to note that if we add Eqs. (4.2.19), (4.2.21) and (4.2.22), we get

$$\begin{aligned}\frac{\mathbf{u}^{n+1} - \mathbf{u}^n}{\triangle t} + \left(\mathbf{u}^{n+2/3} \cdot \nabla\right)\mathbf{u}^{n+2/3} &- \frac{1}{3\mathrm{Re}}\triangle\left[\mathbf{u}^{n+1/3} + \mathbf{u}^{n+2/3} + \mathbf{u}^{n+1}\right] \\ -\frac{\mathrm{Bn}}{\mathrm{Re}}\nabla : \mathbf{\Lambda}^{n+1} &+ \nabla p^{n+1} = \mathbf{f}^{n+1},\end{aligned} \tag{4.2.24}$$

which is an excellent approximation to Eq. (4.2.17). In Eqs. (4.2.19) - (4.2.23), note that $\mathbf{u}^k = \mathbf{u}(\mathbf{x}, k\triangle t)$, where $k \geq 0$ is an integer. We shall now discuss the above three problems in detail.

1. **The generalised Stokes problem**

   The first problem in Eqs. (4.2.19) and (4.2.20) constitute a problem of the Stokes type:

$$\begin{aligned} \alpha\mathbf{u} - \nu\triangle\mathbf{u} + \nabla p &= \mathbf{f}, && (4.2.25)\\ \nabla\cdot\mathbf{u} &= 0, && (4.2.26) \end{aligned}$$

   where

$$\alpha = \frac{1}{\triangle t}, \quad \nu = \frac{1}{3\mathrm{Re}}, \quad \mathbf{u} = \mathbf{u}^{n+1/3}, \quad \mathbf{f} = \mathbf{f}^{n+1} + (\mathbf{u}^n/\triangle t), \tag{4.2.27}$$

   with $\mathbf{f}^1 = \mathbf{b}$. We carry forward the final solution for $\mathbf{u}$ obtained here to the next problem as $\mathbf{u}^{n+1/3}$.

2. **The transport problem**

   Now, Eq. (4.2.21) is a nonlinear elliptic problem of the following type:

$$\alpha\mathbf{u} - \nu\triangle\mathbf{u} + \Big(\mathbf{u}\cdot\nabla\Big)\mathbf{u} = \mathbf{f}, \tag{4.2.28}$$

   where

$$\alpha = \frac{1}{\triangle t}, \quad \nu = \frac{1}{3\mathrm{Re}}, \quad \mathbf{u} = \mathbf{u}^{n+2/3}, \quad \mathbf{f} = \frac{\mathbf{u}^{n+1/3}}{\triangle t}. \tag{4.2.29}$$

   It is possible to turn Eq.(4.2.28) into a linear problem by replacing $(\mathbf{u}\cdot\nabla)\mathbf{u}$ with $(\mathbf{w}\cdot\nabla)\mathbf{u}$, where $\mathbf{w}$ is the previous value of $\mathbf{u}$. We solve this modified problem until convergence occurs, say in $m+1$ steps, and then take $\mathbf{u}^{n+2/3} = \mathbf{u}^{m+1}$ into the problems in Eqs. (4.2.22) and (4.2.23).

3. **The multiplier problem**

Finally, Eqs. (4.2.22) and (4.2.23) are of the following type:

$$\alpha\mathbf{u} - \nu\triangle\mathbf{u} - \beta\nabla\cdot\mathbf{\Lambda} = \mathbf{f}, \tag{4.2.30}$$

$$\mathbf{\Lambda} : \mathbf{A_1}(\mathbf{u}) = \left[\mathbf{A_1}(\mathbf{u}) : \mathbf{A_1}(\mathbf{u})\right]^{1/2}, \tag{4.2.31}$$

where

$$\alpha = \frac{1}{\triangle t}, \quad \beta = \frac{\mathrm{Bn}}{\mathrm{Re}}, \quad \nu = \frac{1}{3\mathrm{Re}}, \tag{4.2.32}$$

$$\mathbf{u} = \mathbf{u}^{n+1}, \quad \mathbf{\Lambda} = \mathbf{\Lambda}^{n+1}, \quad \mathbf{f} = \frac{\mathbf{u}^{n+2/3}}{\triangle t}. \tag{4.2.33}$$

The iteration to find $\mathbf{\Lambda}^{n+1}$ is based on using Eqs. (4.2.7) and (4.2.18). That is, for any $r \geq 0$, we define

$$\mathbf{\Lambda}^{m+1} = P_{\mathscr{M}}\left(\mathbf{\Lambda}^m + r\beta\mathbf{A_1}(\mathbf{u}^m)\right), \tag{4.2.34}$$

where $P_{\mathscr{M}}$ is the projection operator on the space $\mathscr{M}$, defined so that $P_{\mathscr{M}}(\boldsymbol{\mu}) = \boldsymbol{\mu}$, if $||\boldsymbol{\mu}|| < 1$, and $P_{\mathscr{M}}(\boldsymbol{\mu}) = \boldsymbol{\mu}/||\boldsymbol{\mu}||$ otherwise. Note that if we choose the initial value of the multiplier $\mathbf{\Lambda}_0$ such that $\mathbf{1} : \mathbf{\Lambda}_0 = 0$, all other iterations will also have zero trace.

As far as $\mathbf{\Lambda}^{n+1}$ is concerned, it forms the initial value $\mathbf{\Lambda}_0$ when n is upgraded to $n+1$.

4.2.2 Results and validation

The FDLBM has been utilised to simulate the lid-driven cavity flow problem of a Bingham fluid at different Reynolds numbers. An extensive mesh testing procedure was conducted to guarantee a grid independent solution. Seven different mesh combinations were explored for the case of Re = 1000 and Bn = 10. The present code was tested for grid independence by calculating the u and v velocities in the middle of the cavity. It was confirmed that the grid

size (250-250) ensures a grid independent solution as portrayed by Fig.4.4 . The accuracy of the applied code in a lid-driven cavity using the Papanastasiou model is validated through a comparison with Neofytou (2005) who chose a smaller grid size (200-200). The results are shown in Fig.4.5 where the u and v velocities profiles demonstrate the accuracy of the present simulation for Bn = 1 and Re = 100. In addition, the yielded/unyielded region and the streamlines of the FDLBM using the Papanastasiou model are validated by comparison to those of Syrakos et al. (2014) at Re = 1000 and Bn = 10 in Fig.4.6. Results of the FDLBM using the Bingham model is compared with Dean and Glowinski (2002). The streamlines and the yielded/unyielded regions in Fig.4.7 are depicted at Re = 0.53, Bn = 0.1 which refer to the values of U = 1, μ (η) =1, g (τ_y) = 0.1 in the study of Dean and Glowinski (2002) for the dimensional values of Reynolds and Bingham numbers found by Huilgol and You (2009). They stated that the acceptable values of r lie between $0 < r < \eta/2\tau_y^2$. For the studied parameters U = 1, η =1, τ_y = 0.1, r lies between $0 < r < 50$. Hence, in this study, we have selected $r = 1$.

The validation and results demonstrate that FDLBM is an appropriate method to simulate the lid-driven flow of Bingham fluids in a cavity using the Bingham model as well as the Papanastasiou model. In the case of the Bingham model, the OSM was the only applied method for the problem. Two important drawbacks of the method are the running time and the complicated algorithm. On the other hand, the only difference between the utilised algorithms of Newtonian and Bingham fluids in the FDLBM appears in the stresses; however, there is not a significant difference between the running time of the simulations of the flows of Newtonian and Bingham fluids. In the case of the Papanastasiou model, the situation is simpler, for the only difference with the Newtonian fluid in the algorithm is observed in the exponential equation of viscosity instead of a fixed value. Moreover, Syrakos et al. (2014) reported a necessary requirement for very fine grids in high values of Bingham and Reynolds

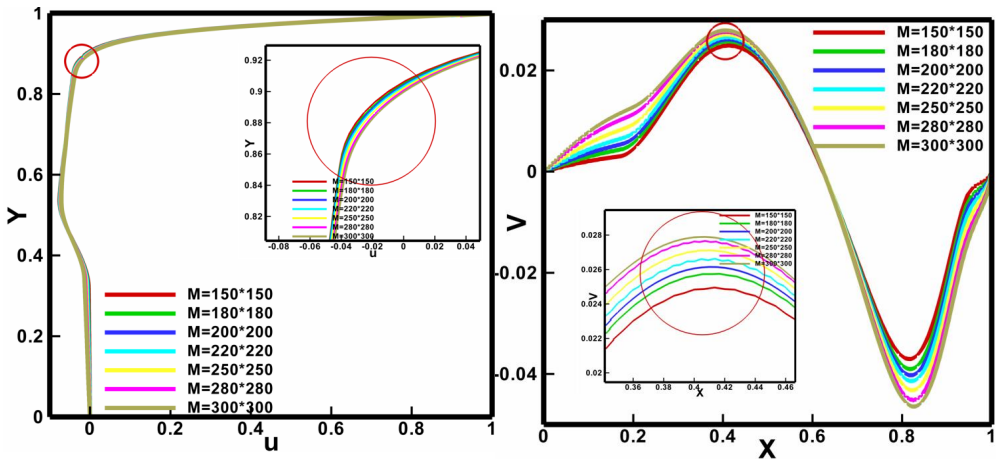

Fig. 4.4 Comparison of velocity distribution at x=0.5 and y=0.5 for (a)u and (b) v respectively at Re=1000 and Bn=10 using the Papanastasiou model ·

numbers (Re = 1000, Bn = 10) in the lid-driven cavity flow as they employed a finite volume method to solve the problem. They stated that "there is observable improvement of the yield surface as the grid density is increased, even up to the 2048*2048 grid". But, in FDLBM, Fig.4.8 shows that no changes were observed in the form and shape of the yielded/unyielded regions due to the increase in the grid sizes more than 250*250. In other words, the cited grid (250*250) is suitable for a wide range of Reynolds and Bingham numbers.

4.3 Simulation of the steady fluid flow of Bingham fluid in a pipe of square cross-section

As mentioned in the second chapter, the steady flow of a Bingham fluid in pipes has attracted the attention of many researchers in this field. In some the cited studies into the topic, the Augmented Lagrangian method (ALM) has been applied to solve the problems, for the ALM has been an effective and reliable numerical technique for solving viscoplastic flow

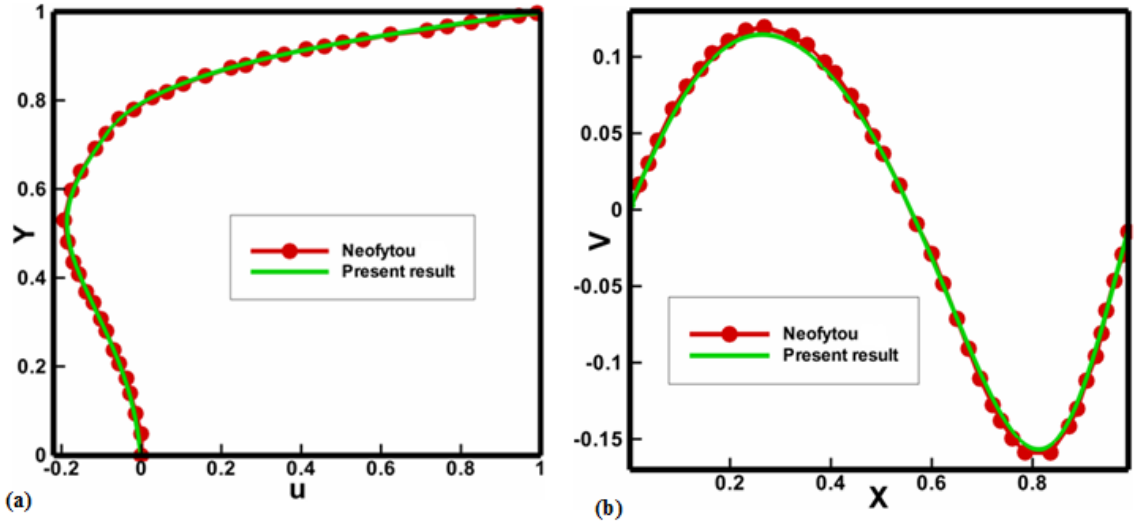

Fig. 4.5 Comparison of u and v velocities profiles in the middle of the cavity between the present results with the results of Neofytou (2005) for Re = 100 and Bn = 1 ·

problems. In fact, the method decouples the computation of the nonlinearity introduced by the complex rheological behaviour of the fluid from that of the velocity. Hence, the ALM provides us with a tool for solving the flow of a Bingham fluid, avoiding the applications of different regularised models. Moreover, it leads to an accurate prediction of the locations of the yielded and unyielded zones. Here, the steady flow of Bingham fluid in a pipe of a square cross-section (Fig.4.9), is studied by applying the method of ALM and FDLBM. First, we explain briefly the methodology of the ALM for the selected problem using the previous study by Huilgol and You (2005). Next, the problem is formulated by FDLBM and the FDLBM results are demonstrated and compared with the results obtained by Huilgol and You (2005) using ALM.

The cross-section of the pipe of infinite length with a square cross-section is shown in Fig.4.9. The flow is governed by the momentum equation as follows:

$$\frac{\partial}{\partial x}\tau_{zx} + \frac{\partial}{\partial y}\tau_{zy} = -\frac{dp}{dz} \ , \tag{4.3.1}$$

where the deviatoric stresses are given by

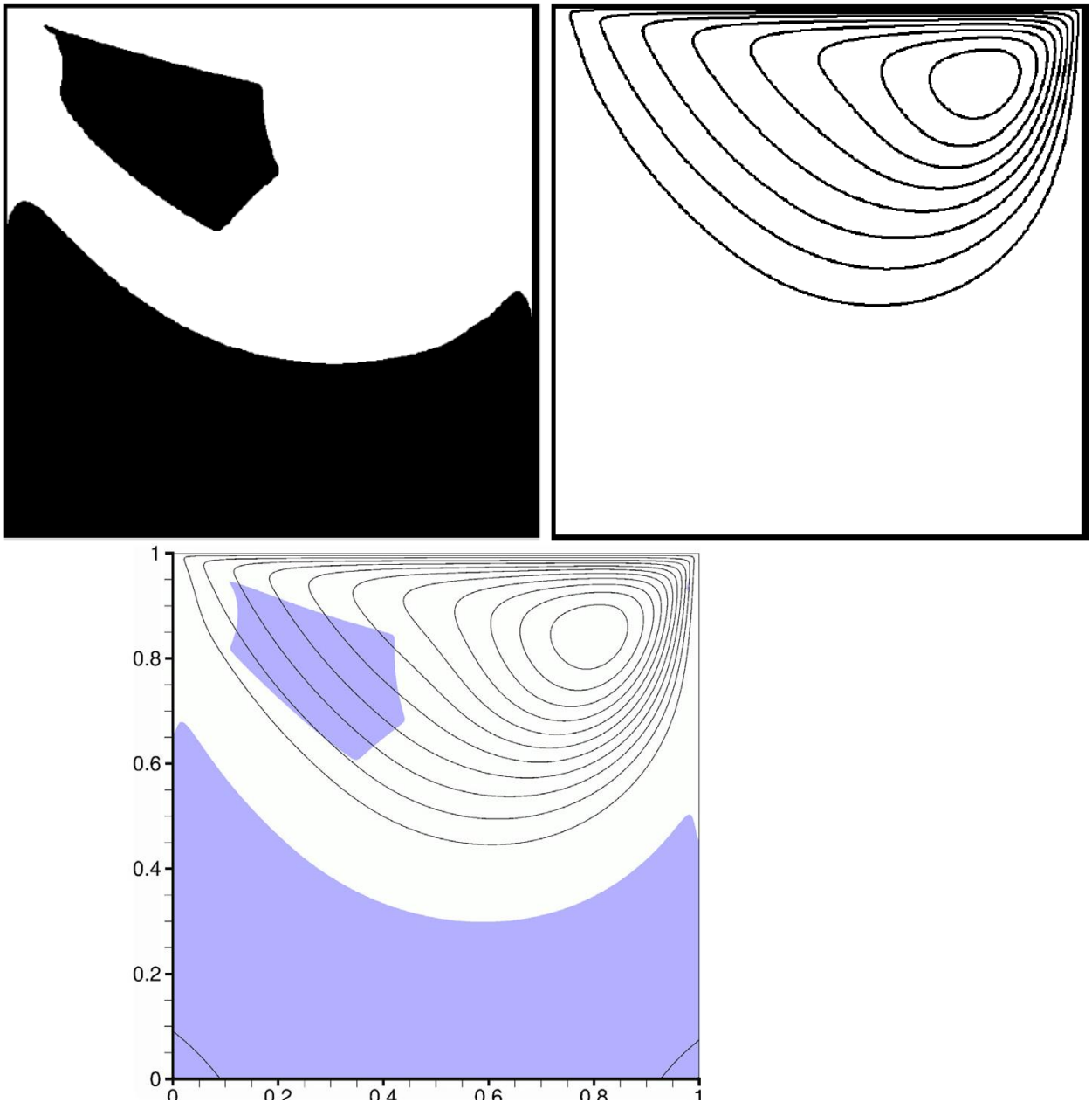

Fig. 4.6 Comparisons of the yielded/unyielded regions and streamlines between (a) the present study with the results of (b) Syrakos et al. (2014) for Re = 1000 and Bn = 10 ·

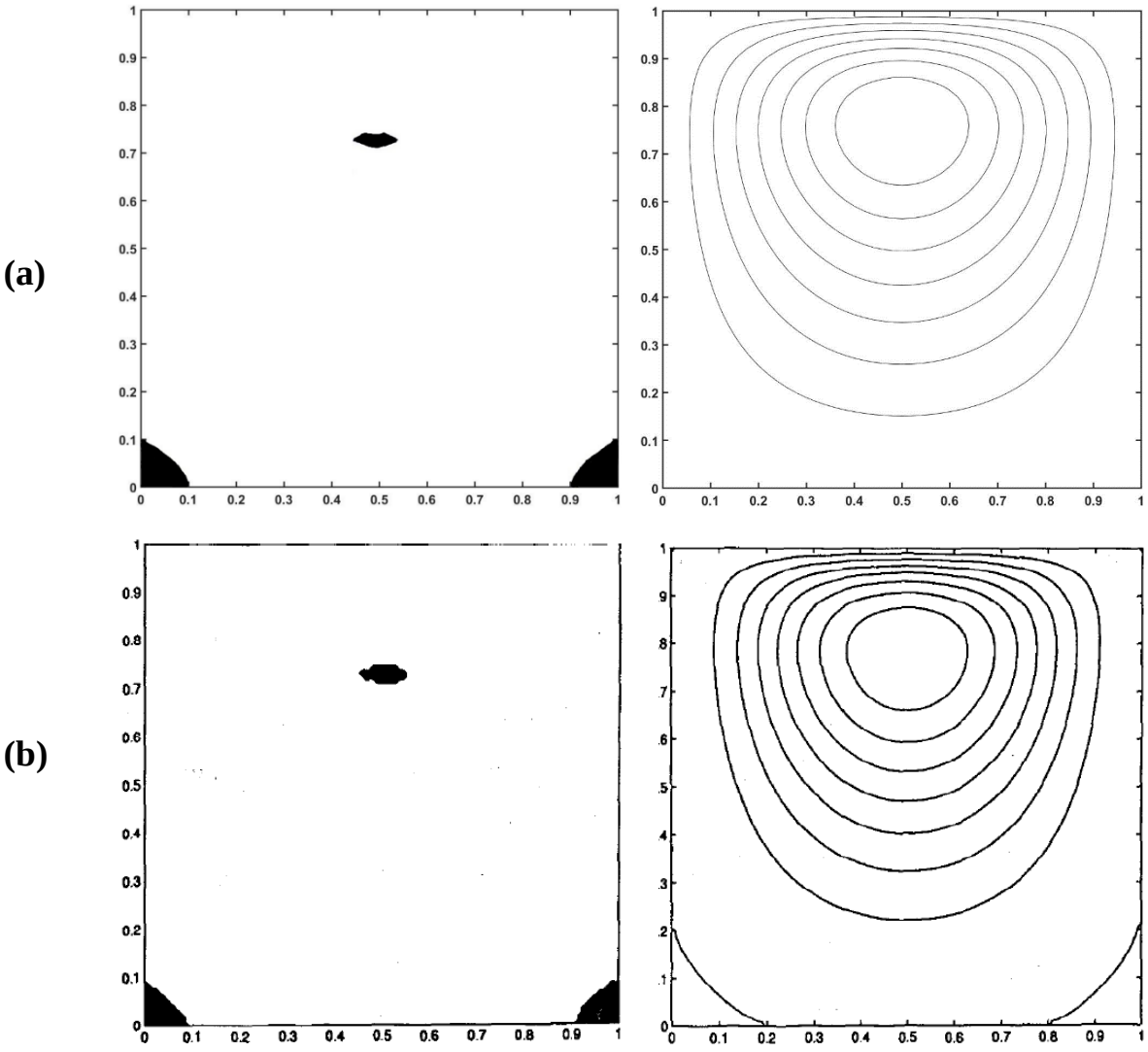

Fig. 4.7 Comparisons of the yielded/unyielded regions and streamlines between (a) the present study with the results of (b) Dean and Glowinski (2002) for Re = 0.53, Bn = 0.1 corresponding to U = 1, μ =1, g = 0.1 in Dean and Glowinski (2002) ·

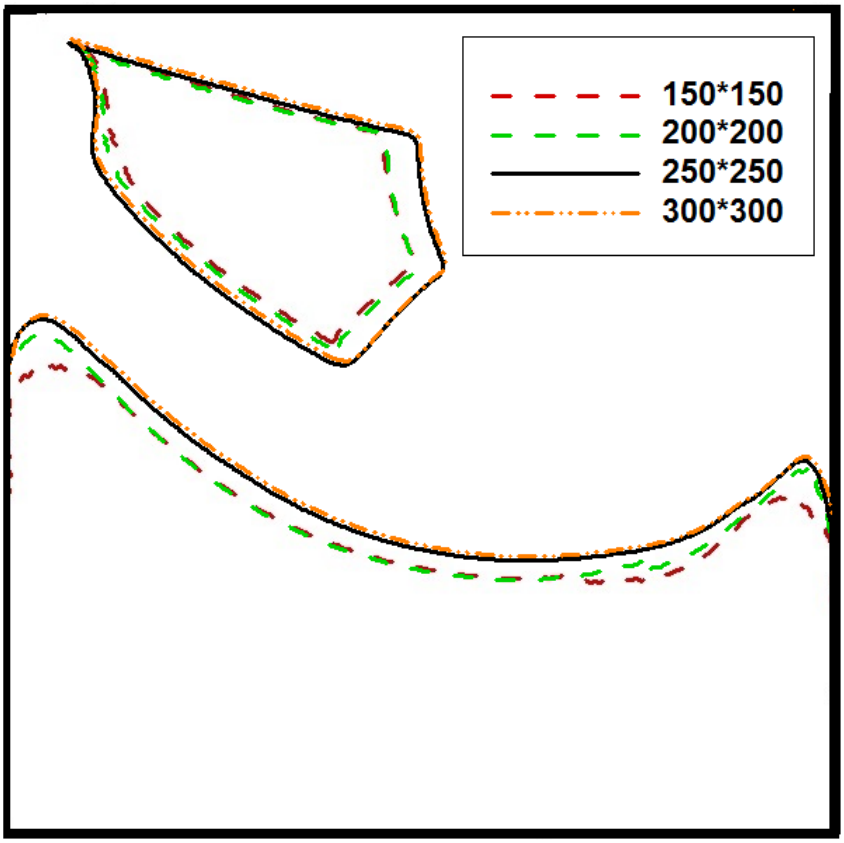

Fig. 4.8 Comparison of the yielded/unyielded regions boundaries for different grids at Re = 1000 and Bn = 10 ·

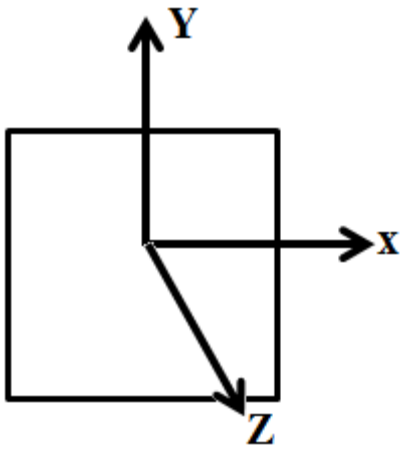

Fig. 4.9 Geometry of a pipe of square cross-section

$$\begin{cases} \mathbf{A_1} = \mathbf{0}, & II(\boldsymbol{\tau}) \leq \tau_y, \\ \boldsymbol{\tau} = \eta \mathbf{A_1} + \frac{\tau_y}{II(\mathbf{A_1})} \mathbf{A_1}, & II(\boldsymbol{\tau}) > \tau_y, \end{cases} \tag{4.3.2}$$

It should be noted that the pressure (p) is independent of (x,y) and depends on the z direction. As a result, the negative gradient of the pressure is equal to a positive constant value$(-\frac{dp}{dz} = c, c > 0)$. Moreover, $w(x,y)$ is the axial velocity and is independent of the z direction.

The non-dimensional parameters are as follows:

$$\bar{x} = \frac{x}{L},\ \bar{y} = \frac{y}{L},\ \bar{w} = \frac{w}{W},\ \ \bar{p} = \frac{p}{cL}\ , \bar{\boldsymbol{\tau}} = \frac{\boldsymbol{\tau}}{cL},\ \bar{A_1} = \frac{A_1 L}{W}\ , \tag{4.3.3}$$

where L is the length of the side of the square and W is the the characteristic velocity given by

$$W = \frac{cL^2}{\eta}\ \cdot \tag{4.3.4}$$

The flow rate (Q) is obtained through

$$Q = WL^2\ \cdot \tag{4.3.5}$$

The hydraulic diameter of a pipe (D_H) is calculated as follows:

$$D_H = \frac{4A}{P}\ \cdot \tag{4.3.6}$$

where A is the area section of the pipe and P is the wetted perimeter of the pipe. For a pipe of square cross-section, D_H is the same as the length of each side. Dropping the bar notation for convenience, the following system of non-dimensional equations is derived for the Bingham model.

$$\begin{cases} \mathbf{A_1} = \mathbf{0}, & II(\boldsymbol{\tau}) \leq Od, \\ \boldsymbol{\tau} = \mathbf{A_1} + \frac{Od}{II(\mathbf{A_1})}\mathbf{A_1}, & II(\boldsymbol{\tau}) > Od, \end{cases} \tag{4.3.7}$$

The Od parameter is the the Oldroyd number and is expressed as

$$Od = \frac{\tau_y}{cL} \cdot \tag{4.3.8}$$

While Od is the same as the Bingham number, Od is used here for it appears in Huilgol and You (2005).

For the given problem, the first Rivlin-Ericksen tensor $(\mathbf{A_1})$, the second invariants of the extra stress tensor $(II(\boldsymbol{\tau}))$, and the $(II(\mathbf{A_1}))$ are set as follows:

$$II(\boldsymbol{\tau}) = \sqrt{{\tau_{zx}}^2 + {\tau_{yx}}^2} \ , \tag{4.3.9}$$

$$\mathbf{A_1} = \boldsymbol{\nabla}\mathbf{w} = \frac{\partial w}{\partial x}\mathbf{i} + \frac{\partial w}{\partial y}\mathbf{j} \ , \tag{4.3.10}$$

$$II(\mathbf{A_1}) = |\nabla \mathbf{w}| = \sqrt{\left(\frac{\partial w}{\partial x}\right)^2 + \left(\frac{\partial w}{\partial y}\right)^2} \cdot \tag{4.3.11}$$

Note that in this problem, the normal stresses τ_{xx}, τ_{yy} and τ_{zz} are zero.

4.3.1 ALM for this problem

The problem was solved by Huilgol and You (2005) and here a brief explanation about the method is provided. It is assumed that all velocity fields have a non-zero component in the axial direction only and that they vanish on the boundary of the pipe. Let $w = w(x,y)$ be the true streamwise velocity, $v = v(x,y)$ be any trial velocity field, and Ω be the cross-section of

a pipe, bounded in $\mathbb{R}^2$. The viscous dissipation functional is given by

$$a(w, v-w) = \int_\Omega \eta(\dot{\gamma}) \nabla w \cdot \nabla (v-w)\, da \cdot \tag{4.3.12}$$

The yield stress dissipation functional has the form

$$j(w) = Od \int_\Omega |\nabla w|\, da, \tag{4.3.13}$$

and the pressure drop functional is given by

$$(c, v-w) = \int_\Omega c(v-w)\, da \cdot \tag{4.3.14}$$

In Eqs (4.3.12)–(4.3.14), ∇ is the two-dimensional gradient operator, the shear rate is given by $\dot{\gamma} = |\nabla w|$, and $\eta(\dot{\gamma})$ equals to one.

It can be shown that the solution $w = w(x,y)$ across the cross-section of the pipe satisfies the following variational inequality (Duvaut and Lions (1972)):

$$a(w, v-w) + j(v) - j(w) \geq (c, v-w). \tag{4.3.15}$$

In addition, it is demonstrated from the variational inequality that the true velocity field satisfies the energy equation:

$$a(w, w) + j(w) = (c, w). \tag{4.3.16}$$

Thus, the true velocity field w can be obtained by minimising the functional

$$\Phi(v) = \frac{1}{2} \int_\Omega |\nabla v|^2\, da + Od \int_\Omega |\nabla v|\, da - \int_\Omega v\, da \cdot \tag{4.3.17}$$

However, the functional $\Phi(v)$ cannot be minimised directly because the yield stress dissipation functional $j(v)$ is a non-differentiable function of v, when the fluid moves as a rigid body or is at rest, where $|\nabla v| = 0$. This difficulty can be circumvented by using a Lagrangian functional.

Thus, let $\mathbf{q}$ be any two-dimensional vector field and the constraint be $\nabla v - \mathbf{q} = \mathbf{0}$. The associated Lagrangian functional is:

$$\mathfrak{L}(v, \mathbf{q}, \boldsymbol{\lambda}) = \Phi(v, \mathbf{q}) + (\boldsymbol{\lambda}, \nabla v - \mathbf{q}), \tag{4.3.18}$$

where

$$(\boldsymbol{\lambda}, \nabla v - \mathbf{q}) = \int_{\Omega} \boldsymbol{\lambda} \cdot (\nabla v - \mathbf{q})\, da, \tag{4.3.19}$$

and $\boldsymbol{\lambda}$ is a Lagrange multiplier. Clearly, this Lagrangian functional is linear in v. In order to obtain a quadratic form to improve the convergence of the iterative scheme, the augmented Lagrangian is introduced. It is taken to be

$$\mathfrak{L}_r(v, \mathbf{q}, \boldsymbol{\lambda}) = \mathfrak{L}(v, \mathbf{q}, \boldsymbol{\lambda}) + \frac{1}{2} r \int_{\Omega} |\nabla v - \mathbf{q}|^2\, da, \tag{4.3.20}$$

where r is a non-negative parameter. In the above scheme, u is the solution of the problem under examination and $\mathbf{q} = \nabla w$.

The iteration scheme using the algorithm ALG (Glowinski (1984)) is implemented as follows:

1. $\mathbf{q}^0$ and $\boldsymbol{\lambda}^1$ are arbitrarily given in the (x, y) plane such that both vectors are square integrable over the domain Ω.

2. With $\mathbf{q}^{m-1}$, $\boldsymbol{\lambda}^m$ known, find w^m such that

$$-r\Delta w^m = 1 + \nabla\cdot\boldsymbol{\lambda}^m - r\nabla\cdot\mathbf{q}^{m-1}, \tag{4.3.21}$$

where $w^m = 0$ on $\partial\Omega$, $m = 1,2,3,\ldots$

3. The vector $\mathbf{q}^m$ is obtained as follows:

$$\begin{cases} \mathbf{q}^m = \mathbf{0}, & \text{if } Od \geq |\boldsymbol{\lambda}^m + r\nabla w^m| \ , \\ \mathbf{q}^m = \frac{\boldsymbol{\lambda}^m + r\nabla w^m}{1+r}(1 - \frac{Od}{|\boldsymbol{\lambda}^m + r\nabla w^m|}), & \text{elsewhere } \cdot \end{cases} \tag{4.3.22}$$

4. Get $\boldsymbol{\lambda}^{m+1}$ from

$$\boldsymbol{\lambda}^{m+1} = \boldsymbol{\lambda}^m + \rho_m(\nabla w^m - \mathbf{q}^m), \tag{4.3.23}$$

where ρ_m is a sequence of constants. The parameters r and ρ_m are set to unity to acquire an optimal convergence performance (Glowinski (1984)).

4.3.2 FDLBM for this problem

With consideration to the problem, Eqs. (3.4.7) - (3.4.20) are modified as follows:

$$\sum_{\alpha=0}^{14} f_\alpha^{eq} = \rho, \tag{4.3.24}$$

$$\sum_{\alpha=0}^{14} f_\alpha^{eq}\boldsymbol{\xi}_\alpha = \rho\mathbf{u}, \quad \mathbf{u} = w\mathbf{k}, \tag{4.3.25}$$

$$\sum_{\alpha=0}^{14} f_\alpha^{eq}\boldsymbol{\xi}_\alpha\otimes\boldsymbol{\xi}_\alpha = \mathbf{M}, \tag{4.3.26}$$

$$\sum_{\alpha=0}^{14} f_\alpha^{(n)} = 0, \quad n \geq 1, \tag{4.3.27}$$

$$\sum_{\alpha=0}^{14} f_\alpha^{(n)}\boldsymbol{\xi}_\alpha = \mathbf{0}, \quad n \geq 1. \tag{4.3.28}$$

Here,

$$\mathbf{M} = \begin{bmatrix} -T_{xx} & 0 & T_{xz} \\ 0 & -T_{yy} & T_{yz} \\ T_{xz} & T_{yz} & \rho w^2 - T_{zz} \end{bmatrix}. \tag{4.3.29}$$

Hence, we have

$$A_0 = \rho - \frac{\rho w^2}{\sigma^2} + \frac{T_{xx} + T_{yy} + T_{zz}}{\sigma^2}, \quad A_1 = A_2 = 0. \tag{4.3.30}$$

$$\mathbf{B}_1 = \frac{\rho w}{2\sigma^2}\mathbf{k}, \quad \mathbf{B}_2 = \mathbf{0}. \tag{4.3.31}$$

$$\mathbf{C}_1 = \begin{bmatrix} C_{11} & 0 & 0 \\ 0 & C_{22} & 0 \\ 0 & 0 & C_{33} \end{bmatrix}, \quad C_{11} = -\frac{1}{2\sigma^4}(T_{xx}), \tag{4.3.32}$$

$$C_{22} = -\frac{1}{2\sigma^4}(T_{yy}).\,, \quad C_{33} = \frac{1}{2\sigma^4}(\rho w^2 - T_{zz}). \tag{4.3.33}$$

Finally,

$$\mathbf{C}_2 = \begin{bmatrix} 0 & C_{12} & C_{13} \\ C_{21} & 0 & C_{23} \\ C_{31} & C_{32} & 0 \end{bmatrix}, \quad C_{12} = C_{21} = 0, \tag{4.3.34}$$

$$C_{23} = C_{32} = -\frac{1}{16\sigma^4}(T_{yz}), \quad C_{13} = C_{31} = -\frac{1}{16\sigma^4}(T_{xz}). \tag{4.3.35}$$

It has been mentioned earlier that $\tau_{xx} = \tau_{yy} = \tau_{zz} = 0$. Hence, we have

$$T_{xz} = \tau_{xz}, \quad T_{yz} = \tau_{yz}, \quad T_{xx} = T_{yy} = T_{zz} = -p \cdot \tag{4.3.36}$$

The Bingham model is utilised for the constitutive equation using the Eqs.(4.2.6) - (4.2.9) .

$$\tau_{xz} = \left[\left(\frac{\partial w}{\partial x} \right) + \sqrt{2}\ \mathrm{Od}\Lambda_{xz} \right] \ , \tag{4.3.37}$$

$$\tau_{yz} = \left[\left(\frac{\partial w}{\partial y} \right) + \sqrt{2}\ \mathrm{Od}\Lambda_{yz} \right] \cdot \tag{4.3.38}$$

We update the tensor $\mathbf{\Lambda}$ using the projection operator.

$$\mathbf{\Lambda}^{n+1} = P_{\mathscr{M}} \left(\mathbf{\Lambda}^{n} + rOd\mathbf{\Lambda}_1^{n} \right) \cdot \tag{4.3.39}$$

The chosen value of r is given below.

4.3.3 Results of the simulation using FDLBM

The FDLBM has been applied to simulate the steady flow of a Bingham fluid in a pipe of square cross-section. In contrast with the ALM, a 3D simulation was utilised for this problem. However, it should be noted that the running time for the 3D simulation and an appropriate mesh (50-50-50) was not excessive and was just 584 seconds, using a PC. The present code was tested for grid independence by calculating the plug velocity in the middle of the pipe. It was confirmed that the grid size (50-50-50) ensures a grid independent solution as portrayed in Table 4.2.

Figs. (4.10, 4.11, 4.12, and 4.13) demonstrate the effect of the increase in the Od number on the velocity profile in two and three dimensional contours and also the yielded/ unyielded regions have been found using the the tensor $\mathbf{\Lambda}$. The Figs. (4.10, 4.11, 4.12, and 4.13) display the unyielded regions in the shape of a circular plug zone in the centre and also in the corners of the cavity. The cited parts extend and the velocity magnitude drops as the Od number increases from Od = 1 to 5. The accuracy of the applied code in the problem is validated through a comparison with the results due to Huilgol and You (2005). The velocity profile

in the square pipe at $Od = 0.2$ in Fig.4.11 demonstrates a great deal of similarity with the Figs.8 in the study of Huilgol and You (2005). In addition, the plug velocity and the flow rate for different Od numbers in the Table. 4.3 show a good agreement with the Table. 7 in the study of Huilgol and You (2005). Finally, the velocity surface and the 3D and 2D contours of velocities at $Od = 0.4$ evidently confirm the accuracy of the values in the Table. 4.3.

In addition, we define S_P as the distance along the diagonal direction from the centre of the square pipe to the border of the yielded zone, and S_d as the distance along the diagonal direction from the centre of the square pipe to the border of the dead zone (Fig. 4.14). The values of S_p and S_d for different Od numbers are compared in the Table.4.4 with the Fig.16 in the study of Huilgol and You (2005). It was mentioned that the acceptable values of r in Eq. 4.3.39 lie between $0 < r < \eta/2\tau_y^2$ and the studied parameters are $Od = 0.2$ and 0.4, c=1, $\eta = 1$. Thus, $0 < r < 50$ for $Od = 0.1$, $0 < r < 12.5$ for $Od = 0.2$, $0 < r < 3$ for $Od = 0.4$, and $0 < r < 2$ for $Od = 0.5$. Hence, in this study, we have selected the $r = 1$.

In addition, our results have been compared with the study of Moyers-Gonzalez and Frigaard (2004) where they studied the problem for the hydraulic diameter of $D_H = 1$. In Fig. 4.15, we show the obtained results for $Od = 0.2$ and demonstrate that the velocity surfaces have a good agreement with those in Fig. 4 in Moyers-Gonzalez and Frigaard (2004). It should be noted that the Bingham number B defined in Moyers-Gonzalez and Frigaard (2004) is identical to the Oldroyd number Od used here. On the other hand, the comparison between Figs. 4.11 and 4.15 indicates that the decrease in the hydraulic diameter from $D_H = 2$ to 1 causes the unyielded sections to enlarge and the plug velocity to fall considerably.

The comparison between the ALM and the FDLBM demonstrates the advantages of the FDLBM clearly. In contrast with the ALM, the Bingham model is applied directly to the stresses in FDLBM and the unyielded region is shown clearly. In addition, the 3D simulation generates a better vision of the velocity profile and the plug velocity in the z direction, not only in the cross-section of the pipe. Moreover, in ALM, a very fine triangle mesh and a high

Table 4.2 Comparison between the plug velocities of different grid sizes at $Od = 0.2$

Grid sizes	20-20	30-301	40-40	50-50	60-60
Plug velocity(w_p)	0.147	0.135	0.128	0.121	0.121

Table 4.3 Comparison between the results of the present study usisng the FDLBM and the ALM which is studied by Huilgol and You (2005)

	Od number	Plug flow velocity (w_p)	Flow rate (Q)
Present study	0.2	0.121	0.292
Huilgol and You (2005)	0.2	0.117	0.286
Present study	0.4	1.98×10^{-2}	6.12×10^{-2}
Huilgol and You (2005)	0.4	1.92×10^{-2}	6.07×10^{-2}

computational process (4225 nodes) were employed in the results due to Huilgol and You (2005). This grid size increases the required computational capacity and time running vastly. But, in FDLBM, we applied a simple coarse square mesh which drops the running time and the CPU considerably when compared with ALM. The results compare very favorably with those in Table.7 of Huilgol and You (2005).

Table 4.4 Comparison between the present study and the results of Huilgol and You (2005) for the location of yielded/unyielded surfaces

	Od number	S_p	S_d
Present study	0.2	0.42	1.38
Huilgol and You (2005)	0.2	0.41	1.39
Present study	0.4	0.83	1.31
Huilgol and You (2005)	0.4	0.82	1.33

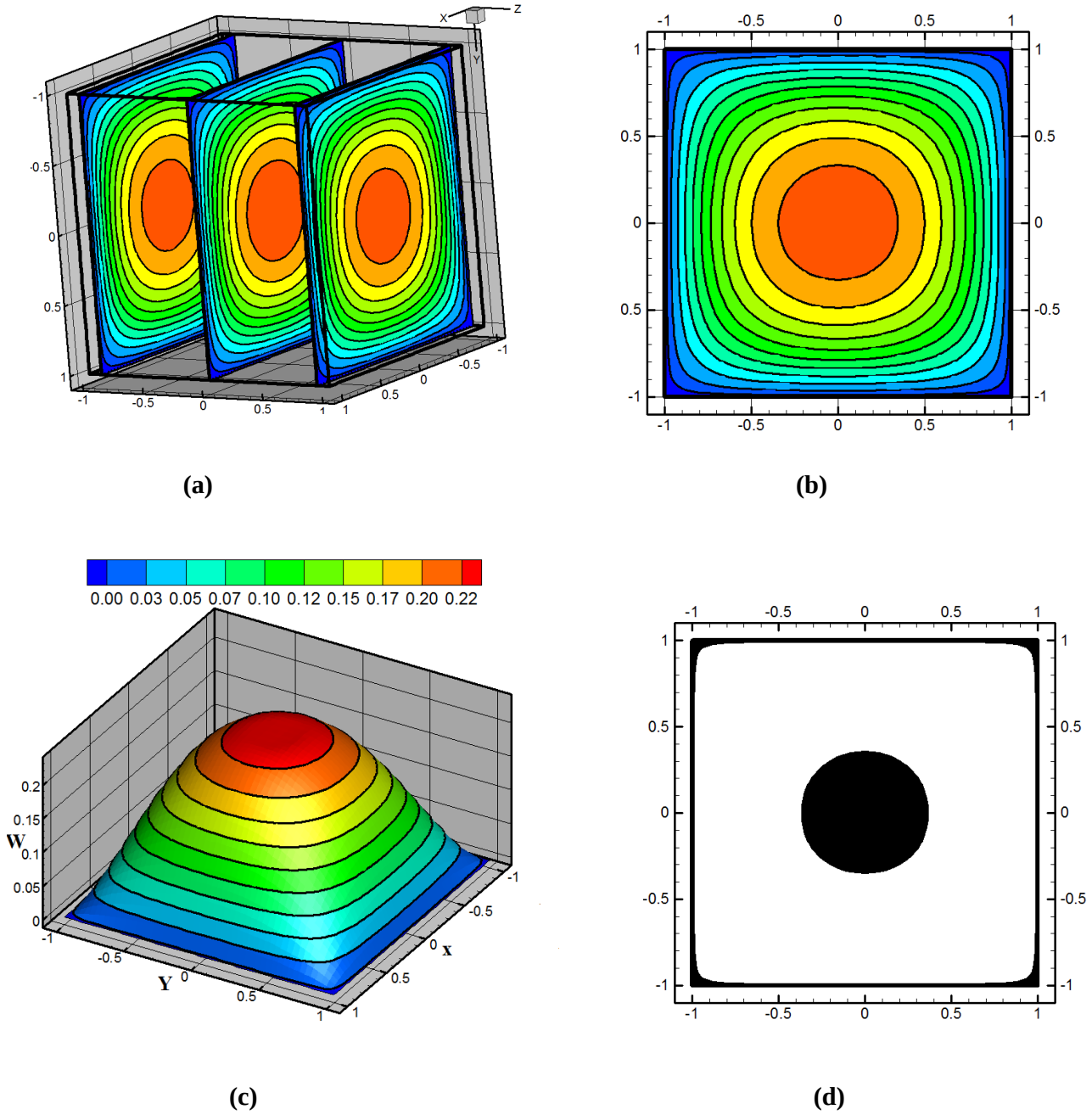

Fig. 4.10 (a) 3D contour of the square pipe flow (b) 2D contour of the square pipe flow (c) Velocity surface (d) The yielded/unyielded zones for $Od = 0.1$ and $D_H = 2$

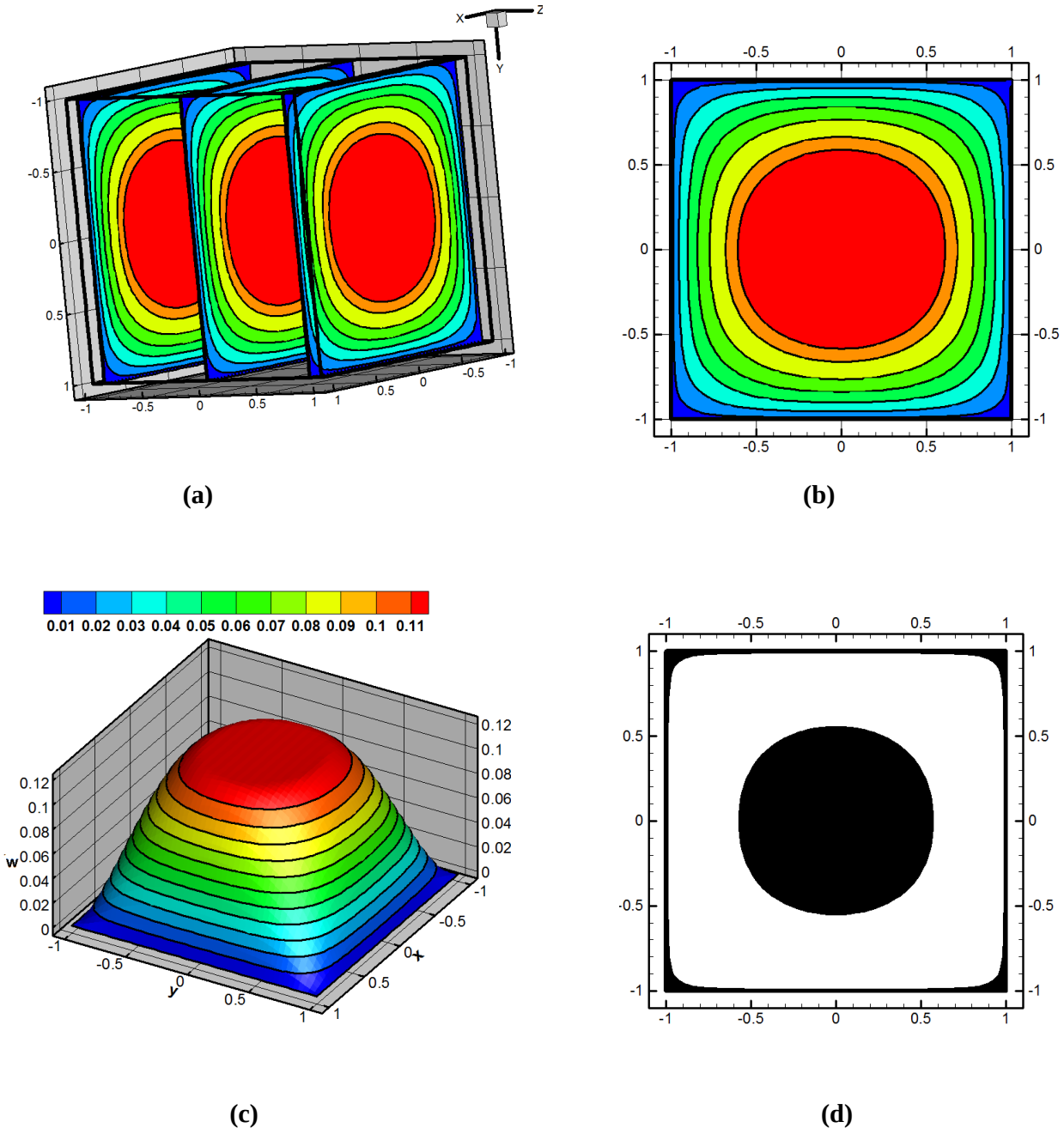

Fig. 4.11 (a) 3D contour of the square pipe flow (b) 2D contour of the square pipe flow (c) Velocity surface (d) The yielded/unyielded zones for $Od = 0.2$ and $D_H = 2$

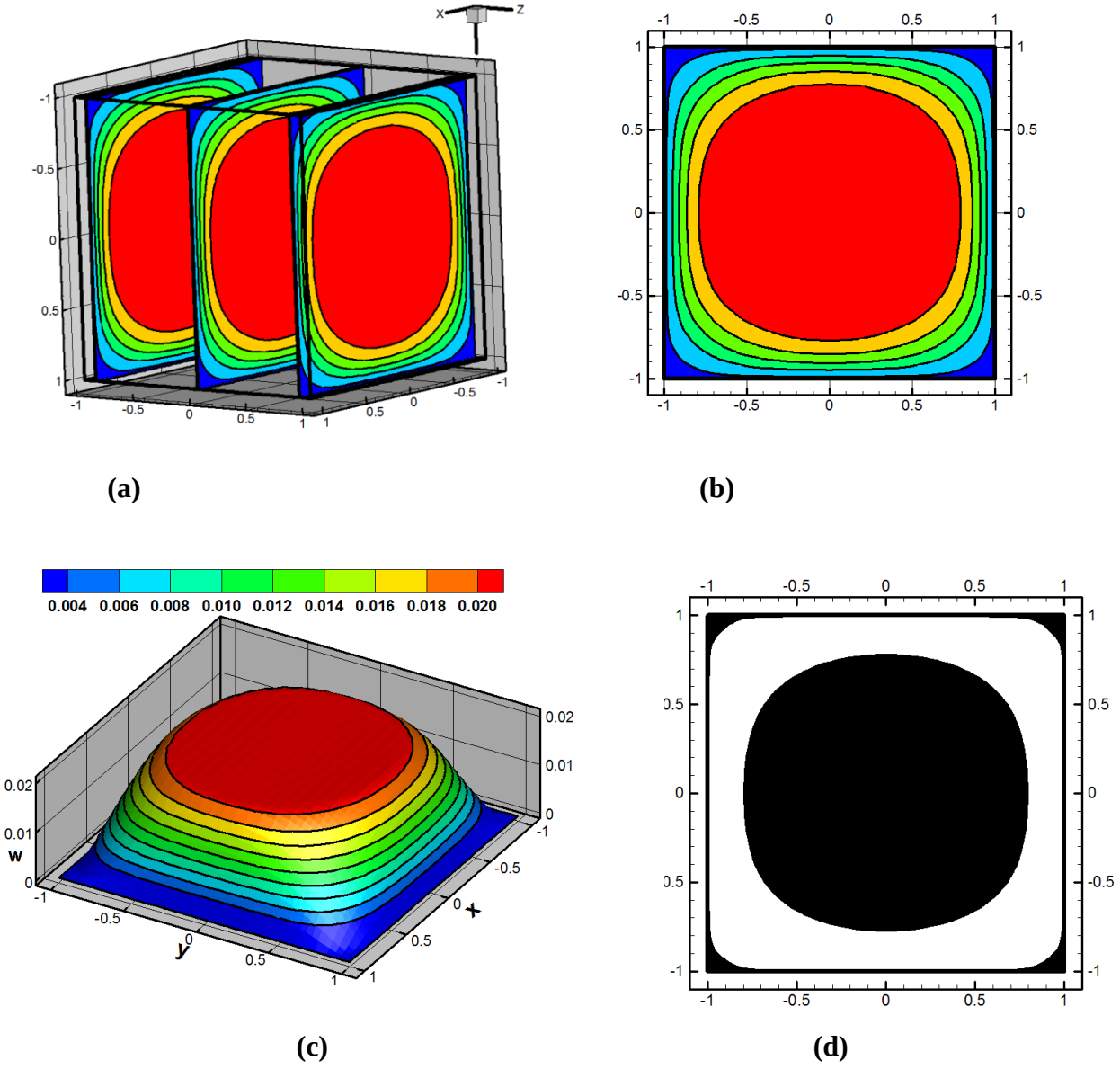

Fig. 4.12 (a) 3D contour of the square pipe flow (b) 2D contour of the square pipe flow (c) Velocity surface (d) The yielded/unyielded zones for $Od = 0.4$ and $D_H = 2$

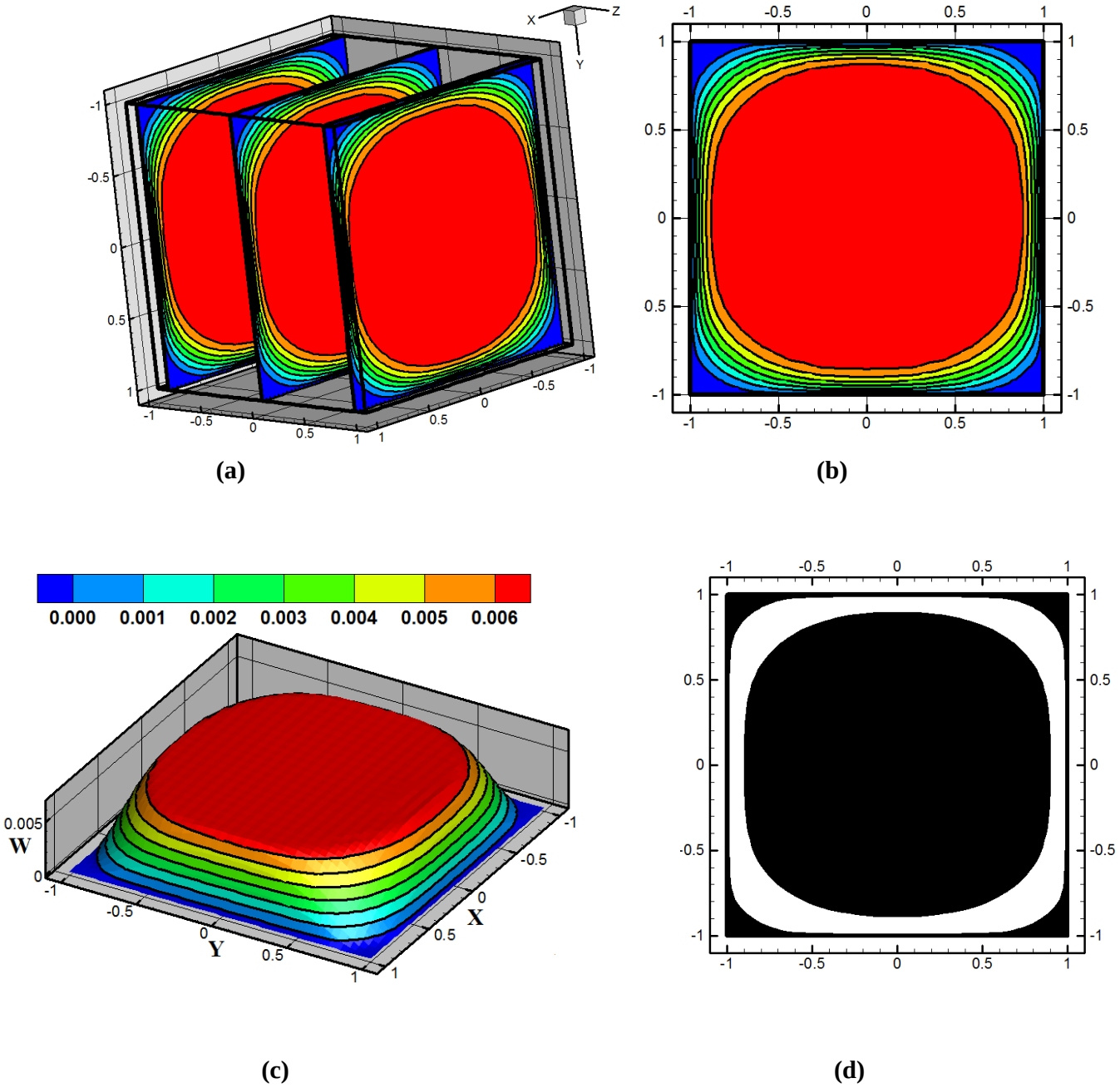

Fig. 4.13 (a) 3D contour of the square pipe flow (b) 2D contour of the square pipe flow (c) Velocity surface (d) The yielded/unyielded zones for $Od = 0.5$ and $D_H = 2$

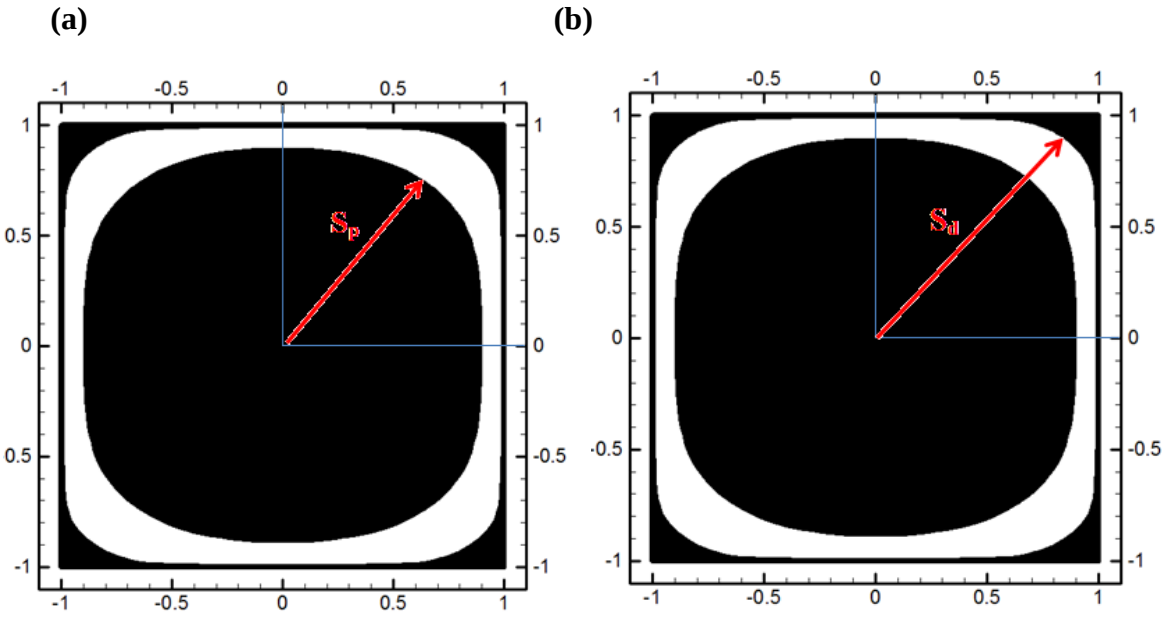

Fig. 4.14 The location of the yielded/unyielded surfaces (a) the border of plug flow zone (S_p); (b) the border of dead zone (S_d)

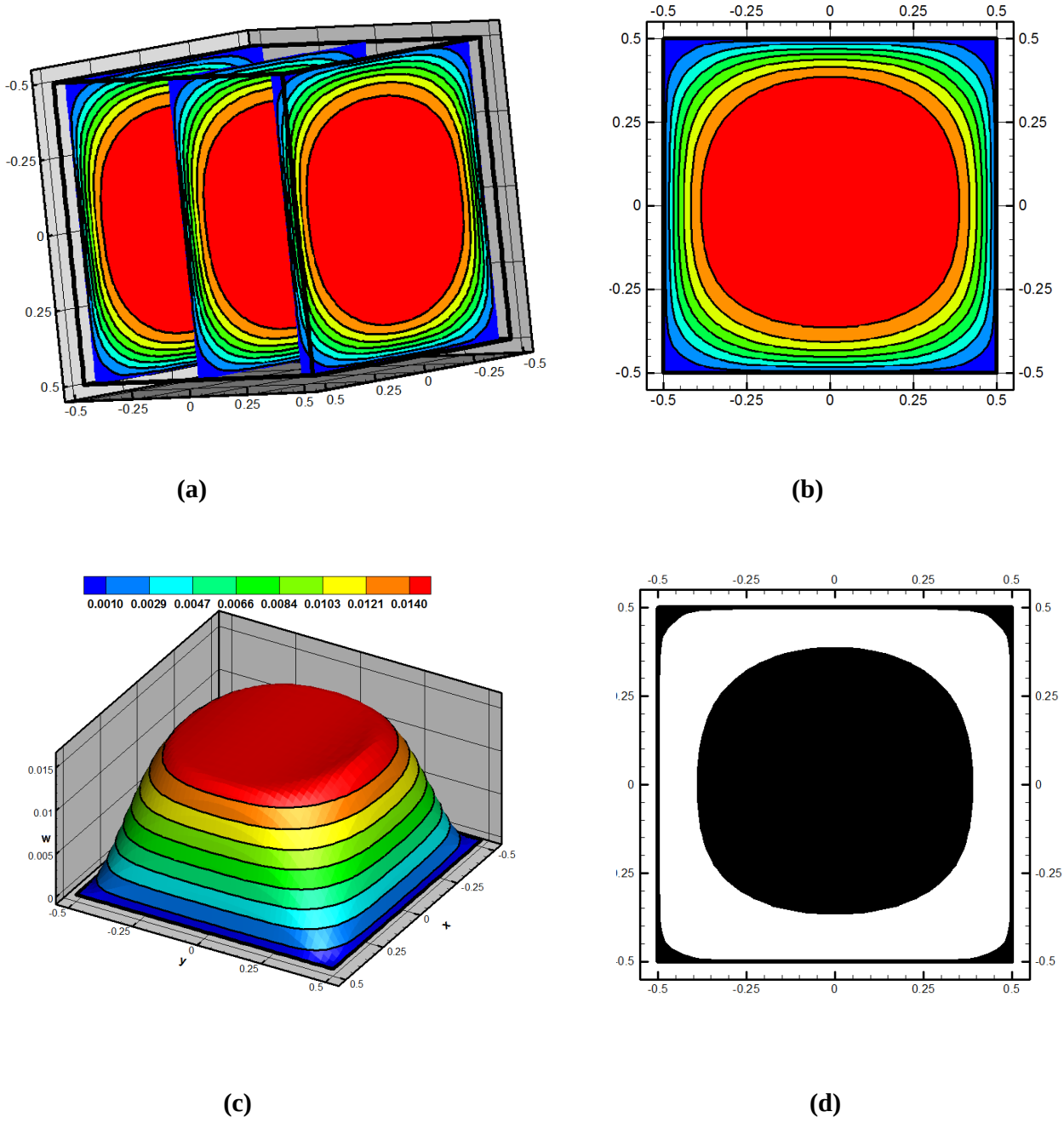

Fig. 4.15 (a) 3D contour of the square pipe flow (b) 2D contour of the square pipe flow (c) Velocity surface (d) The yielded/unyielded zones for $Od = 0.2$ and $D_H = 1$

Chapter 5

Non-isothermal flows of Bingham fluids: natural convection and mixed convection in a cavity

5.1 Natural convection of a Newtonian fluid using the mesoscopic method

The geometry of the chosen problem is shown in Fig.5.1. It consists of a two-dimensional cavity with a height L. The temperature of the left wall is maintained at a higher temperature T_H and the right wall is fixed at a lower temperature T_C. The horizontal walls are considered to be adiabatic and the cavity is filled with an incompressible Newtonian fluid. The density variation is approximated by the standard Boussinesq model. Finally, the viscous dissipation is neglected in the energy equation.

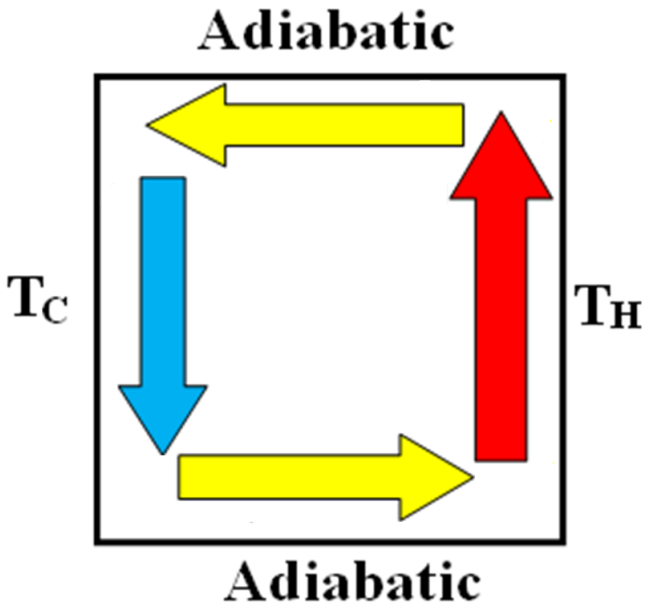

Fig. 5.1 Geometry of natural convection problem

Dimensional equations

Based on the above assumptions, denoting by $\mathbf{u} = u\mathbf{i} + v\mathbf{j}$ the velocity field, ρ the density, T the temperature field, and applying the Boussinesq approximation, Cauchy's equations for an incompressible fluid are (de Vahl Davis (1983); Quéré (1991); Quéré and de Roquefort (1985)):

$$\frac{\partial u}{\partial x} + \frac{\partial v}{\partial y} = 0 \ , \tag{5.1.1}$$

$$\rho\left(\frac{\partial u}{\partial t} + u\frac{\partial u}{\partial x} + v\frac{\partial u}{\partial y}\right) = -\frac{\partial p}{\partial x} + \left(\frac{\partial \tau_{xx}}{\partial x} + \frac{\partial \tau_{xy}}{\partial y}\right) \ , \tag{5.1.2}$$

$$\rho\left(\frac{\partial v}{\partial t} + u\frac{\partial v}{\partial x} + v\frac{\partial v}{\partial y}\right) = -\frac{\partial p}{\partial y} + \left(\frac{\partial \tau_{xy}}{\partial x} + \frac{\partial \tau_{yy}}{\partial y}\right) + \rho g\left[1 + \beta\left(T - T_C\right)\right], \tag{5.1.3}$$

$$\frac{\partial T}{\partial t}+u\frac{\partial T}{\partial x}+v\frac{\partial T}{\partial y}=\alpha\left(\frac{\partial^2 T}{\partial x^2}+\frac{\partial^2 T}{\partial y^2}\right)\ . \tag{5.1.4}$$

where α is the conductivity coefficient and β is the coefficient of thermal expansion. Now, let the pressure (p) be written as the sum $p=p_s+p_d$, where the static part p_s accounts for gravity alone, and p_d is the dynamic part. Thus,

$$-\frac{\partial p_s}{\partial y}=\rho g\cdot \tag{5.1.5}$$

The extra stresses are defined as follows:

$$\tau_{xx}=2\eta\left(\frac{\partial u}{\partial x}\right),\ \tau_{yy}=2\eta\left(\frac{\partial v}{\partial y}\right),\ \tau_{xy}=\eta\left(\frac{\partial u}{\partial y}+\frac{\partial v}{\partial x}\right)\ , \tag{5.1.6}$$

where η is the dynamic viscosity.

Dimensional boundary conditions

The flow domain is given by $\Omega=(0,L)\times(0,L)$, and the boundary $\Gamma=\partial\Omega$, with a subset $\Gamma_1=\{\mathbf{x}|\mathbf{x}=\{x,y\},0<x<L,y=0\,\text{or}\,L\}$. The boundary condition for the velocity is straightforward: $\mathbf{u}|_\Gamma=0$. The thermal boundary conditions are

$$T|_{x=0}=T_C,\ T|_{x=1}=T_H,\ \left.\frac{\partial T}{\partial y}\right|_{\Gamma_1}=0. \tag{5.1.7}$$

Non-dimensional equations

In order to proceed to the numerical solution, the following non-dimensional variables are introduced (Quéré (1991); Quéré and de Roquefort (1985)):.

$$\bar{x} = \frac{x}{L},\ \bar{y} = \frac{y}{L},\ \bar{u} = \frac{u}{(\alpha/L)\,Ra^{0.5}},\ \bar{v} = \frac{v}{(\alpha/L)\,Ra^{0.5}}\ , \tag{5.1.8a}$$

$$\bar{p} = \frac{p}{\rho(\alpha/L)^2 Ra}, \bar{t} = \frac{t}{(L^2/\alpha)\,Ra^{-0.5}},\quad \bar{T} = \frac{T - T_C}{T_H - T_C}\cdot \tag{5.1.8b}$$

By substitution of Eqs. (5.1.8) into Eqs.(5.1.1)-(5.1.4), and dropping the bar notation for convenience, the following system of non-dimensional equations is derived:

$$\frac{\partial u}{\partial x} + \frac{\partial v}{\partial y} = 0\ , \tag{5.1.9}$$

$$\left(\frac{\partial u}{\partial t} + u\frac{\partial u}{\partial x} + v\frac{\partial u}{\partial y}\right) = -\frac{\partial p}{\partial x} + \frac{\mathrm{Pr}}{\sqrt{Ra}}\left[\left(\frac{\partial^2 u}{\partial x^2}\right) + \left(\frac{\partial^2 u}{\partial y^2}\right)\right]\ , \tag{5.1.10}$$

$$\left(\frac{\partial v}{\partial t} + u\frac{\partial v}{\partial x} + v\frac{\partial v}{\partial y}\right) = -\frac{\partial p}{\partial y} + \frac{\mathrm{Pr}}{\sqrt{Ra}}\left[\left(\frac{\partial^2 v}{\partial x^2}\right) + \left(\frac{\partial^2 v}{\partial y^2}\right)\right] + \mathrm{Pr}\,T\ , \tag{5.1.11}$$

$$\frac{\partial T}{\partial t} + u\frac{\partial T}{\partial x} + v\frac{\partial T}{\partial y} = \frac{1}{\sqrt{Ra}}\left(\frac{\partial^2 T}{\partial x^2} + \frac{\partial^2 T}{\partial y^2}\right)\ . \tag{5.1.12}$$

The non-dimensional parameters for the problem under consideration are the Rayleigh number

$$Ra = \frac{\beta g L^3 (T_H - T_C)}{\nu \alpha} \ , \tag{5.1.13}$$

and the Prandtl number

$$\mathrm{Pr} = \frac{\nu}{\alpha} \ . \tag{5.1.14}$$

Non-dimensional boundary conditions

The flow domain is given by $\Omega = (0,1) \times (0,1)$, and the boundary $\Gamma = \partial\Omega$, with a subset $\Gamma_1 = \{\mathbf{x} | \mathbf{x} = \{x,y\}, 0 < x < 1, y = 0 \,\mathrm{or}\, 1\}$. The boundary condition for the velocity is straightforward: $\mathbf{u}|_\Gamma = 0$. The thermal boundary conditions are

$$T|_{x=0} = 0, \ T|_{x=1} = 1, \ \left.\frac{\partial T}{\partial y}\right|_{\Gamma_1} = 0. \tag{5.1.15}$$

TFDDFM

The mass and momentum equations in the absence of the buoyancy force term (Eqs. 5.1.1-5.1.2) are solved by applying Eqs. (3.3.4)-(3.3.13). Moreover, the energy equation (Eq.5.1.3) can be solved by using Eqs. (3.3.39)-(3.3.46).

The buoyancy force term effect as a body force in the momentum equation has been studied using the Eqs.(3.3.29)-(3.3.32) and the following equations are obtained.

$$F_\alpha = 0 \quad \alpha = 0,2,4,6,8 \ , \tag{5.1.16a}$$

$$F_\alpha = \boldsymbol{\xi}_\alpha . M \quad \alpha = 1,3,5,7 \ , \tag{5.1.16b}$$

$$M = \frac{\mathrm{Pr}\,T}{2\sigma^2}\,\mathbf{j}\cdot \tag{5.1.16c}$$

The corresponding polynomial of the equilibrium distribution function for the energy equation using the Eqs. (3.3.39)-(3.3.52) can be written as follows:

$$g_\alpha^{\mathrm{eq}} = D_\alpha + \boldsymbol{\xi}_\alpha \cdot \mathbf{E}_\alpha \ , \tag{5.1.17a}$$

$$D_0 = T \quad D_1 = D_2 = 0 \ , \tag{5.1.17b}$$

$$\mathbf{E}_1 = \frac{1}{2\sigma^2}\left(T\mathbf{u} - \frac{1}{\sqrt{\mathrm{Ra}}}\nabla T\right), \quad \mathbf{E}_2 = \mathbf{0}\cdot \tag{5.1.17c}$$

Results and validation

The Thermal Finite Difference Discrete Flux Method (TFDDFM) has been employed to simulate the flow under study and investigated at different Rayleigh numbers (Ra = 10^3, 10^4, and 10^5) and Prandtl numbers (Pr = 0.71, 5 and 10). To check the accuracy of the results, the present code is validated with published studies of Fu et al. (2012) where the average Nusselt number on the hot wall is compared at Pr = 0.71. The results are exhibited in Table.5.1 and show a good agreement between the compared studies. Since the Nusselt number (Nu) is one of the most important dimensionless parameters in describing the convective heat transport, the local and the average Nusselt numbers at the hot wall with the utilization of the dimensionless parameters are calculated through

$$\mathrm{Nu} = -\frac{\partial T}{\partial x}, \quad x = 0, \tag{5.1.18}$$

$$\mathrm{Nu}_{\mathrm{avg}} = \int_0^1 \mathrm{Nu}\, dy. \tag{5.1.19}$$

In addition, streamlines and isothermal contours as well as the velocities and temperatures in the middle of the cavity have been drawn to demonstrate the effects of the alterations of Prandtl and Rayleigh numbers.

Fig.5.2 shows the streamlines and isotherms of different Rayleigh numbers at Prandtl number of Pr = 5. As the Rayleigh number increases, the shape of the isotherms between the cold and hot walls change significantly and they become progressively curved. Moreover, the gradient of temperature on the hot wall augments with the rise of the Rayleigh number. In fact, the thermal boundary layer thickness on the side walls decreases with increasing Rayleigh number. The streamlines exhibit that the convection process has been enhanced by the growth of Rayleigh numbers as the core of the streamline changes from the circular shape to elliptical one gradually and the streamlines move into the cavity.

Fig.5.3 shows the vertical velocity and temperature components along the horizontal mid-plane of the cavity as the local Nusselt number changes. Different Rayleigh numbers are used when Pr = 5. At Ra = 10^3, the distribution of the temperature is nearly linear and the vertical velocity component is essentially negligible due to a very weak flow as the effects of buoyancy forces are dominated by viscous effects. Under this circumstance, the heat transfer takes place entirely by conduction across the enclosure, although the vertical velocity magnitude does indeed augment with augmentation of Rayleigh number. The distribution of the temperature becomes increasingly non-linear with the strengthening of convective transport for higher values of Rayleigh numbers. The local Nusselt number on the hot wall for Ra = 10^3 is roughly equal to one which demonstrates that the heat transfer takes place with the pure conduction process. The effects of buoyancy force strengthen in comparison to the viscous effects with increasing Rayleigh numbers. Therefore, as Rayleigh number rises,

Table 5.1 Comparison of the average Nusselt number between the present result and Fu et al. (2012) for Pr = 0.71·

Ra	10^3	10^4	10^5	10^6
Present	1.116	2.241	4.520	8.901
Fu et al. (2012)	1.117	2.246	4.518	8.906

the magnitude of the local Nusselt number is enhanced notably.

Fig.5.4 exhibits the isotherms and streamlines for various Prandtl numbers at Ra = 10^5. It illustrates that the gradient of the isotherms on the hot wall is enhanced as the Prandtl number increases. This trend has been confirmed by the streamlines in the core which demonstrates that the convection process augments with the rise of the Prandtl number.

The influence of Prandtl numbers can be observed on the vertical velocity in the middle of the cavity and the local Nusselt number on the hot wall at Fig.5.5. It is evident that an increase in the Prandtl number enhances the local Nusselt number significantly in the first half of the hot wall. However, the rise of the Prandtl number is nearly ineffective on the second part of the hot wall. In addition, the increase in the Prandtl number from Pr = 5 to 10 alters the local Nusselt number marginally. In other words, the enhancement of the Prandtl number from Pr = 5 to 10 does not influence heat transfer considerably. The vertical velocity distributions in the middle of the cavity indicate that the growth of Prandtl number raises the vertical velocity in the cavity although the mentioned trend is weakened from Pr = 5 to 10.

Table.5.2 reveals the average Nusselt number on the hot wall for different Rayleigh and Prandtl numbers. It demonstrates that the average Nusselt number rises as the Prandtl number increases while the augmentation is marginal from Pr = 5 to 10.

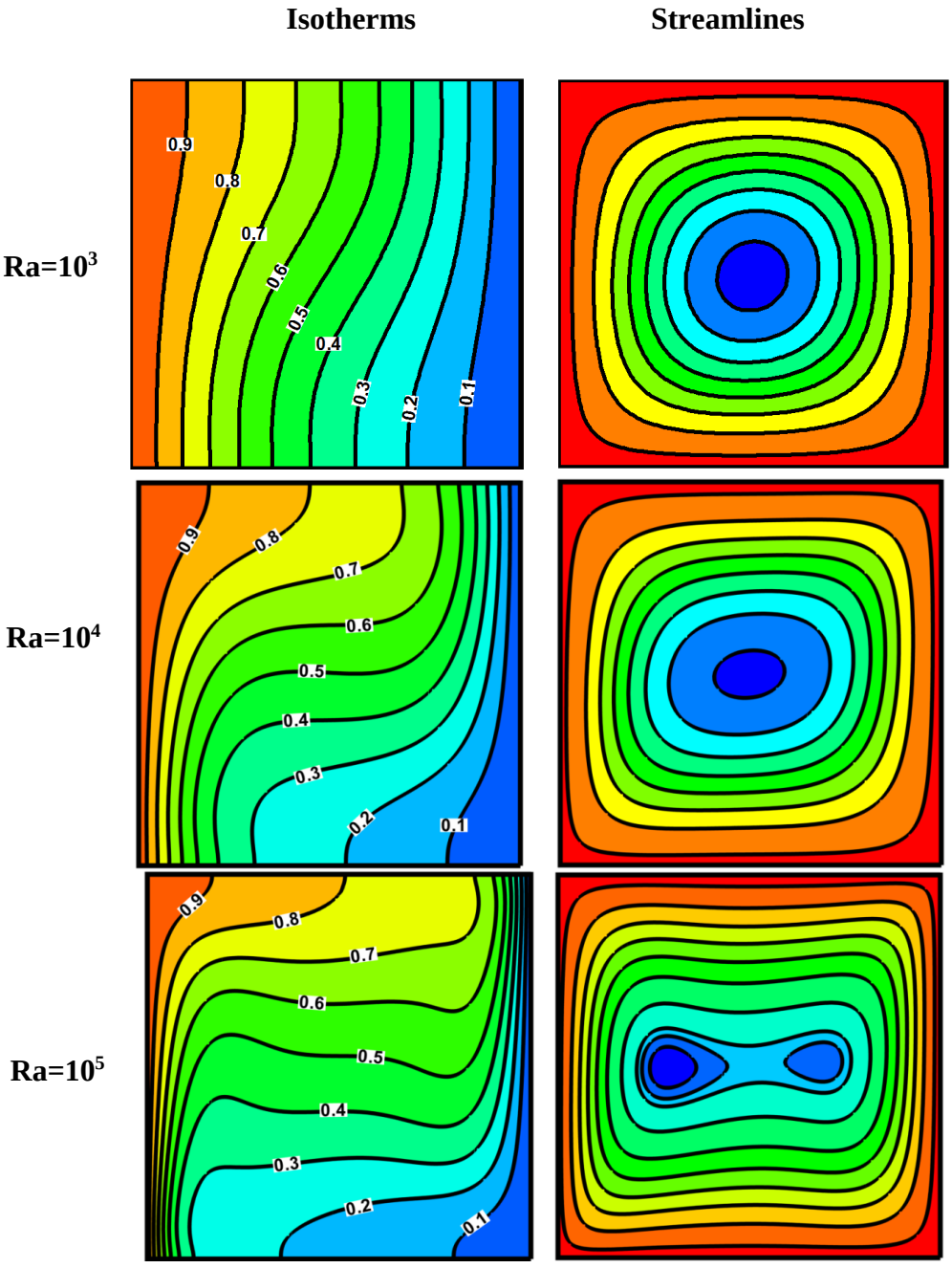

Fig. 5.2 Comparison of streamlines and isotherms for different Rayleigh numbers at Pr = 5·

Table 5.2 Comparison of the average Nusselt numbers for different Prandtl numbers·

	Pr=0.71	Pr=5	Pr=10
Ra=10^3	1.116	1.130	1.131
Ra=10^4	2.241	2.295	2.298
Ra=10^5	4.520	4.926	4.938

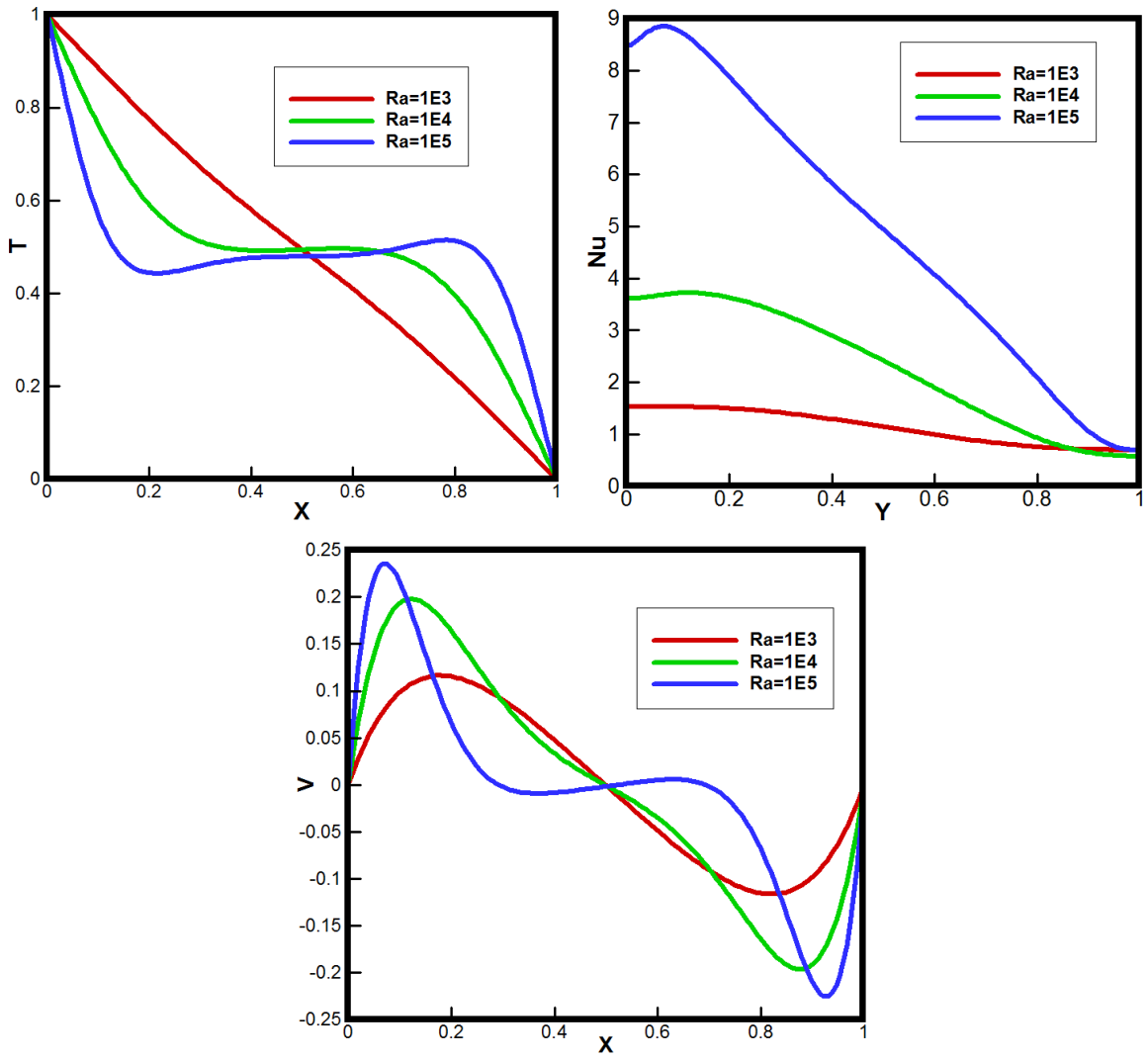

Fig. 5.3 Comparison of velocities and temperatures in the middle of the cavity and the local Nusselt number on the hot wall for different Rayleigh numbers·

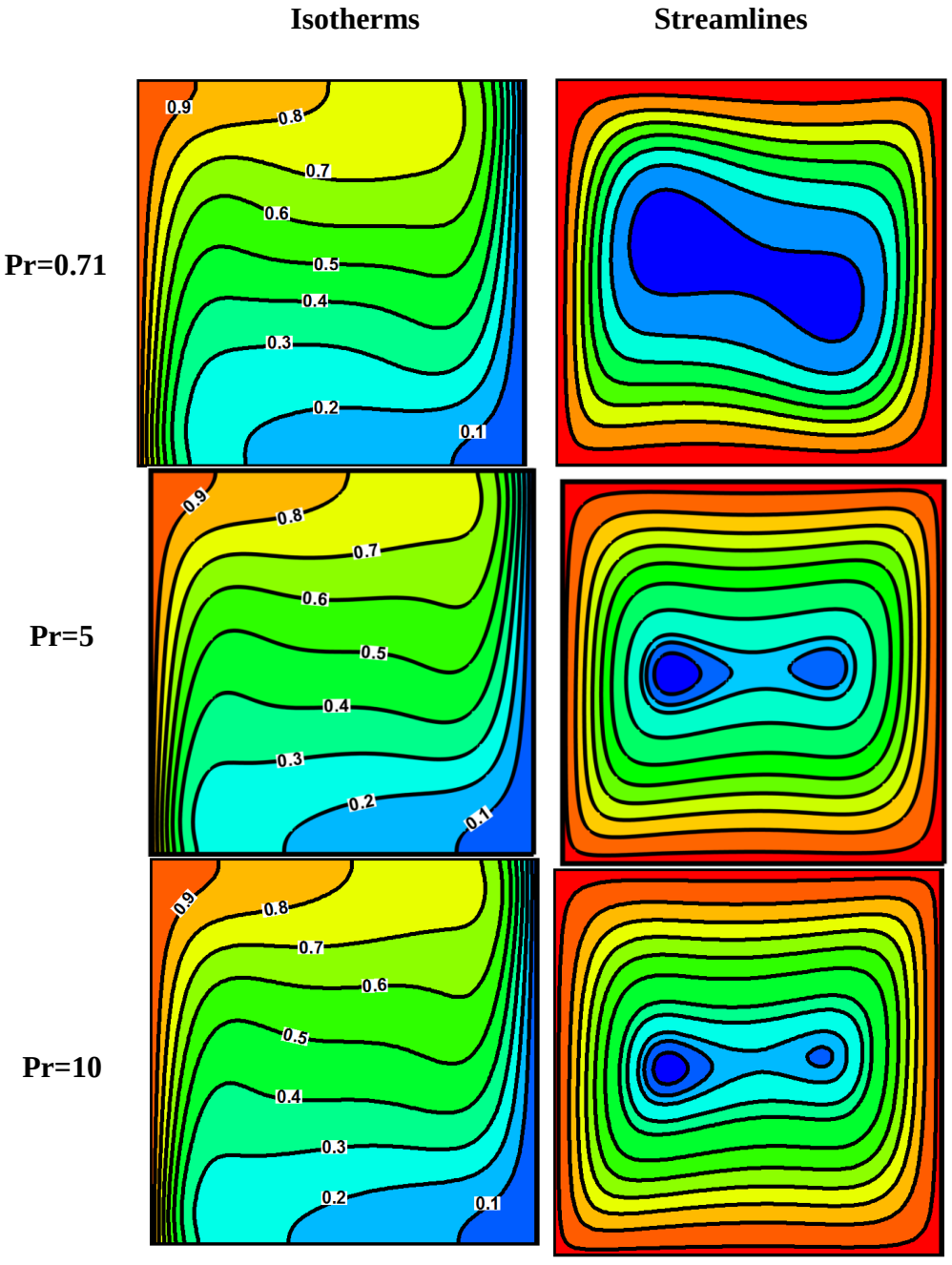

Fig. 5.4 Comparison of streamlines and isotherms for different Prandtl numbers at Ra = 10^5.

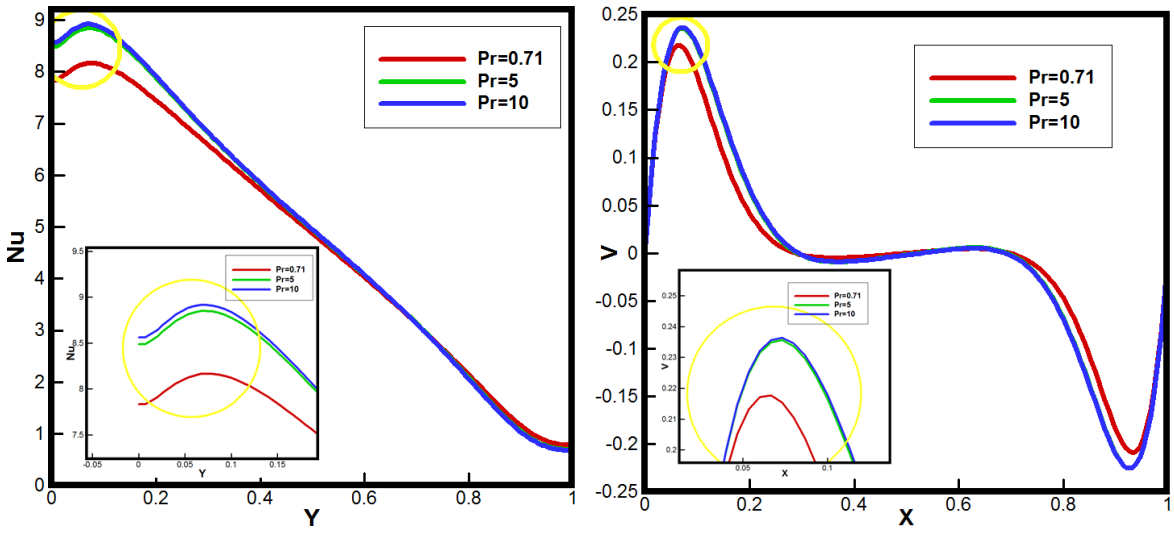

Fig. 5.5 Comparison of velocities in the middle of the cavity and the local Nusselt number on the hot wall for different Prandtl numbers·

5.2 Natural convection of a Bingham fluid using the Operator Splitting Method

The natural convection of a Bingham fluid is supposed to take place in an upright square cavity with an edge length of L (Fig. 5.6). The horizontal walls are insulated, and the vertical left and right walls are at temperatures T_H and $T_C < T_H$, respectively. The flow velocity is zero on all the walls. The gravity vector $\mathbf{g} = -g\mathbf{e}_2$ is directed in the negative y-coordinate direction, with $\mathbf{e}_2$ the unit vector in the y direction. Following the conventional Boussinesq approximation (Li and Glowinski (1996)), we consider small temperature variations only, i.e., the relative change in temperature $\delta T/T \ll 1$. The density ρ, thermal conductivity k, the heat capacity c_p and viscosity η are set to be constants here. For completeness, let us mention that in the extended Boussinesq or more general models, k and η are defined as functions of T, e.g., obeying the Sutherland law (Chenoweth and Paolucci (1985, 1986)), which leads to an enlarged range of validity when η has a strong temperature dependence (Gartling and Hickox (1985); Gray and Giorgini (1976); Li and Glowinski (1996)).

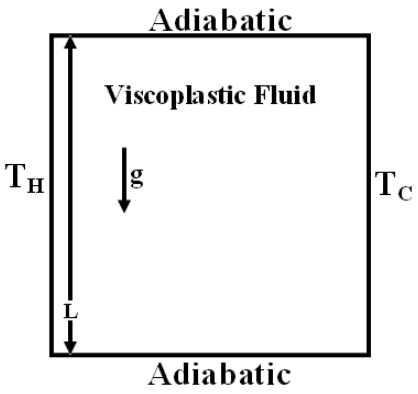

Fig. 5.6 The geometry of natural convection of Bingham fluid

5.2.1 Constitutive model

The Bingham model is utilised here and therefore the constitutive relation can be described as follows:

$$\mathbf{S} = \eta \mathbf{A_1}(\mathbf{v}) + \sqrt{2}\tau_y \mathbf{\Lambda}\,, \tag{5.2.1}$$

where

$$\mathbf{\Lambda} : \mathbf{\Lambda} \leq 1, \quad \mathbf{1} : \mathbf{\Lambda} = 0, \tag{5.2.2}$$

$$\mathbf{\Lambda} : \mathbf{A_1}(\mathbf{v}) \leq [\mathbf{A_1}(\mathbf{v}) : \mathbf{A_1}(\mathbf{v})]^{1/2}, \tag{5.2.3}$$

$$\mathbf{\Lambda} : \mathbf{A_1}(\mathbf{u}) = [\mathbf{A_1}(\mathbf{u}) : \mathbf{A_1}(\mathbf{u})]^{1/2}, \tag{5.2.4}$$

where $\mathbf{u}$ is the solution vector, and $\mathbf{v}$ is any trial velocity field.

It is important to note that the tensor $\mathbf{\Lambda}$ has zero trace. Secondly, the real advantage of the tensor $\mathbf{\Lambda}$ becomes obvious when $\mathbf{\Lambda} : \mathbf{\Lambda} < 1$. In this case, we see through Eq. (5.2.4) and

the Cauchy-Schwarz inequality that

$$[\mathbf{A_1}(\mathbf{u}) : \mathbf{A_1}(\mathbf{u})]^{1/2} = \boldsymbol{\Lambda} : \mathbf{A_1}(\mathbf{u}) \leq [\boldsymbol{\Lambda} : \boldsymbol{\Lambda}]^{1/2}[\mathbf{A_1}(\mathbf{u}) : \mathbf{A_1}(\mathbf{u})]^{1/2}$$
$$< [\mathbf{A_1}(\mathbf{u}) : \mathbf{A_1}(\mathbf{u})]^{1/2}. \tag{5.2.5}$$

The only solution to this inequality is that $\mathbf{A_1}(\mathbf{u}) = \mathbf{0}$. That is, wherever $\boldsymbol{\Lambda} : \boldsymbol{\Lambda} < 1$, the motion must be rigid. This shows that the fluid domain is now decomposed into two sets: one where $\boldsymbol{\Lambda} : \boldsymbol{\Lambda} < 1$ and where $\boldsymbol{\Lambda} : \boldsymbol{\Lambda} = 1$. In the latter case, the fluid has yielded. That is, by finding the tensor $\boldsymbol{\Lambda}$ throughout the flow domain, one overcomes the difficulty associated with the Bingham model.

The tensor $\boldsymbol{\Lambda}$ can be obtained from a simple projection operation as follows (Huilgol and You (2009)):

$$\boldsymbol{\Lambda} = P_{\mathscr{M}}\left(\boldsymbol{\Lambda} + r\tau_y \mathbf{A_1}(\mathbf{v})\right) \quad \forall r > 0, \tag{5.2.6}$$

where $\mathscr{M} = \left\{\boldsymbol{\mu} | \boldsymbol{\mu} = (\mu_{ij})_{1\leq i,j\leq 2} \in (L^2(\Omega))^4, \|\boldsymbol{\mu}\| \leq 1 \text{ a.e. on } \Omega\right\}$ and

$$P_{\mathscr{M}} : (L^2(\Omega))^4 \to \mathscr{M} \tag{5.2.7}$$

is the projection operator defined so that $P_{\mathscr{M}}(\boldsymbol{\mu}) = \boldsymbol{\mu}$, if $\|\boldsymbol{\mu}\| \leq 1$, and $P_{\mathscr{M}}(\boldsymbol{\mu}) = \boldsymbol{\mu}/\|\boldsymbol{\mu}\|$ otherwise. Note that in the context of Eq. (5.2.6), the tensor $\boldsymbol{\mu} = \boldsymbol{\Lambda} + r\tau_y \mathbf{A_1}(\mathbf{v})$ and it is symmetric. Further, the tensor $\boldsymbol{\mu}$ must be dimensionless for $\boldsymbol{\Lambda}$ is also dimensionless. In the Appendix A, this property of $\boldsymbol{\mu}$ is shown to lead to its non-dimensional form.

5.2.2 Dimensional governing equations

The governing equations for the buoyancy driven natural convection problem have the following form:

- Continuity equation

$$\nabla \cdot \mathbf{u} = 0. \tag{5.2.8}$$

- Momentum equation

$$\rho \left[\frac{\partial \mathbf{u}}{\partial t} + (\mathbf{u} \cdot \nabla)\mathbf{u} \right] - \nabla \cdot \mathbf{S} + \nabla p = \rho \mathbf{b}, \tag{5.2.9}$$

where the body force $\mathbf{b}$ is the sum of that due to gravity and the buoyancy effects. That is,

$$\mathbf{b} = [1 + \beta(T_r - T)]\mathbf{g}, \tag{5.2.10}$$

where $\mathbf{g} = -g\mathbf{e}_2$. Now, let p be written as the sum $p = p_s + p_d$, where the static part p_s accounts for gravity alone, and p_d is the dynamic part. Thus,

$$-\nabla p_s - \rho \mathbf{g} = \mathbf{0}, \tag{5.2.11}$$

so that $p_s = -\rho g y$. Hence, the momentum equation incorporates the dynamic part only, and is of the form

$$\rho \left[\frac{\partial \mathbf{u}}{\partial t} + (\mathbf{u} \cdot \nabla)\mathbf{u} \right] - \nabla \cdot \mathbf{S} + \nabla p_d = \rho \beta (T_r - T)\mathbf{g} \cdot \tag{5.2.12}$$

- Energy equation

$$\rho c_p \left[\frac{\partial T}{\partial t} + (\mathbf{u} \cdot \nabla)T \right] - k\nabla^2 T = 0, \tag{5.2.13}$$

where ∇^2 is the two dimensional Laplacian.

- Constitutive equation

$$\mathbf{S} = \eta \mathbf{A_1}(\mathbf{u}) + \sqrt{2}\tau_y \mathbf{\Lambda}. \tag{5.2.14}$$

In the above equations, $\mathbf{u}$, p and T stand for the unknown velocity, pressure and temperature, respectively. T_r is the reference temperature defined as $T_r = (T_H + T_C)/2$; β is the coefficient of thermal expansion. The right hand side of Eq. (5.2.12) accounts for the buoyancy effect under the Boussinesq approximation, which allows only small temperature deviations from the reference temperature.

5.2.3 Non-dimensionalisation

Letting L be the length scale, the average temperature $T_r = (T_H + T_C)/2$ the temperature scale, and $\delta T = T_H - T_C$, we define the buoyancy velocity scale $U = \sqrt{gL\beta\delta T}$, and the three dimensionless numbers as follows:

$$\mathrm{Bn} = \frac{\sqrt{2}\tau_y L}{\eta U}, \quad \mathrm{Ra} = \frac{g\beta\rho L^3 \delta T}{\alpha\eta}, \quad \mathrm{Pr} = \frac{\eta c_p}{k}, \tag{5.2.15}$$

where $\alpha = k/\rho c_p$ is the thermal diffusivity. The numbers Bn, Ra and Pr are known as the Bingham, Rayleigh and Prandtl numbers respectively. Next, set

$$\mathbf{u} = U\mathbf{u}^*,\ \mathbf{x} = L\mathbf{x}^*,\ t = \frac{L}{U}t^*,\ p_d = \frac{\eta U}{L}p^*,\ T = T_r + \delta T \cdot T^*. \tag{5.2.16}$$

The following non-dimensional governing equations are obtained by applying Eq. (5.2.16) to the dimensional equations (5.2.8)-(5.2.14) and dropping the asterisks:

$$\nabla \cdot \mathbf{u} = 0, \tag{5.2.17}$$

$$\sqrt{\frac{\mathrm{Ra}}{\mathrm{Pr}}}\left[\frac{\partial \mathbf{u}}{\partial t} + (\mathbf{u}\cdot\nabla)\mathbf{u}\right] - \nabla\cdot\mathbf{A_1}(\mathbf{u}) + \nabla p - \mathrm{Bn}\nabla\cdot\mathbf{\Lambda} = \sqrt{\frac{\mathrm{Ra}}{\mathrm{Pr}}}T\mathbf{e}_2, \tag{5.2.18}$$

$$\frac{\partial T}{\partial t} + (\mathbf{u}\cdot\nabla)T - \frac{1}{\sqrt{\mathrm{RaPr}}}\nabla^2 T = 0. \tag{5.2.19}$$

Now, let the flow domain $\Omega = (0,1) \times (0,1)$, and the boundary $\Gamma = \partial\Omega$, with a subset $\Gamma_1 = \{\mathbf{x}|\mathbf{x} = \{x,y\}, 0 < x < 1, y = 0 \text{ or } 1\}$. The boundary condition for the velocity is straightforward: $\mathbf{u}|_\Gamma = 0$. The thermal boundary conditions are

$$T|_{x=0} = \frac{1}{2},\ T|_{x=1} = -\frac{1}{2},\ \left.\frac{\partial T}{\partial y}\right|_{\Gamma_1} = 0. \tag{5.2.20}$$

Finally, it is worth noting that if the Bingham number $\mathrm{Bn} = 0$, the fluid is a Newtonian fluid. Thus, there is no need to find the viscoplastic constraint tensor $\mathbf{\Lambda}$. It can be put to zero everywhere in the numerical scheme to derive the results for the Newtonian fluid.

5.2.4 Numerical Procedure

In this section, we shall explain the numerical scheme we have used to solve the problem (5.2.17)-(5.2.20).

Time discretisation by operator-splitting method

Based on the operator-splitting method discussed in Huilgol and You (2009), Li and Glowinski (1996), a new scheme has been designed to examine the non-isothermal viscoplastic problem, and the algorithm has been written in variational form in order to facilitate the finite element implementation.

Let Δt be the time step and f^n denote the value of function $f(t)$ at time $t = t^n$. As usual, $t^{n+\gamma} = (n+\gamma)\Delta t$. Assuming that $\mathbf{u}^n, p^n, T^n, \mathbf{\Lambda}^n$ are known, the numerical scheme works in an iterative way:

Step 1. The temperature problem:

Solve the energy equation together with boundary conditions for T^{n+1}:

$$\begin{aligned}\frac{1}{\Delta t}\int_\Omega (T^{n+1}-T^n)\varphi\, da &+ \int_\Omega (\mathbf{u}^n\cdot\nabla)T^{n+1}\varphi\, da \\ +\chi\int_\Omega \nabla T^{n+1}\cdot\nabla\varphi\, da &= 0, \quad \forall\varphi\in H_0^1(\Omega).\end{aligned} \tag{5.2.21}$$

Step 2. The generalised Stokes problem:

Find $\left\{\mathbf{u}^{n+1/3}, p^{n+1}\right\}\in (H_0^1)^2\times L^2$ such that

$$\begin{aligned}&\frac{\alpha}{\Delta t}\int_\Omega (\mathbf{u}^{n+1/3}-\mathbf{u}^n)\cdot\mathbf{v}\, da+\frac{1}{3}\int_\Omega \nabla\mathbf{u}^{n+1/3}:\nabla\mathbf{v}\, da-\int_\Omega p^{n+1}\nabla\cdot\mathbf{v}\, da\\ &=\alpha\int_\Omega \frac{T^{n+1}+T^n}{2}\mathbf{e}_2\cdot\mathbf{v}\, da, \quad \forall\mathbf{v}\in(H_0^1(\Omega))^2,\end{aligned} \tag{5.2.22}$$

$$\int_\Omega \nabla\cdot\mathbf{u}^{n+1/3}q=0\, da, \quad \forall q\in L^2(\Omega). \tag{5.2.23}$$

Step 3. The convected derivative problem:

Solve for $\mathbf{u}^{n+2/3}\in(H_0^1)^2$:

$$\begin{aligned}&\frac{\alpha}{\Delta t}\int_\Omega (\mathbf{u}^{n+2/3}-\mathbf{u}^{n+1/3})\cdot\mathbf{v}\, da+\alpha\int_\Omega (\mathbf{u}^{n+1/3}\cdot\nabla)\mathbf{u}^{n+2/3}\cdot\mathbf{v}\, da\\ &+\frac{1}{3}\int_\Omega \nabla\mathbf{u}^{n+2/3}:\nabla\mathbf{v}\, da=0, \quad \forall\mathbf{v}\in(H_0^1(\Omega))^2.\end{aligned} \tag{5.2.24}$$

Note that in Eq. (5.2.24), $(\mathbf{u}^{n+1/3}\cdot\nabla)\mathbf{u}^{n+2/3}$ is the linearised form of the original nonlinear term $(\mathbf{u}^{n+2/3}\cdot\nabla)\mathbf{u}^{n+2/3}$. By this simplification, we can take the advantage of saving computation cost without losing the accuracy.

Step 4. The viscoplasticity constraint tensor problem:

Given $\mathbf{u}^{n+2/3}$, solve for $\left\{\mathbf{u}^{n+1}, \mathbf{\Lambda}^{n+1}\right\} \in (H_0^1)^2 \times \mathscr{M}$:

$$\begin{aligned}&\frac{\alpha}{\Delta t}\int_\Omega (\mathbf{u}^{n+1}-\mathbf{u}^{n+2/3})\cdot\mathbf{v}\,da + \frac{1}{3}\int_\Omega \nabla\mathbf{u}^{n+1}:\nabla\mathbf{v}\,da \\ &+\mathrm{Bn}\int_\Omega \mathbf{\Lambda}^{n+1}:\nabla\mathbf{v}\,da = 0, \quad \forall\mathbf{v}\in(H_0^1(\Omega))^2,\end{aligned} \tag{5.2.25}$$

$$\mathbf{\Lambda}^{n+1} = P_{\mathscr{M}}\left(\mathbf{\Lambda}^n + \mathrm{Pr}\cdot\mathrm{Bn}\mathbf{A_1}(\mathbf{u}^{n+2/3})\right). \tag{5.2.26}$$

As mentioned after Eq. (5.2.7), the new value of $\mathbf{\Lambda}^{n+1}$ depends on the magnitude of $\mathbf{\Lambda}^n + \mathrm{Pr}\cdot\mathrm{Bn}\mathbf{A_1}(\mathbf{u}^{n+2/3})$. That is, we use $P_{\mathscr{M}}(\boldsymbol{\mu}) = \boldsymbol{\mu}$, if $\|\boldsymbol{\mu}\| \le 1$, and $P_{\mathscr{M}}(\boldsymbol{\mu}) = \boldsymbol{\mu}/\|\boldsymbol{\mu}\|$ otherwise, to find the new value of $\mathbf{\Lambda}^{n+1}$.

Again, recall from the comments made that if the Bingham number $\mathrm{Bn} = 0$, then one can put $\mathbf{\Lambda}^n = \mathbf{0}$ in Eq. (5.2.26). Then, it follows that $\mathbf{\Lambda}^{n+1} = \mathbf{0}$ automatically and in Eq. (5.2.25), we can omit the integral involving this tensor. Thus, Eq. (5.2.25) becomes a sub-problem for finding $\mathbf{u}^{n+1}$ only.

Finally, one should note that we have taken $\alpha = \sqrt{\mathrm{Ra}/\mathrm{Pr}}$ in Eqs. (5.2.21), (5.2.24) and (5.2.25), and $\chi = 1/\sqrt{\mathrm{Ra}\cdot\mathrm{Pr}}$ in Eq. (5.2.21) for convenience.

It is clear that the original complicated problem has been split into four subproblems in each time step and solved by an iterative algorithm. In Step 1, the updated temperature in the new time step T^{n+1} is calculated from the values of last time step T^n and $\mathbf{u}^n$. Then the pressure in the new time step p^{n+1} is updated and the intermediate velocity $\mathbf{u}^{n+1/3}$ is solved in Step 2. Step 3 gives the intermediate velocity $\mathbf{u}^{n+2/3}$ and finally the velocity in the new time step $\mathbf{u}^{n+1}$ together with Λ^{n+1} is updated in Step 4. The stopping criterion for the iteration is $\left\|\mathbf{u}^{n+1}-\mathbf{u}^n\right\|_{L^2} + \left\|T^{n+1}-T^n\right\|_{L^2} < \varepsilon$, in which ε is a convergence parameter.

Spatial discretisation by finite element method

For the spatial discretisation, we employ the finite element method using the P2–P1 element pair, the same as in Huilgol and You (2009). With $\mathscr{T}_h$ a standard finite element triangulation of Ω and h the maximum length of the edges of $\mathscr{T}_h$, we define the discrete spaces P_h for pressure, W_h for temperature and V_h for velocity approximations as

$$P_h = \left\{ q_h | q_h \in C^0\left(\overline{\Omega}\right), q_h|_T \in P_1, \forall T \in \mathscr{T}_h \right\}, \tag{5.2.27}$$

$$W_h = \left\{ w_h | w_h \in C^0\left(\overline{\Omega}\right), w_h|_T \in P_2, \forall T \in \mathscr{T}_h \right\}, \tag{5.2.28}$$

$$V_h = \left\{ \mathbf{v}_h | \mathbf{v}_h \in \left(C^0\left(\overline{\Omega}\right)\right)^2, \mathbf{v}_h|_T \in \left(P_2\right)^2, \forall T \in \mathscr{T}_h \right\}. \tag{5.2.29}$$

The corresponding boundary conditions can be imposed on the basic spaces W_h and V_h. Note that we have chosen the same finite element spaces for the temperature and the velocity components to achieve better performance.

5.2.5 Code validation and grid independence

This problem has been investigated at different Rayleigh numbers of $\mathrm{Ra} = 10^3 - 10^5$ and Prandtl numbers of $\mathrm{Pr} = 0.1 - 10$ as Bingham number is studied in different ranges for various Rayleigh numbers. The Operator Splitting Method based on FEM has been utilized to perform the numerical simulations. A uniform triangulation mesh has been applied to the problem and the maximum length of the edges is fixed at h = 0.01. Moreover, the time step is 0.001 and the convergence parameter is $\varepsilon = 10^{-6}$. To check the accuracy of the present results, the present code for Newtonian fluid has been validated with published studies on the natural convection in a cavity. The results are compared in Table 5.3 and they show a close

agreement between present and previous studies. Moreover, the results for the Bingham fluid on natural convection in an enclosure have been tested against the work of Turan et al. (2010, 2011) in Table 5.4. Although they utilized the regularised bi-viscosity model, the comparison shows that the average Nusselt number is nearly the same for low Bingham numbers as evident in Table 5.4. However, the differences between the present results and those of Turan et al. (2010, 2011) increase gradually as the Bingham number increases. In fact, the different methods result in the observed differences at high Bingham numbers.

Table 5.3 Comparison of the present study with the results of de Vahl Davis (1983) for different Rayleigh numbers at Pr = 0.71·

		Present study	de Vahl Davis (1983)
$Ra = 10^3$	Nu	1.118	1.118
	Nu_{max}	1.505	1.505
	U_{max}	3.644	3.649
	V_{max}	3.690	3.697
$Ra = 10^4$	Nu	2.243	2.243
	Nu_{max}	3.528	3.528
	U_{max}	16.170	16.178
	V_{max}	19.613	19.617
$Ra = 10^5$	Nu	4.519	4.519
	Nu_{max}	7.717	7.717
	U_{max}	34.725	34.730
	V_{max}	68.588	68.590

Table 5.4 Comparison of present study with the results of Turan et al. (2010) on the average Nusselt number at the hot wall for Pr = 1 and Rayleigh numbers of $Ra = 10^4$ and 10^5·

	Bn = 0	Bn = 0.5	Bn = 1	Bn = 1.5	Bn = 2	Bn = 2.5	Bn = 3
$Ra = 10^4$							
Turan et al. (2010)	2.23	2.00	1.70	1.43	1.21	1.10	1.00
Present study	2.23	1.91	1.65	1.49	1.34	1.21	1.1
$Ra = 10^5$							
Turan et al. (2010)	4.60		3.89		3.45		2.95
Present study	4.60		3.89		3.46		3.16

5.2.6 Results and Discussion

Rayleigh number effect

The Fig. 5.7 illustrates the isotherms and streamlines as the yielded and unyielded zones have been clarified evidently for different Rayleigh numbers at Bn = 3 and Pr = 0.1. At Ra = 10^3, the temperature contours are parallel to the wall which demonstrate that conduction dominates in the enclosure. As the Rayleigh number increases, the movements of the isotherms between the cold and hot walls change significantly and they become progressively curved. Moreover, the gradient of temperature on the hot wall augments with the rise of the Rayleigh number, for the thermal boundary layer thickness on the side walls decreases with increasing Rayleigh numbers. The streamlines exhibit that the convection process has been enhanced by the growth of Rayleigh numbers as the core of the streamline changes from the circular shape to elliptical one gradually and the streamlines traverse further into the cavity. The last column displays the yielded (White) and unyielded (Black) regions for the studied Rayleigh numbers at Bn = 3. It is clear that the proportion of the unyielded sections in the enclosure has increased with the fall in the Rayleigh numbers markedly. Therefore, for constant Bingham and Prandtl numbers, the increase in Rayleigh number causes the unyielded zones to decline.

The Fig. 5.8 indicates the vertical velocity and temperature along the horizontal mid-plane of the cavity as the local Nusselt number has been varied for different Rayleigh numbers at Bn = 3 and Pr = 0.1. At Ra = 10^3, the distribution of T is nearly linear and the vertical velocity component is essentially negligible due to a very weak flow as the effects of buoyancy forces are dominated by viscous effects. Under this circumstance, the heat transfer takes place entirely by conduction across the enclosure. The vertical velocity magnitude does indeed increase with augmentation of the Rayleigh number and the distribution of the temperature becomes increasingly non-linear with the strengthening of convective transport for higher

values of Rayleigh numbers. The local Nusselt number on the hot wall for Ra = 10^3 is roughly equal to one which demonstrates that the heat transfer occurs by conduction only. The effects of buoyancy force strengthen in comparison to the viscous effects with increasing Rayleigh numbers. Therefore, as the Rayleigh number rises, the magnitude of the local Nusselt number increases markedly.

Bingham number effect

The Bingham number influence on the isotherms, streamlines and the proportion of the unyielded regions has been depicted by Fig. 5.9 for Ra = 10^5 and Pr = 0.1. It shows that the curved shape of the isotherm declines with an increase in the Bingham number. This process causes the gradient of temperature on the hot wall to drop and therefore heat transfer decreases with the rise of the Bingham number. The streamlines prove the decrease in the convection process with the growth of the Bingham number as the inclined elliptical form of the core of the cavity alters to a circular shape. The pattern in the streamlines was metioned by Turan et al. (2010). Table 5.5 corroborates the mentioned effects of the Bingham numbers clearly for the maximum strength of the streamline decreases with the augmentation of the Bingham numbers. Moreover, the maximum vertical and horizontal velocities in the middle of the cavity have declined and the average Nusselt number decreases with the rise of the Bingham number. As a result, the convection process decreases with the enhancement of the Bingham number. The unyielded sections occupy larger regions in the cavity as the Bingham number increases. In fact, the rise of the Bingham number causes the yielded regions to disappear gradually. However, there is a critical Bingham number at which the flow would be fully unyielded. This value is named as the maximum Bingham number and is specified in Table 5.6 for different Prandtl and Rayleigh numbers. Furthermore, the relationship between

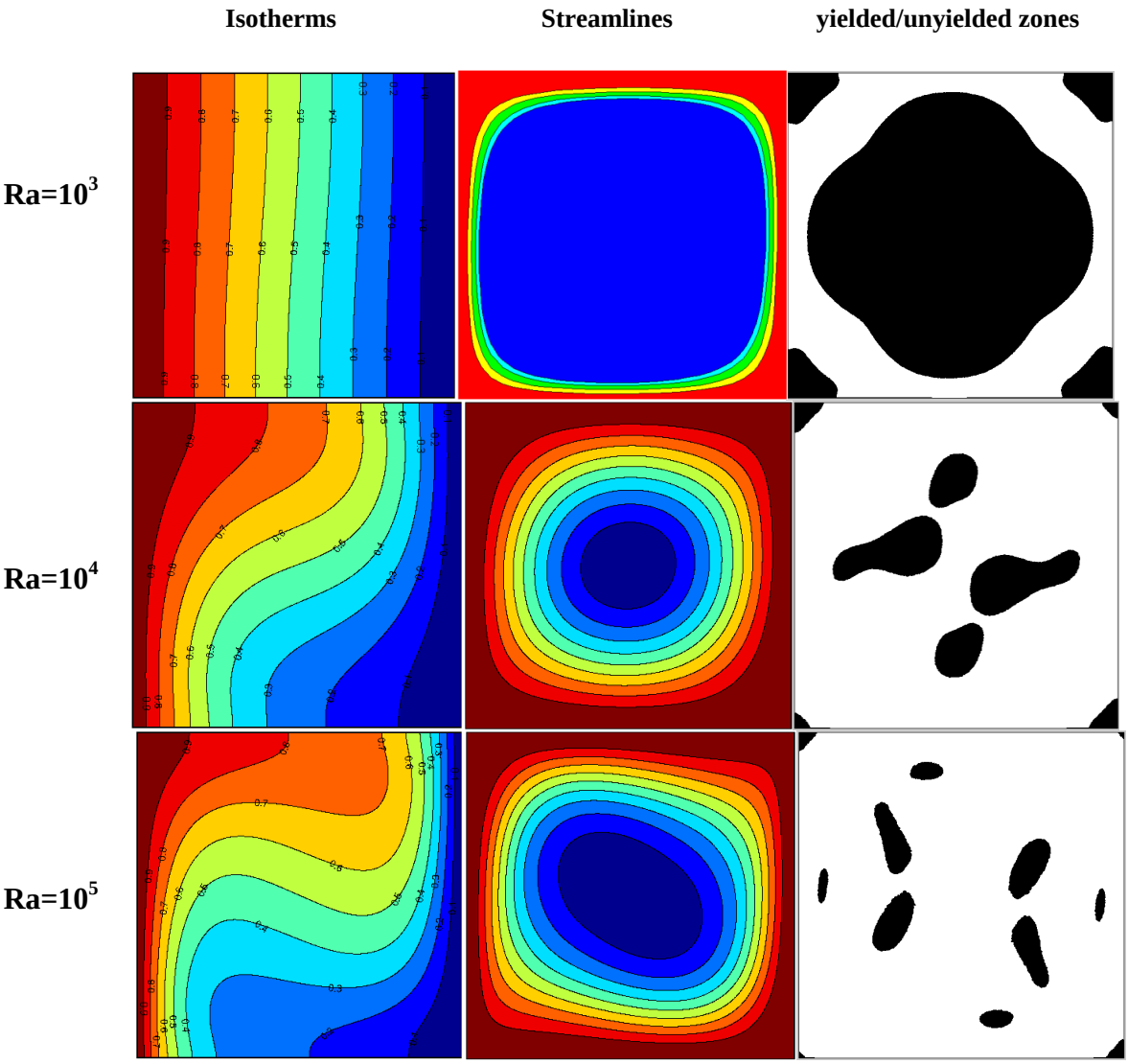

Fig. 5.7 Comparison of the streamlines, isotherms and yielded/unyielded zones for various Rayleigh numbers at Bn = 3 and Pr = 0.1 (Black: unyielded zone; white: yielded zone)·

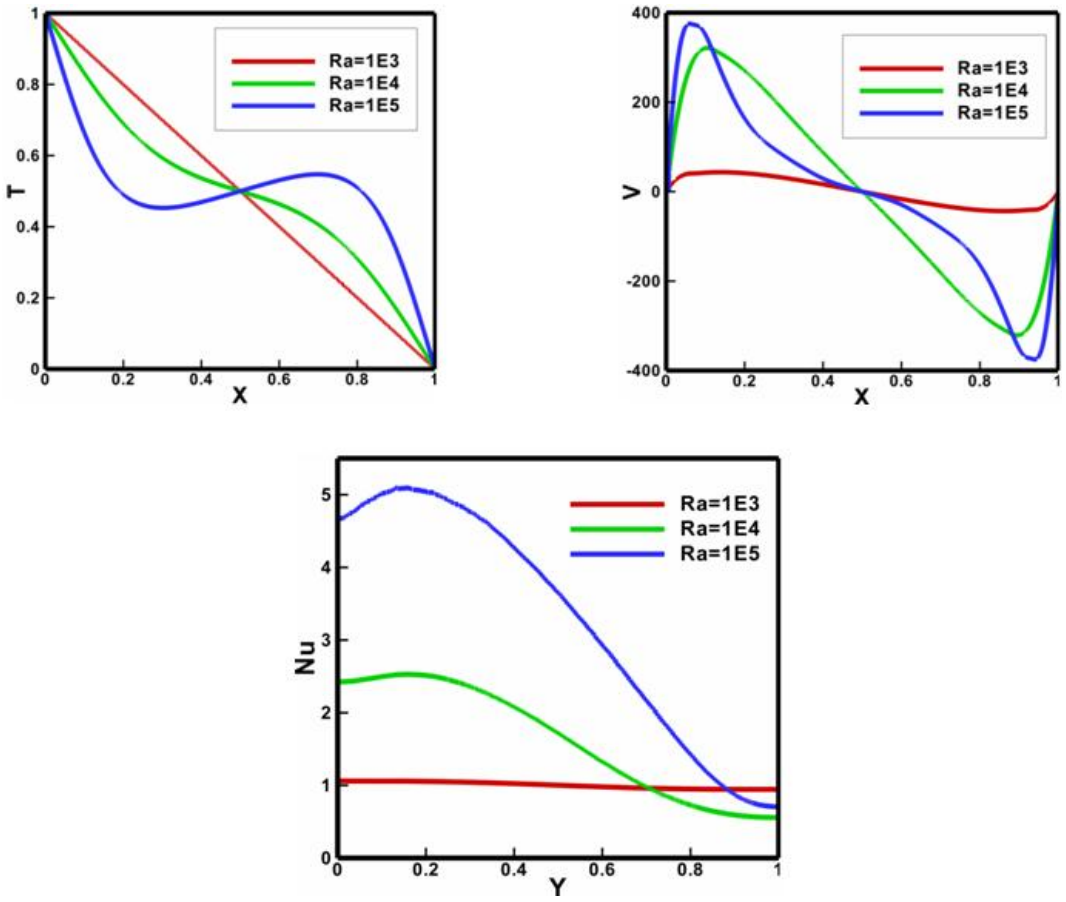

Fig. 5.8 Vertical velocity and temperatures in the middle of the cavity and local Nusselt number on the hot wall for different Rayleigh numbers at Bn = 3 and Pr = 0.1 ·

the maximum Bingham, Rayleigh and Prandtl numbers appears to be given by:

$$Bn_{max} \simeq Ra^{0.5} Pr^{-0.5} , \tag{5.2.30}$$

similar to that found by Karimfazli et al. (2015).

The Fig. 5.10 depicts the vertical velocity and temperature along the horizontal mid-plane of the cavity as the local Nusselt number changes for different Bingham numbers at Ra = 10^5 and Pr = 0.1. The temperature profile becomes linear when the Bingham number increases which shows the effects of the Bingham number leading to a drop of the convection process. This pattern is followed by the vertical velocity in the middle of the cavity where its magnitude drops significantly with the increase in the Bingham number. The local Nusselt number decreases with the enhancement of the Bingham number. In fact, for high values of the Bingham number, the viscous force overcomes the buoyancy force and as a result of this, no significant flow is induced within the enclosure.

Table 5.5 Effect of Bingham number on different parameters at Pr = 0.1 and Ra = 10^5 .

	Bn = 1	Bn = 3	Bn = 6	Bn = 9	Bn = 18	Bn = 27
$\lvert\psi_{\max}\rvert$	7.457	7.406	6.958	6.481	5.144	4.578
Nu_{avg}	3.393	3.263	3.083	2.898	2.402	2.143
U_{max}	33.762	29.051	23.873	20.615	15.483	14.131
V_{max}	41.255	37.563	32.580	28.217	19.866	16.709

Prandtl number effect

The Fig. 5.11 shows the isotherms and streamlines and the yielded and unyielded zones have been displayed clearly for various Prandtl numbers at Bn = 1 and Ra = 10^5. It illustrates that the gradient of the isotherms on the hot wall decreases as the Prandtl number increases. This trend has been confirmed by the streamlines as the core demonstrates that the convection

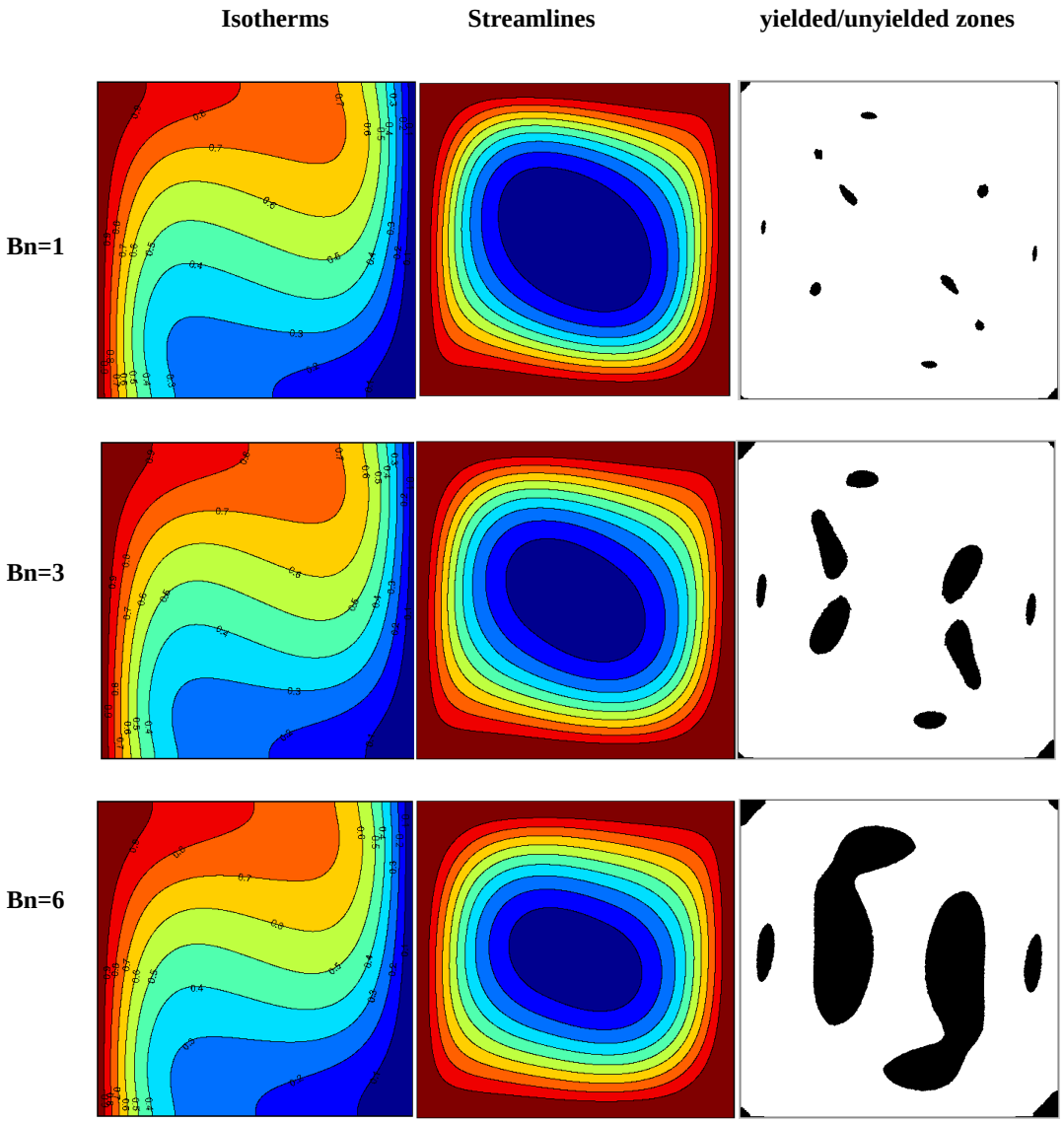

Fig. 5.9 Comparison of the isotherms, streamlines and yielded/unyielded zones for various Bingham numbers at Ra = 10^5 and Pr = 0.1 (Black: unyielded zone; white: yielded zone)·

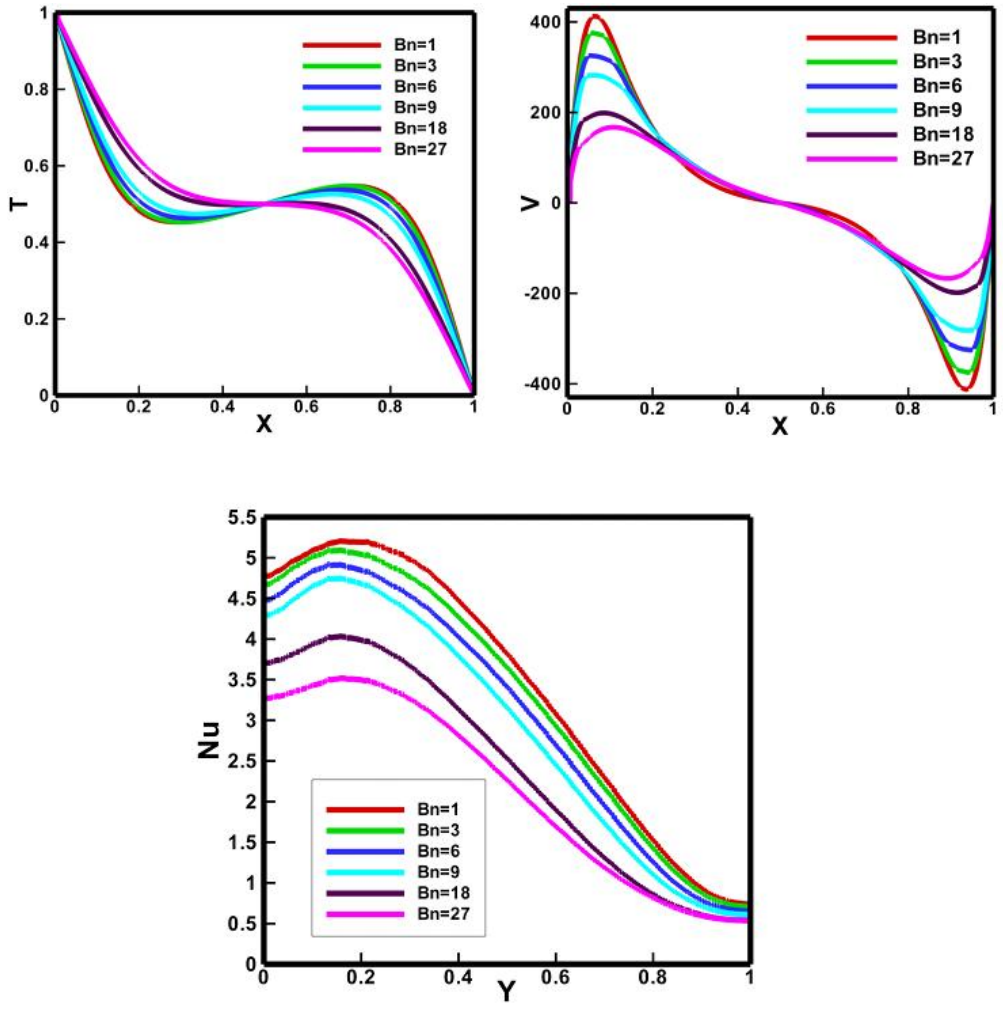

Fig. 5.10 Vertical velocity and temperatures in the middle of the cavity and local Nusselt number on the hot wall for various Bingham numbers at Ra = 10^5 and Pr = 0.1·

process decreases with the rise of the Prandtl number. Further, the Fig. 5.11 shows that the unyielded section for a fixed Bingham and Rayleigh numbers increases with the augmentation of the Prandtl number. In fact, the increase in the unyielded sections at higher Prandtl numbers causes the heat transfer to drop.

The influence of the Prandtl number can be observed on vertical and horizontal velocities and temperature in the middle of the cavity in Fig. 5.12. It is evident that the effect of the Prandtl number on the temperature is marginal although the increase in this number alters the curved shape of the temperature slightly and therefore drops the convection process. The vertical and horizontal velocity distributions in the middle of the cavity indicate that the growth of the Prandtl number lowers the velocity in the cavity drastically. It demonstrates that the development of the unyielded sections, which increase at higher Prandtl numbers, causes the velocities to drop markedly.

Table 5.6 Maximum Bingham numbers (Bn_{max}) for different Rayleigh and Prandtl numbers·

	$Ra = 10^3$	$Ra = 10^4$	$Ra = 10^5$
Pr = 0.1	5	12	37
Pr = 1	2	4.5	11
Pr = 10	1	1.5	4.5

Concluding Remarks

In this study, the OSM based on the Finite Element Method has been utilized to simulate the laminar natural convection of a Bingham fluid in a cavity. The Bingham model for the constitutive equation has been used in the problem without any regularization in contrast with previous research. In fact, Vola et al. (2003) and Turan et al. (2010) have studied the mentioned flow; however, Vola et al. (2003) showed restricted results on the topic and Turan et al. (2010) utilized the regularised bi-viscosity model.

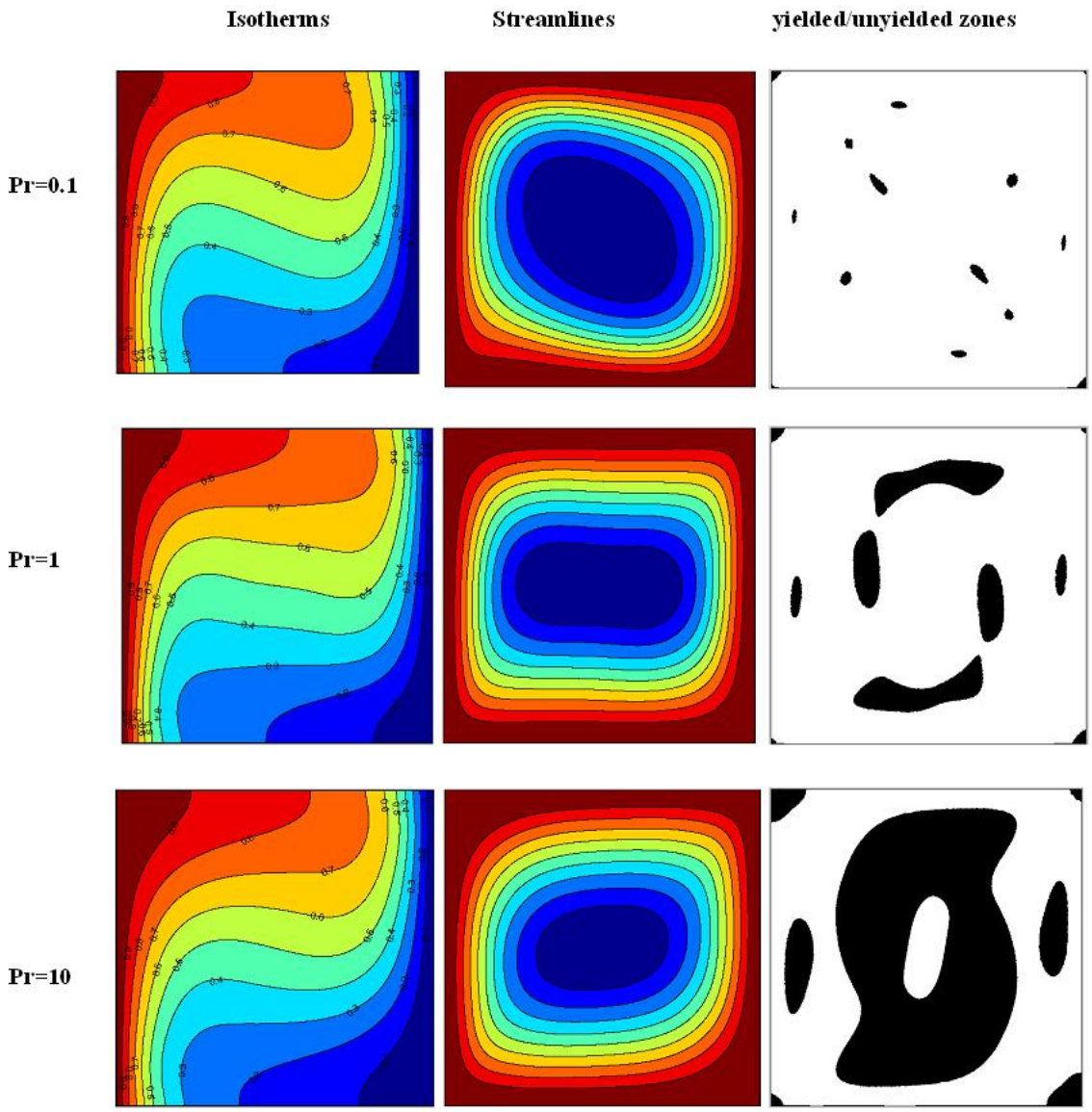

Fig. 5.11 Comparison of the isotherms, streamlines and yielded/unyielded zones for various Prandtl numbers at Ra = 10^5 and Bn = 1 (Black: unyielded zone; white: yielded zone)·

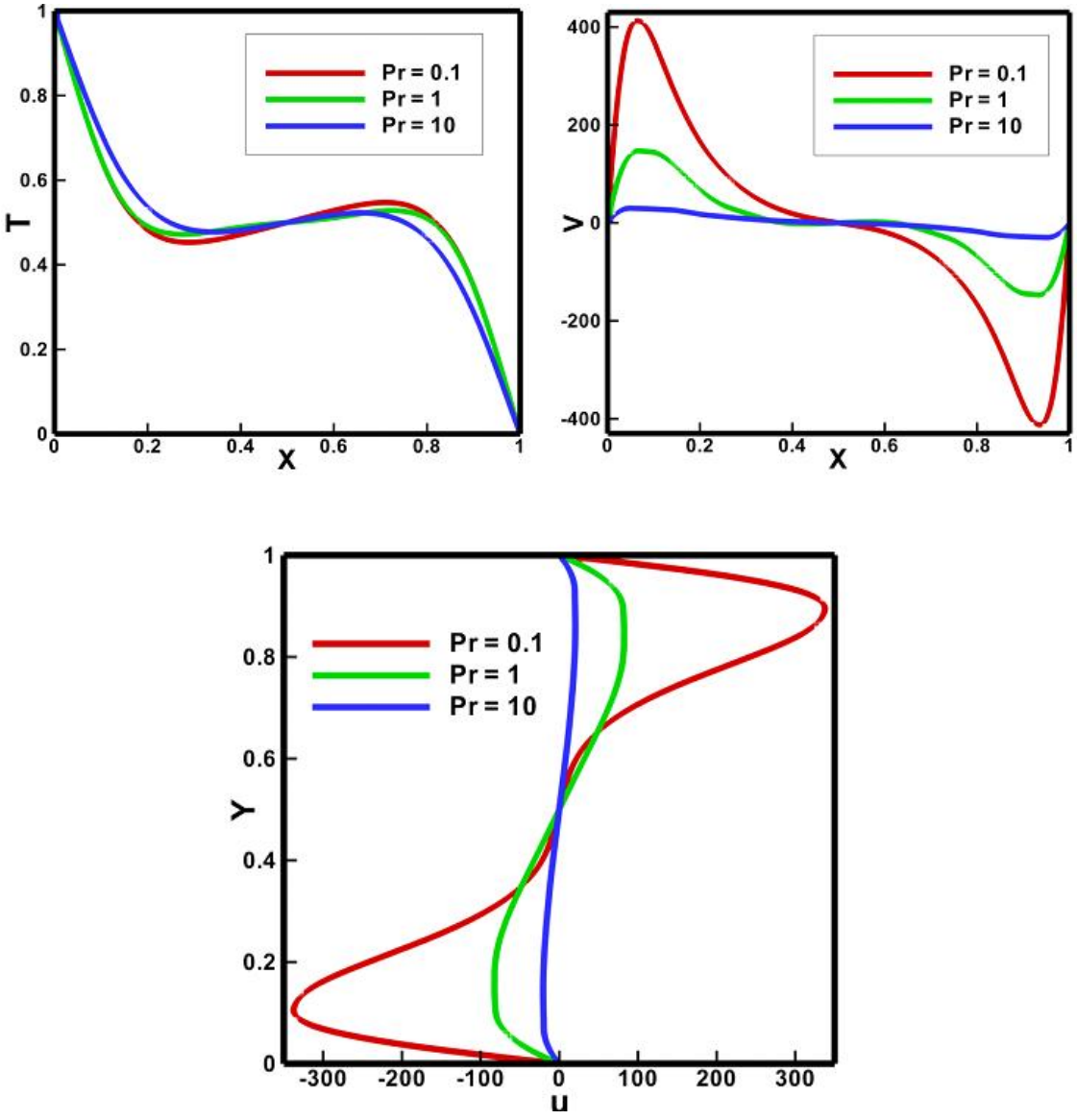

Fig. 5.12 Vertical and horizontal velocities and temperatures in the middle of the cavity for various Prandtl numbers at Ra = 10^5 and Bn = 1·

The pertinent parameters have been scrutinized in the following ranges: the Rayleigh number between, $\mathrm{Ra} = 10^3 - 10^5$, Prandtl number between 0.1 and 10 while the Bingham number is changed over a wide range of Rayleigh numbers. This investigation has been performed for various mentioned parameters and the following conclusions have been reached. The validation with the previous numerical investigations demonstrates that the Operator Splitting Method (OSM) is an appropriate method for the studied problem. It is found that the rise of the Rayleigh number increases the heat transfer as it causes the unyielded zones to decline for various Bingham and Prandtl numbers. The increase in the Bingham number decreases the heat transfer as it enlarges the unyielded sections. The unyielded regions enhance with the augmentation of the Prandtl number for certain Rayleigh and Bingham numbers.

5.3 Natural convection of Bingham fluids using the mesoscopic method

5.3.1 Formulation

In this section, a partial investigation of the natural convection of a Bingham fluid is simulated using the mesoscopic method in order to verify that the results of using the macroscopic OSM are identical to those of the mesoscopic results, when the Bingham constitutive equation is used. Moreover, the mesoscopic method reveals the differences between the Bingham and the Papanastasiou (Papanastasiou (1987)) models. The main difference between this problem and the natural convection of the Newtonian fluid in section 5.1 is observed in the stresses, while the dimensional and non-dimensional variables, and the non-dimensional equations are similar to those for Newtonian fluids. We now list the non-dimensional constitutive equations and stresses of the Bingham and Papanastasiou models.

In the case of the Papanastasiou model (Papanastasiou (1987)), the non-dimensional apparent viscosity is given by

$$\eta = 1 + \frac{\mathrm{Bn}}{II(\mathbf{A}_1)}\left[1 - \exp(-mII(\mathbf{A}_1))\right] \cdot \tag{5.3.1}$$

Hence, the extra stresses are:

$$\tau_{xx} = 2\eta\left(\frac{\partial u}{\partial x}\right),\ \tau_{yy} = 2\eta\left(\frac{\partial v}{\partial y}\right),\ \tau_{xy} = \eta\left(\frac{\partial u}{\partial y} + \frac{\partial v}{\partial x}\right), \tag{5.3.2}$$

where

$$II(\mathbf{A}_1) = \left\{2\left[\left(\frac{\partial u}{\partial x}\right)^2 + \left(\frac{\partial v}{\partial y}\right)^2\right] + \left(\frac{\partial v}{\partial x} + \frac{\partial u}{\partial y}\right)^2\right\}^{\frac{1}{2}} \cdot \tag{5.3.3}$$

In the case of the Bingham model (Huilgol (2015)), the non-dimensional stresses are given by

$$\tau_{xx} = \left[2\left(\frac{\partial u}{\partial x}\right) + \sqrt{2}\ \mathrm{Bn}\Lambda_{xx}\right]\ , \tag{5.3.4a}$$

$$\tau_{yy} = \left[2\left(\frac{\partial v}{\partial y}\right) + \sqrt{2}\ \mathrm{Bn}\Lambda_{yy}\right]\ , \tag{5.3.4b}$$

$$\tau_{xy} = \left[\left(\frac{\partial u}{\partial y} + \frac{\partial v}{\partial x}\right) + \sqrt{2}\ \mathrm{Bn}\Lambda_{xy}\right] \cdot \tag{5.3.4c}$$

The non-dimensional parameters for the problem are as follows:

$$\mathrm{Bn} = \frac{\tau_y L}{\eta U}\ , \tag{5.3.5}$$

$$\mathrm{Ra} = \frac{\beta g_y L^3 (T_H - T_C)}{\nu\,\alpha}\ , \tag{5.3.6}$$

$$\mathrm{Pr} = \frac{\nu}{\alpha} \ . \tag{5.3.7}$$

The numerical simulations using the two different models and methods have been compared in Fig. 5.13 and Fig. 5.14. The figures show the yielded/unyielded zones in the natural convection problem when Bn = 0.1 and Bn = 1. It is seen that the results of the Bingham model using the OSM and the mesoscopic method are identical for both Bingham numbers, whereas these for the regularised model are not so when Bn = 1, which is to be expected. Those comparisons show that one can apply the mesoscopic method to study convection problems in yield stress fluids.

5.4 Mixed convection of a Bingham fluid using the mesoscopic method

5.4.1 Theoretical formulation

The geometry of the present problem is shown in figure 5.15. It consists of a two-dimensional cavity with a height L. The temperature of the left wall is maintained at a higher temperature than the right wall. The horizontal walls are adiabatic and impermeable, and the top wall is driven from the left to right at a constant speed. The cavity is filled with a Bingham fluid. The fluid is incompressible, and the flow is laminar. The Grashof number is kept at Gr = 10000, while the Reynolds number varies from Re = 100 to 500, and 1000, while the Prandtl number takes on the values 0.1, 1, and 10. The buoyancy force is approximated by the standard Boussinesq model.

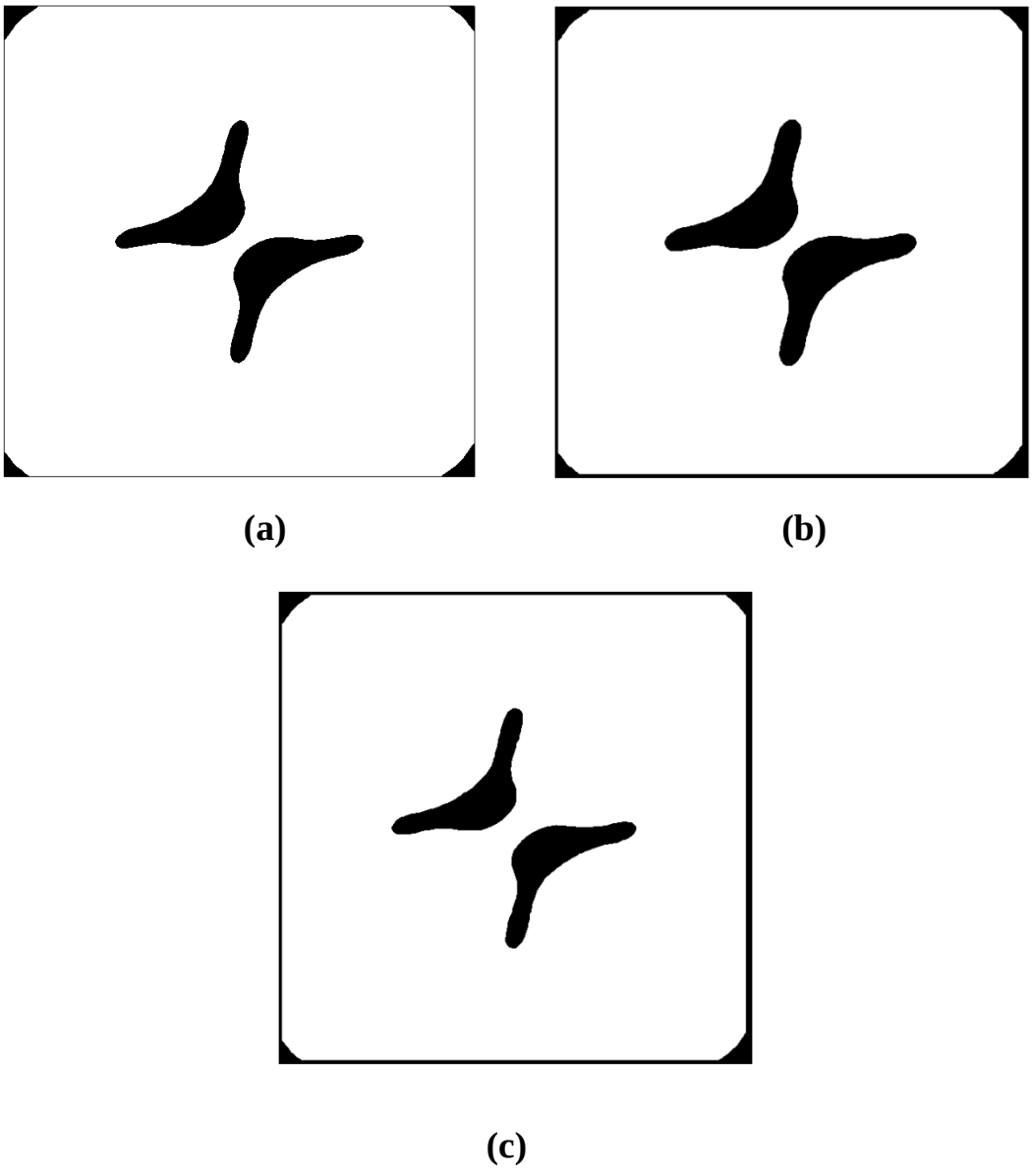

Fig. 5.13 Comparison of yielded and unyielded sections at Bn = 0.1, Pr = 0.71, and Ra $= 10^3$ for (a) The Bingham model using the Operator Splitting Method (b) The Bingham model using the mesoscopic method (c) The Papanatasiou model using the mesoscopic method, showing slightly larger yielded zones·

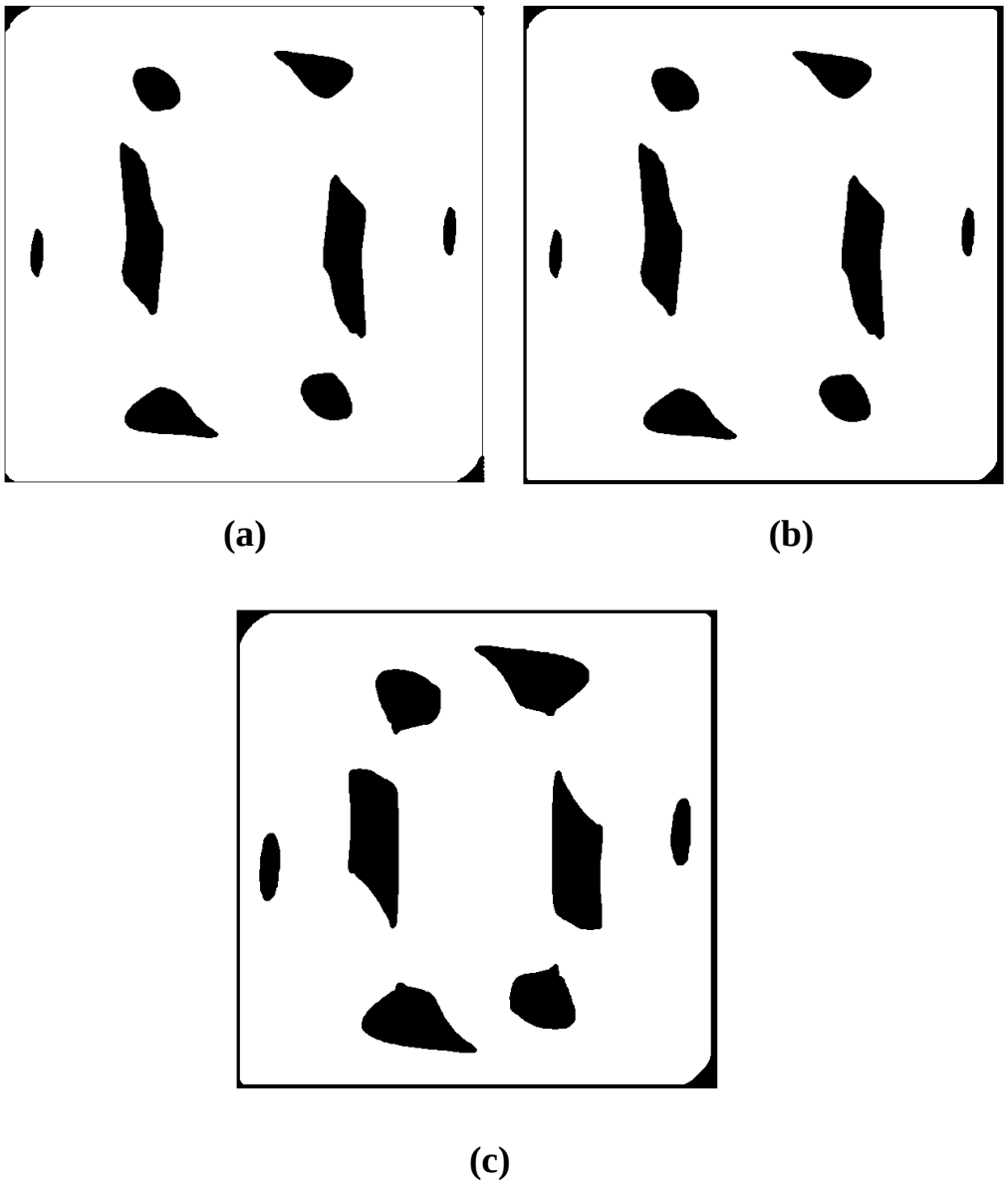

Fig. 5.14 Comparison of yielded and unyielded sections at Bn = 1, Pr = 0.71, and Ra $= 10^5$ for (a) The Bingham model using the Operator Splitting Method (b) The Bingham model using the mesoscopic method (c) The Papanatasiou model using the mesoscopic method, showing a slight decrease in the site of the yielded region·

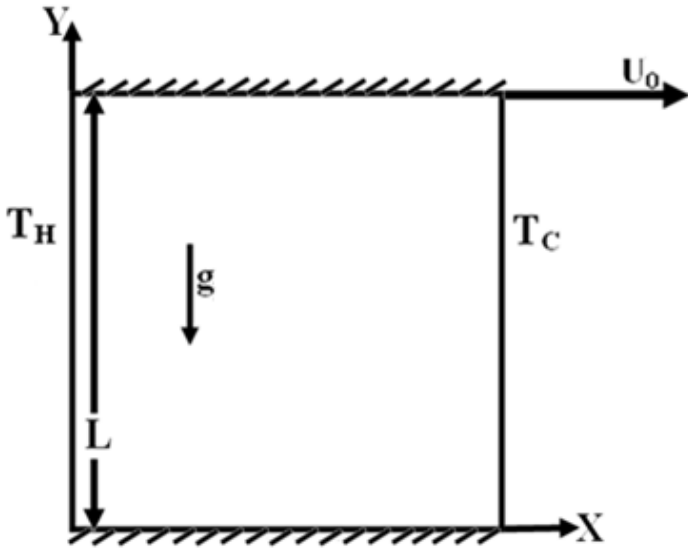

Fig. 5.15 Geometry of mixed convection

5.4.2 Dimensional equations

Based on the above assumptions, denoting by $\mathbf{u} = u\mathbf{i} + v\mathbf{j}$ the velocity field, ρ the density, and T the temperature field, and applying the Boussinesq approximation, Cauchy's equations for the steady flow of an incompressible fluid are:

$$\frac{\partial u}{\partial x} + \frac{\partial v}{\partial y} = 0, \tag{5.4.1}$$

$$\rho\left(u\frac{\partial u}{\partial x} + v\frac{\partial u}{\partial y}\right) = -\frac{\partial p}{\partial x} + \frac{\partial \tau_{xx}}{\partial x} + \frac{\partial \tau_{xy}}{\partial y}, \tag{5.4.2}$$

$$\rho\left(u\frac{\partial v}{\partial x} + v\frac{\partial v}{\partial y}\right) = -\frac{\partial p}{\partial y} + \frac{\partial \tau_{xy}}{\partial x} + \frac{\partial \tau_{yy}}{\partial y} + \rho g\left[1 + \beta\left(T - T_C\right)\right], \tag{5.4.3}$$

where β is the coefficient of thermal expansion. Next, ignoring viscous dissipation,

$$u\frac{\partial T}{\partial x} + v\frac{\partial T}{\partial y} = \alpha\left(\frac{\partial^2 T}{\partial x^2} + \frac{\partial^2 T}{\partial y^2}\right), \tag{5.4.4}$$

where α is the conductivity coefficient. Let the pressure p be written as the sum $p = p_s + p_d$, where the static part p_s accounts for gravity alone, and p_d is the dynamic part. Thus,

$$-\frac{\partial p_s}{\partial y} = \rho g \cdot \tag{5.4.5}$$

The flow domain is given by $\Omega = (0,L) \times (0,L)$, and the boundary $\Gamma = \partial\Omega$. It is the union of four disjoint subsets:

$$\Gamma_1 = \{(x,y), x = 0, 0 \leq y \leq L\}, \quad \Gamma_2 = \{(x,y), x = L, 0 \leq y \leq L\}, \tag{5.4.6}$$

$$\Gamma_3 = \{(x,y), 0 \leq x \leq L, y = 0\}, \quad \Gamma_4 = \{(x,y), 0 \leq x \leq L, y = L\}. \tag{5.4.7}$$

The boundary condition for the velocity is straightforward:

$$\mathbf{u}|_{\Gamma_1} = \mathbf{u}|_{\Gamma_2} = \mathbf{u}|_{\Gamma_3} = \mathbf{0}, \mathbf{u}|_{\Gamma_4} = U_0\mathbf{i}. \tag{5.4.8}$$

The boundary conditions for the temperature are:

$$T|_{\Gamma_1} = T_H, T|_{\Gamma_2} = T_C, \partial T/\partial y|_{\Gamma_3} = 0, \partial T/\partial y|_{\Gamma_4} = 0. \tag{5.4.9}$$

5.4.3 Non-dimensional equations

In order to proceed to the numerical solution of the system, the following non dimensional variables are introduced.

$$\bar{t} = tU_0/L, \quad \bar{x} = x/L, \quad \bar{y} = y/L, \quad \bar{u} = u/U_0, \quad \bar{v} = v/U_0. \tag{5.4.10}$$

$$\bar{p}_d = p_d/\rho {U_0}^2, \quad \bar{T} = (T - T_C)/(T_H - T_C), \tag{5.4.11}$$

where U_0 is the speed of the upper wall.

By substitution of Eqs. (5.4.10) and (5.4.11) into Eqs. (5.4.1) - (5.4.4) and dropping the bar notation for convenience, the following system of non-dimensional equations is derived:

$$\frac{\partial u}{\partial x}+\frac{\partial v}{\partial y}=0, \tag{5.4.12}$$

$$u\frac{\partial u}{\partial x}+v\frac{\partial u}{\partial y}=-\frac{\partial p_d}{\partial x}+\frac{1}{\mathrm{Re}}\left(\frac{\partial \tau_{xx}}{\partial x}+\frac{\partial \tau_{xy}}{\partial y}\right), \tag{5.4.13}$$

$$u\frac{\partial v}{\partial x}+v\frac{\partial v}{\partial y}=-\frac{\partial p_d}{\partial y}+\frac{1}{\mathrm{Re}}\left(\frac{\partial \tau_{xy}}{\partial x}+\frac{\partial \tau_{yy}}{\partial y}\right)+\frac{\mathrm{Gr}}{\mathrm{Re}^2}T, \tag{5.4.14}$$

$$u\frac{\partial T}{\partial x}+v\frac{\partial T}{\partial y}=\frac{1}{\mathrm{Re}\,\mathrm{Pr}}\left(\frac{\partial^2 T}{\partial x^2}+\frac{\partial^2 T}{\partial y^2}\right). \tag{5.4.15}$$

In the case of the Papanastasiou model (Papanastasiou (1987)), the non-dimensional apparent viscosity is given by

$$\eta=1+\frac{\mathrm{Bn}}{II(\mathbf{A}_1)}\left[1-\exp(-mII(\mathbf{A}_1))\right]\cdot \tag{5.4.16}$$

Hence, the extra stresses are:

$$\tau_{xx}=2\eta\left(\frac{\partial u}{\partial x}\right),\ \tau_{yy}=2\eta\left(\frac{\partial v}{\partial y}\right),\ \tau_{xy}=\eta\left(\frac{\partial u}{\partial y}+\frac{\partial v}{\partial x}\right), \tag{5.4.17}$$

where

$$II(\mathbf{A}_1) = \left\{ 2\left[\left(\frac{\partial u}{\partial x}\right)^2 + \left(\frac{\partial v}{\partial y}\right)^2 \right] + \left(\frac{\partial v}{\partial x} + \frac{\partial u}{\partial y}\right)^2 \right\}^{\frac{1}{2}}. \tag{5.4.18}$$

In the case of the Bingham model, the non-dimensional stresses are given by

$$\tau_{xx} = \left[2\left(\frac{\partial u}{\partial x}\right) + \sqrt{2}\ \mathrm{Bn}\Lambda_{xx} \right] , \tag{5.4.19a}$$

$$\tau_{yy} = \left[2\left(\frac{\partial v}{\partial y}\right) + \sqrt{2}\ \mathrm{Bn}\Lambda_{yy} \right] , \tag{5.4.19b}$$

$$\tau_{xy} = \left[\left(\frac{\partial u}{\partial y} + \frac{\partial v}{\partial x}\right) + \sqrt{2}\ \mathrm{Bn}\Lambda_{xy} \right] . \tag{5.4.19c}$$

The non-dimensional parameters for the problem are as follows:

Grashof number:

$$\mathrm{Gr} = \frac{\rho^2 \beta g_y L^3 (T_H - T_C)}{\eta^2}, \tag{5.4.20}$$

Prandtl number:

$$\mathrm{Pr} = \frac{\eta}{\rho\, \alpha}, \tag{5.4.21}$$

Reynolds number:

$$\mathrm{Re} = \frac{\rho\, U_0 L}{\eta}, \tag{5.4.22}$$

Bingham number:

$$\mathrm{Bn} = \frac{\tau_y L}{\eta\, U_0}. \tag{5.4.23}$$

5.4.4 Applied parameters

With consideration to the dimensionless equations, the cited stresses in the fourth section Eqs.(5.4.17) and (5.4.19) should be divided by the Reynolds number (Re) and applied to the

mentioned stresses in Eqs.(3.3.10)- (3.3.13).

The buoyancy force acts as the external force and with consideration to Eqs.(3.4.9)-(3.4.14), the non-dimensional form of the functions F_α are given by

$$F_\alpha = 0, \quad \alpha = 0,2,4,6,8, \tag{5.4.24a}$$

$$F_\alpha = \boldsymbol{\xi}_\alpha \cdot \mathbf{N}, \quad \alpha = 1,3,5,7, \tag{5.4.24b}$$

$$\mathbf{N} = \frac{1}{2\sigma^2}\left(\frac{\mathrm{Gr}\,T}{\mathrm{Re}^2}\right)\mathbf{j}\,\cdot \tag{5.4.24c}$$

The parameters of the internal energy distribution function which are given by Eqs.(3.3.42) and (3.3.43) are as follows:

$$D_0 = T, \quad D_1 = D_2 = 0, \tag{5.4.25a}$$

$$\mathbf{E}_1 = \frac{1}{2\sigma^2}\left(T\mathbf{u} - \frac{1}{\mathrm{Re}\,\mathrm{Pr}}\nabla T\right), \quad \mathbf{E}_2 = \mathbf{0}. \tag{5.4.25b}$$

The local and the average Nusselt numbers at the hot wall with the utilization of the dimensionless parameters are obtained from

$$\mathrm{Nu_h} = -\frac{\partial T}{\partial x}, \;\; x = 0, \tag{5.4.26}$$

$$\mathrm{Nu_{avg}} = \int_0^1 \mathrm{Nu_h}\, dy. \tag{5.4.27}$$

5.4.5 Parameters and grid independence

The Thermal Finite Difference Discrete Flux Method (TFDDFM) scheme based on Lattice Boltzmann Method (LBM) has been employed in the numerical simulation of a laminar

mixed convection flow in a lid-driven cavity filled with a Bingham fluid. This problem has been investigated at different Reynolds numbers (Re = 100, 500 and 1000), Bingham numbers (Bn = 0, 1, 5 and 10), and Prandtl numbers (Pr = 0.1, 1, and, 10) while the Grashof number is fixed at Gr = 10,000. An extensive mesh testing procedure was conducted to guarantee a grid independent solution. Seven different mesh combinations were explored for the case of Re = 1000, Pr = 1 and Bn = 10 using the Papanastasiou model. It was confirmed that the grid size (200*200) ensured a grid independent solution as portrayed in figure 5.16 and Table 5.7. In addition, we set $\Delta t = 0.0001$ and the value of σ was varied in each iteration according to Eq. (A7). To check the accuracy of the present results, the code was validated with the published studies on mixed convection in a cavity; see Table 5.8. Secondly, the accuracy of the applied code in a lid-driven cavity in the absence of the energy equation using the Papanastasiou model was validated through a comparison with Neofytou (2005). The results are shown in figure 4.5 where the u and v velocities profiles demonstrate the accuracy of the present simulation for Bn = 1 and Re = 100. Finally, in figure 5.13, the results obtained by Huilgol and Kefayati (2015) in their study of the natural convection in a cavity of a Bingham fluid based on the finite element method are compared with those obtained in the current study. Both the and the regularised models are considered when the Bingham number is 0.1. The agreement is found to be excellent.

Table 5.7 Grid independence study at Re= 1000, Bn=1, and Pr=1

Mesh size	Nu_{avg}	$\lvert\psi_{\max}\rvert$
120*120	8.609	0.0859
140*140	8.591	0.0864
160*160	8.576	0.0868
180*180	8.562	0.0870
200*200	8.549	0.0872
220*220	8.549	0.0872
240*240	8.549	0.0872

Table 5.8 Comparison of average Nusselt number with results available in the literature

	Re = 1	Re = 100	Re = 400	Re = 1000
Present work	1.0094	2.09	4.0808	6.5469
Waheed (2009)	1.0003	2.03116	4.0246	6.48423
Tiwari and Das (2007)	-	2.10	3.85	6.33
Abdelkhalek (2008)	-	1.985	3.8785	6.345
Khanafer et al. (2007)	-	2.02	4.01	6.42
Sharif (2007)	-	-	4.05	6.55
Khanafer and Chamkha (1999)	-	2.01	3.91	6.33
Iwatsu et al. (1993)	-	1.94	3.84	6.33

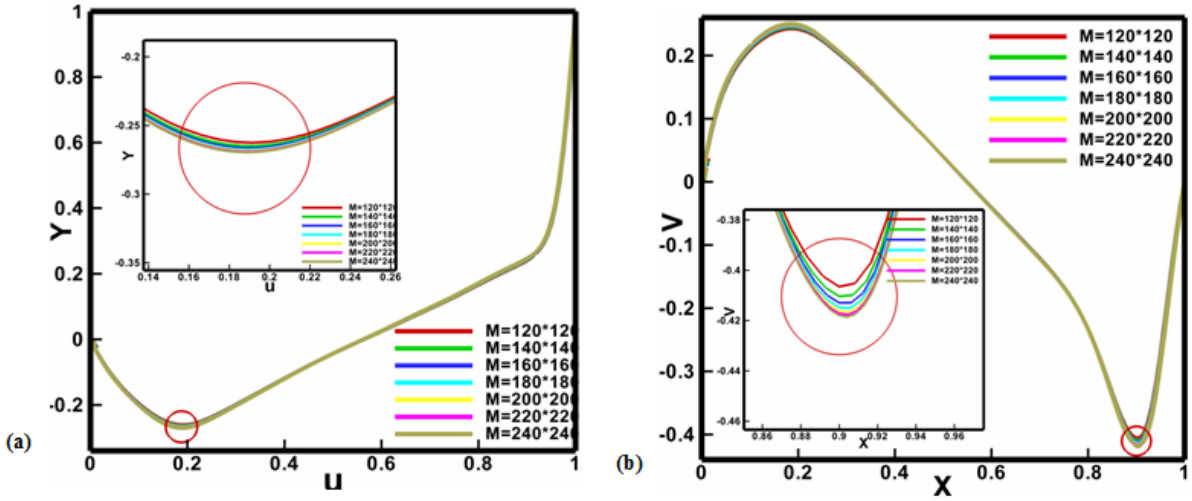

Fig. 5.16 Comparison of velocity distribution at $x = 0.5$ and $y = 0.5$ for (a) u and (b) v respectively at Re = 1000, Pr = 1 and Bn = 10

5.4.6 Results and discussion

The numerical simulation has been conducted using the Papanastasiou model only because the required number of iterations is less than that using the Bingham model. However, it has to emphasised that as the Bingham number increases, the results of the two models diverge. For example, see Figs. 5.13 and 5.14 where the yielded/unyielded zones in the natural convection problem are depicted when the Bingham number Bn = 0.1 and when Bn = 1. It is seen that the results for the model using the finite element method and the current

one are identical, whereas those for the regularised model are not so when Bn = 1. While it is generally believed that increasing the value of the parameter m will bring the predictions of the Papanastasiou model closer to that of the Bingham model, discrepancies arise with an increase in the Bingham number. As shown by Glowinski (2003), for the solution $\mathbf{u}_\varepsilon$ of the regularised model to be a good approximation to the exact solution $\mathbf{u}$, the regularisation parameter ε has to be small; for our purposes, one can take $\varepsilon = 1/m$. However, when this parameter is small, the initial/boundary value problem is badly conditioned whenever the unyielded zone is large. Since an increase in the Bingham number results in a larger unyielded zone, it is clear that increasing the value of m may not provide quantitatively accurate results. This can be seen in Figs. 5.17 and 5.18, for an increase in m from 100 to 1000 when Bn = 1 and 10 does not produce any significant improvement in the predictions of the regularised model as far as the yielded/unyielded regions are concerned. Similar observations regarding the streamlines and the isotherms can be made as seen in Figs. 5.17 and 5.18 respectively. Finally, it can be seen in Fig. 15(b) in Dimakopoulos et al. (2013) that even when $m = 10^6$, there is a fair amount of divergence between the predictions of the Papanastasiou model and the results derived from ALM, as the Bingham number increases. Hence, the results presented here have to be accepted as being qualitatively accurate to those obtained by using the exact constitutive equation.

The figure 5.19 presents the isotherms for different Bingham and Reynolds numbers at Prandtl number of Pr = 1 using the Papanastasiou model with the regularisation parameter of $m = 1000$. At Bn = 0, it is evident that the increase in the Reynolds number alters the shape of the isotherms significantly since the isotherms on the hot wall come together more and more. In fact, the augmentation of the forced flow in the fixed buoyant flow causes the cited pattern to be created. In other words, the trend demonstrates that the convection process has strengthened with the increase in Reynolds number. However, it also shows that the effect of Reynolds number enhancement is more noteworthy from Re = 100 to 500 while the changes

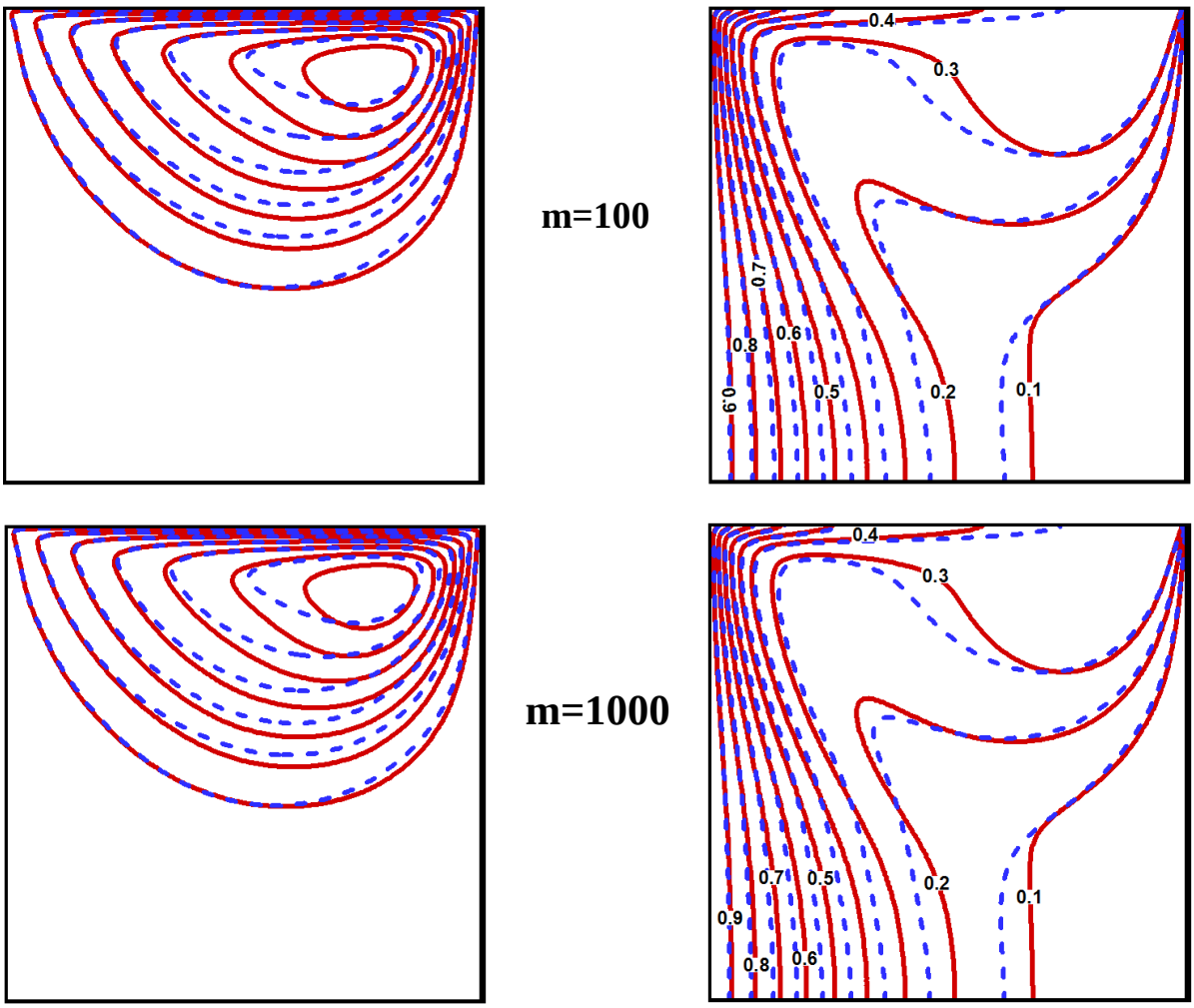

Fig. 5.17 Comparison between the streamlines and the isotherms of the Bingham model (The Black line) and the Papanastasiou model for different m parameters of m = 100 (The red line) and m = 1000 (The green line) at Bn = 1, Re = 500, and Pr = 1 ·

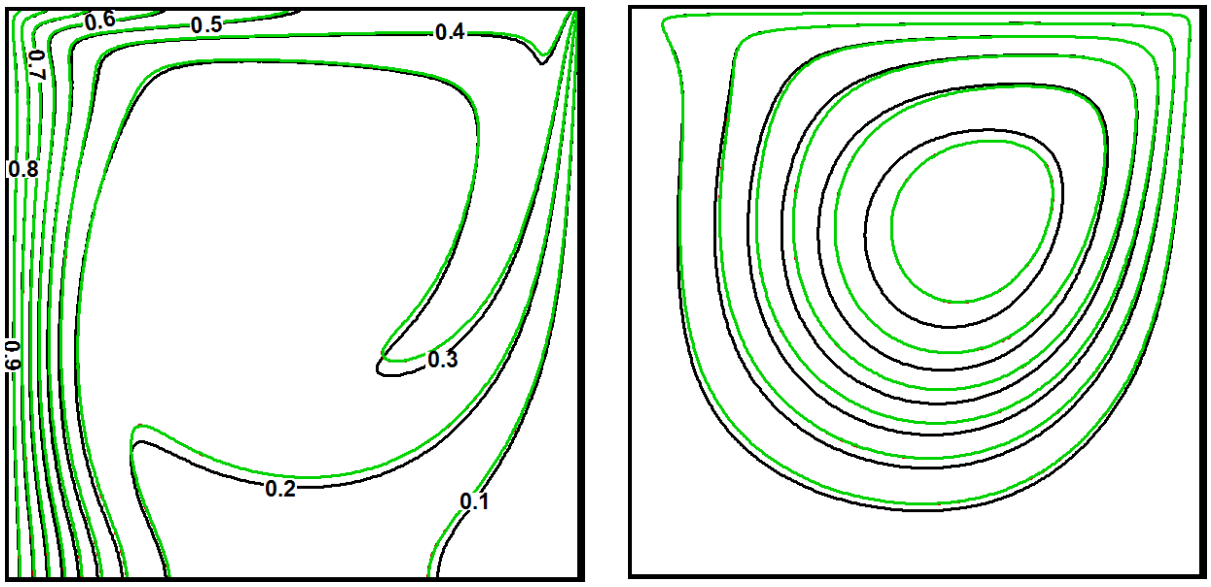

Fig. 5.18 Comparison between the streamlines and the isotherms of the Bingham model (Simple red line) and the Papanastasiou model (Dashed blue line) at Bn = 10, Re = 500, and Pr = 1 ·

are insignificant from Re = 500 to 1000. Increasing the Bingham number to Bn = 1 affects the isotherms for various Reynolds numbers marginally, although the isotherms demonstrate that the heat transfer decreases slightly; this is can be seen from the isotherms of T = 0.3 and 0.2 for Re = 500 and 1000 respectively. However, at Bn = 5, the isotherms, most notably when Re = 500 and 1000 are of a different form entirely. The increase in the Bingham number has caused the isotherm gradients on the hot wall to decline and as a result, the convection process is weakened. Obviously, as the Bingham number increases, conductive heat transfer dominates the region next to the hotter wall, while next to the cooler one, convective heat transfer occurs. However, the movement of the upper plate to the right means that convective heat transfer can never disappear totally, for any finite Bingham number.

The figure 5.20 illustrates the streamlines for different Bingham and Reynolds numbers at the Prandtl number Pr=1 using the Papanastasiou model with the regularisation parameter of $m = 1000$. For Bn = 0, a clockwise circulation has occupied the cavity at Re = 100 where

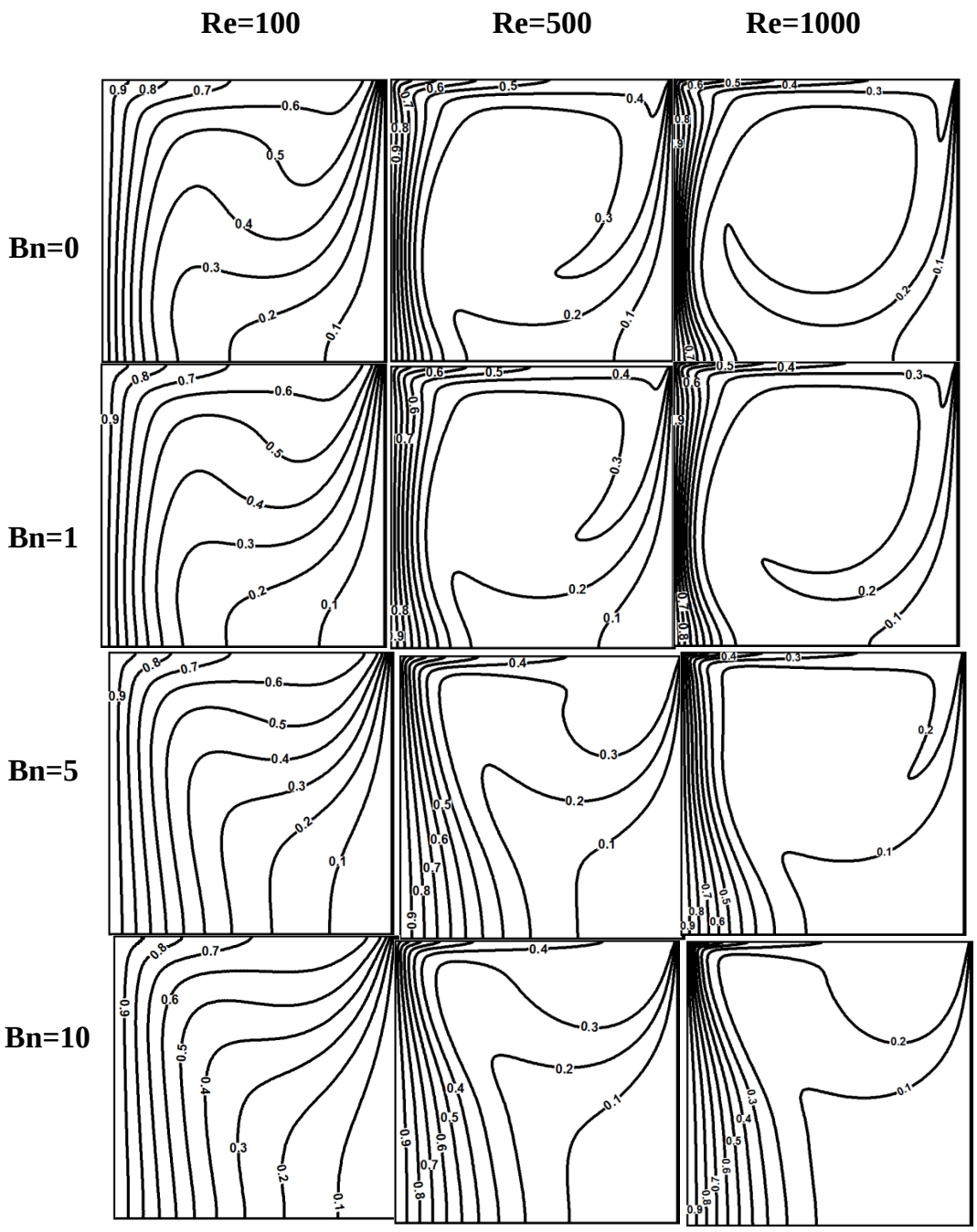

Fig. 5.19 Comparison of the isotherms for different Reynolds and Bingham numbers at Pr = 1·

the buoyancy effect is dominant. But, at Re = 500, the forced flow enhancement results in a secondary counterclockwise circulation at the bottom right corner of the enclosure. The presence of the secondary vortex proves that the convection procedure has been intensified by the rise of the Reynolds number. This can be observed clearly at Re = 1000 with another weaker circulation in the bottom left corner of the cavity which rotates counterclockwise. In fact, the intensity of the inertia force causes the core of the main circulation to move to the middle of the cavity while opposite circulations form at the bottom corners of the enclosure. For Bn = 1, the observed effect of the inertia force due to the rise of Reynolds number declines as the secondary circulation disappears at Re = 500 and a very small secondary vortex appears at Re = 1000. The inclination of the streamlines cores to the upper right wall at Bn = 5 confirms that natural convection has weakened and the role of the forced flow has become significant; however, the removal of the minor opposite vortices at the bottom of the cavity demonstrates that the convection process has fallen generally. At Bn = 5 and 10, it is clear that the core of the main circulation becomes closer to the upper section and therefore it can be stated that the increase in the Bingham number decreases the free convection influence generally and ameliorates the forced flow effect. On the other hand, with an increase in the Reynolds number, the core of the main circulation moves close to the upper wall.

Next, the figure 5.21 indicates the yielded and unyielded zones for different Bingham and Reynolds numbers at a Prandtl number Pr=1 using the Papanastasiou model with the regularisation parameter of $m = 1000$. It shows that the rise of the Bingham number for various Reynolds numbers enhances the unyielded zone steadily.

The figures 5.22, 5.23, and 5.24 demonstrate the effect of the Bingham number using the Papanastasiou model with the regularisation parameter of $m = 1000$ on the local Nusselt number on the hot wall, vertical and horizontal velocities in the middle of the cavity as well as the temperature profile at y = 0.5 in different Reynolds numbers. The local Nusselt number increases with the rise of the Reynolds number clearly for each Bingham number. Moreover,

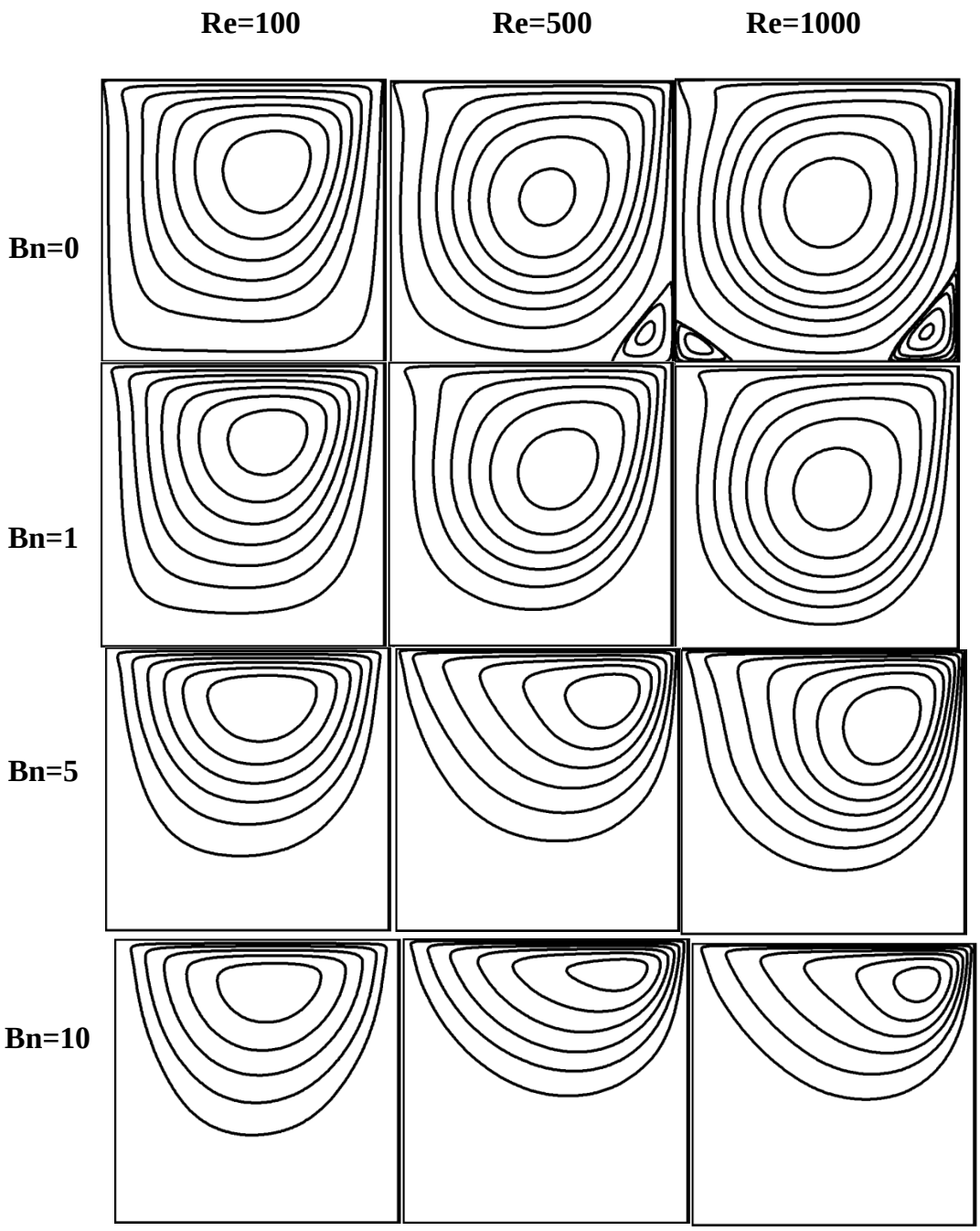

Fig. 5.20 Comparison of the streamlines for different Reynolds and Bingham numbers at Pr = 1·

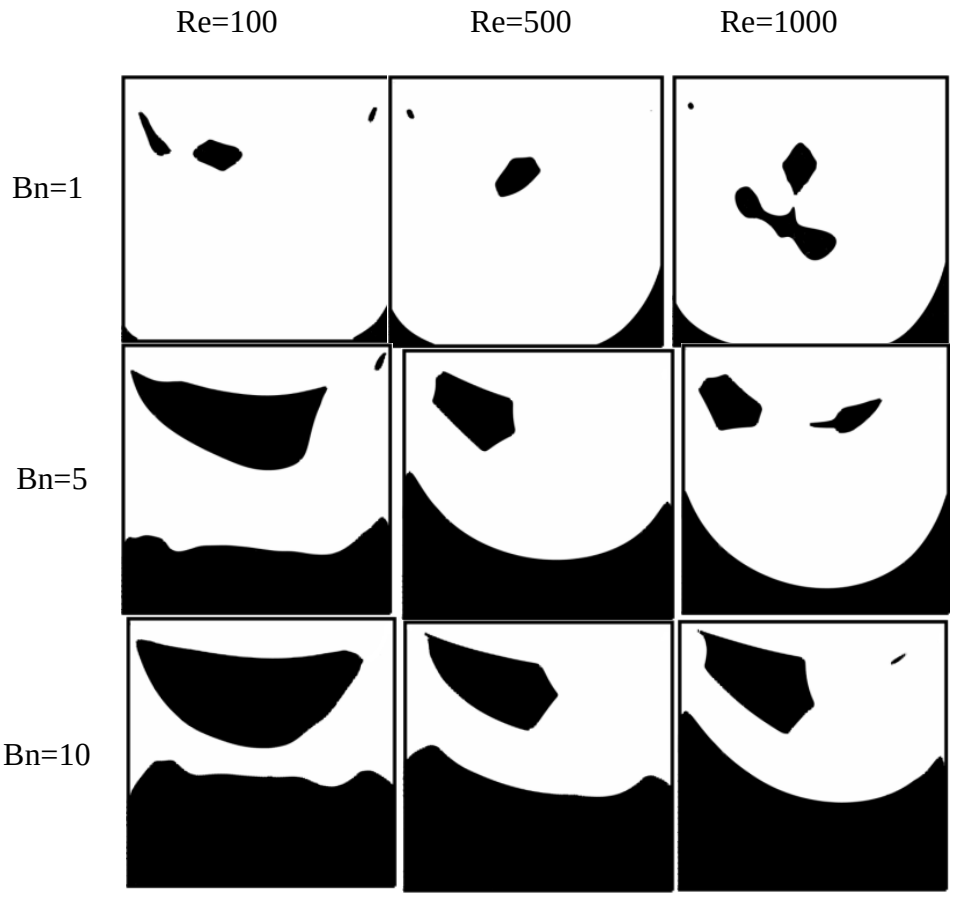

Fig. 5.21 Comparison of the streamlines for different Reynolds and Bingham numbers at Pr = 1·

as the Bingham number augments from Bn = 0 to 1, the local Nusselt number drops while the velocity profiles follow the same trend. However, the local Nusselt number shows a different pattern at higher Bingham numbers where the maximum amount is observed close to the top wall in contrast with Bn = 0 and 1. In other words, for Bn ≥ 5, the local Nusselt number is flat at $y < 0.5$ and thereafter enhances gradually. The main reason for the pattern is the shape of the unyielded section at $y < 0.5$ which results in a considerable drop in the heat transfer. It is noticeable that the vertical velocity in the middle of the cavity drops as the Bingham number increases. It indicates that the strength of the natural and forced convection forces becomes increasingly weak in comparison to the viscous flow resistance for increasing values of the Bingham number. Hence, the fluid movement becomes more sluggish and eventually it leads to a drop in convection with the rise of Bingham number. This statement is further supported by the dimensionless temperature profiles as they become smoother in the middle of the cavity with declining Bingham numbers. The decrease in the curvature of the temperature and velocity distributions demonstrates that the convection process weakens as the Bingham number enhances. In addition, the increase of forced convection is clearly noticeable with the enhancement of the Reynolds number as the temperature profile becomes flatter. In fact, it proves that the convection process increases with the rise of the Reynolds number. Another phenomenon which has the potential to distinguish the role the Bingham number plays in decreasing the convection transport is the horizontal velocity in the middle of the cavity. The horizontal velocity progressively becomes linear with the rise of the Bingham number as a result of the weakening of convective transport. Further, the maximum value of the horizontal velocity increases in the first half of the cavity ($x < 0.5$) as the Reynolds number increases.

The influence of the Prandtl number on the streamlines, the isotherms, and the yielded/unyielded sections for different Reynolds numbers at Bn = 5 using the Papanastasiou model with the regularisation parameter $m = 1000$ is exhibited in figure 5.25. It illustrates that the gradient of the isotherms on the hot wall increases markedly with the rise of the Prandtl number

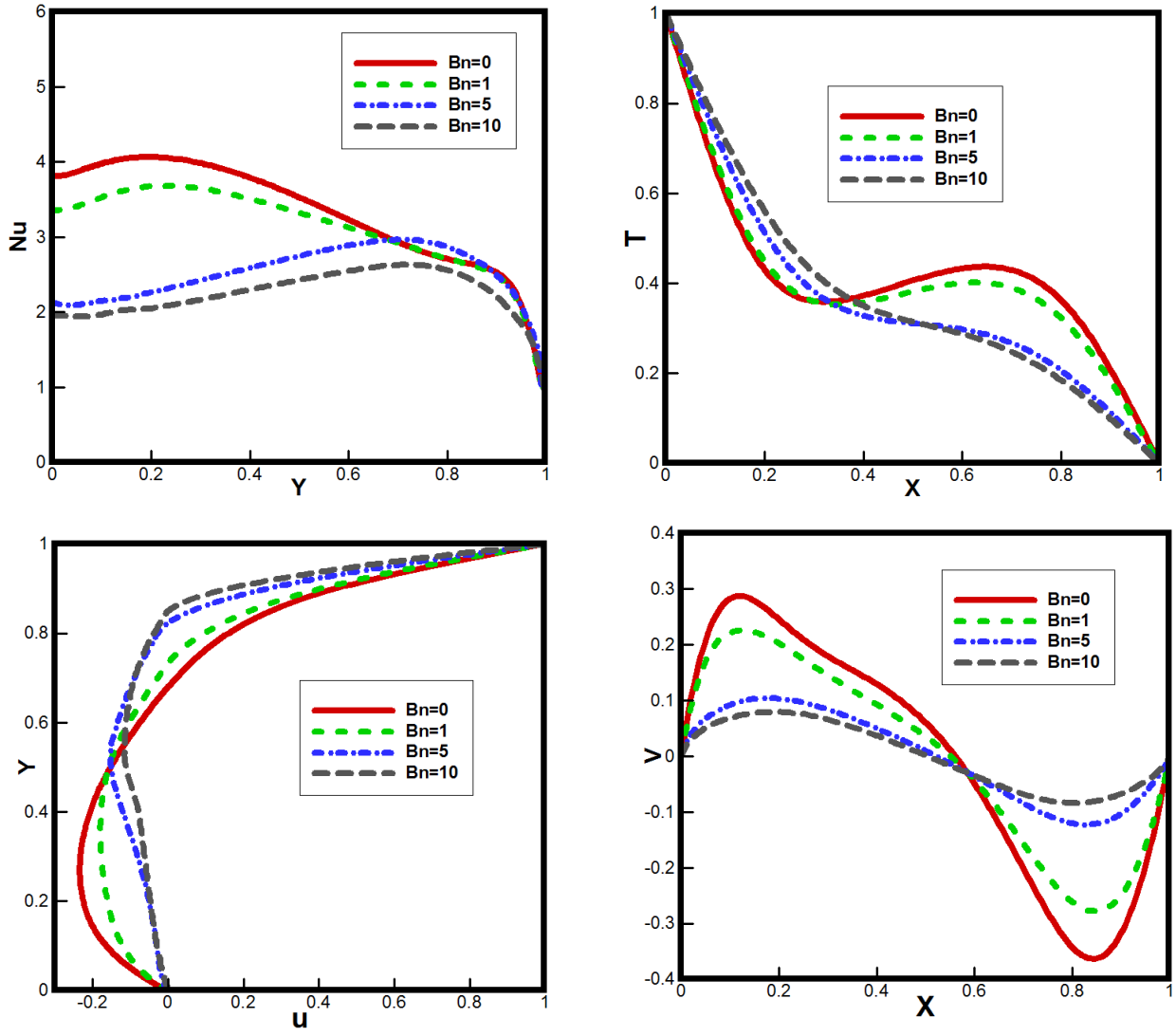

Fig. 5.22 Vertical velocity (v) and temperature distribution (T) at $y = 0.5$, horizontal velocity profile (u) at $x = 0.5$ and the local Nusselt number at the hot wall for different Reynolds and Bingham numbers at Pr = 1 and Re=100·

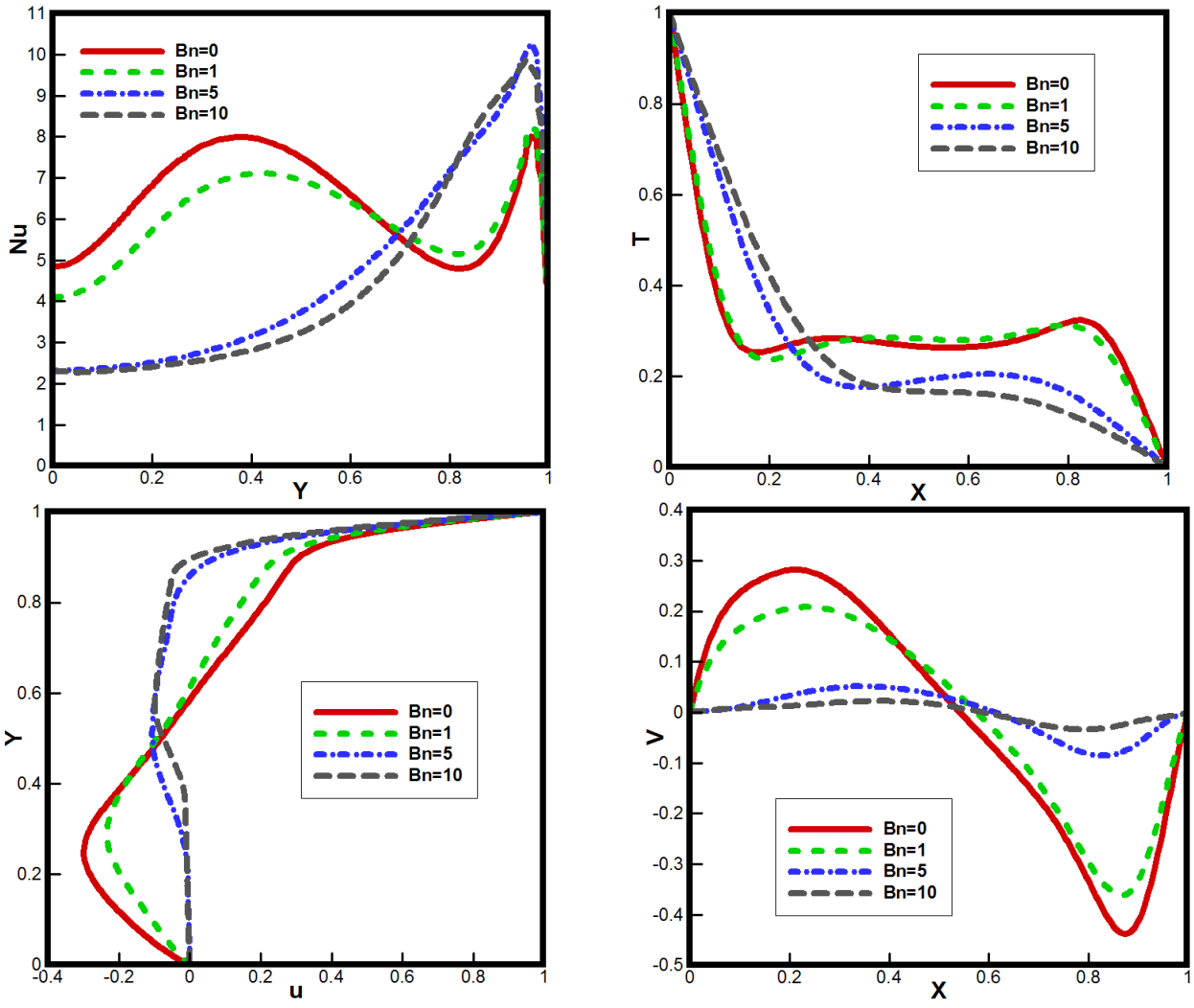

Fig. 5.23 Vertical velocity (v) and temperature distribution (T) at $y = 0.5$, horizontal velocity profile (u) at $x = 0.5$ and the local Nusselt number at the hot wall for different Reynolds and Bingham numbers at Pr = 1 and Re=500·

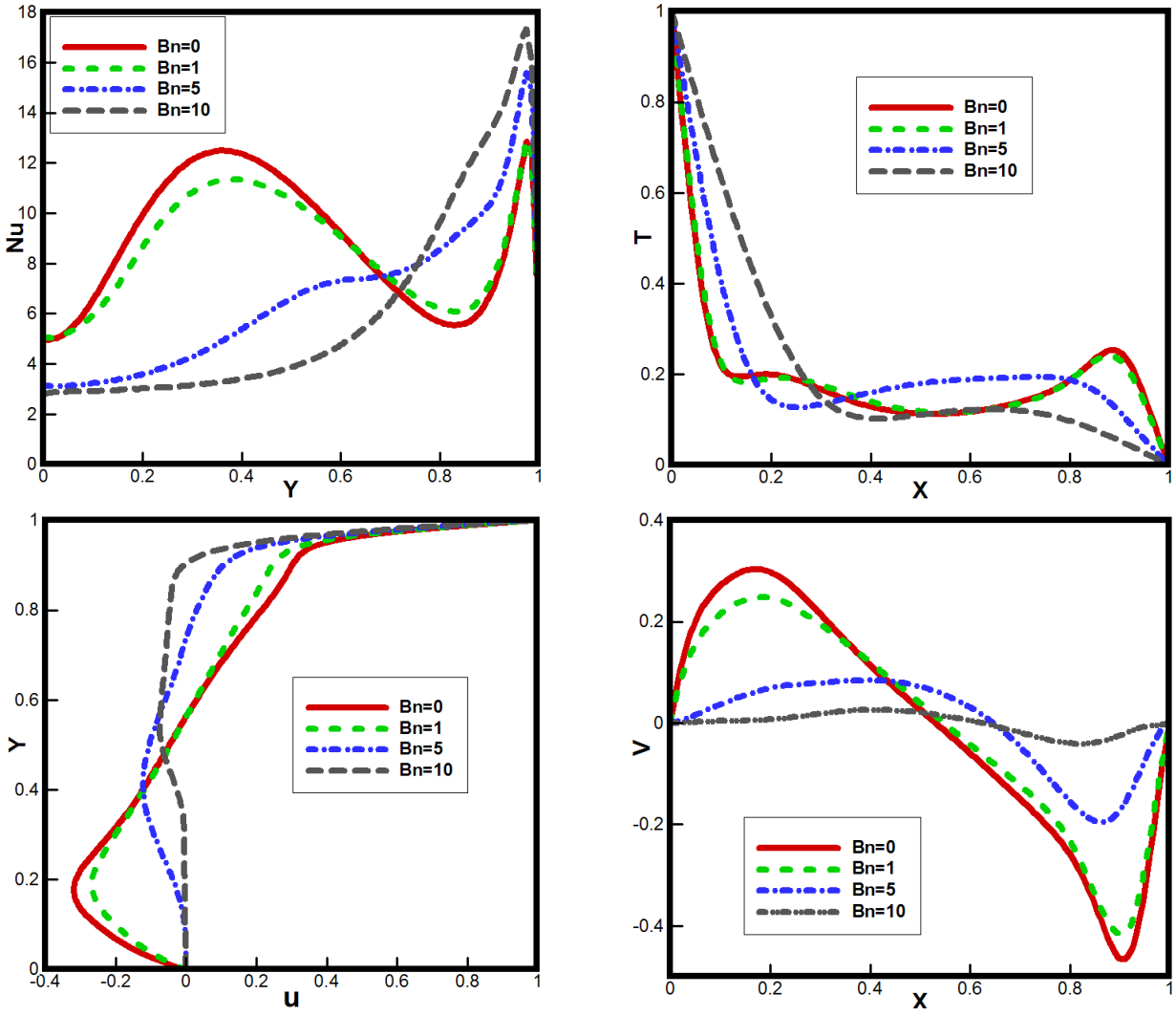

Fig. 5.24 Vertical velocity (v) and temperature distribution (T) at $y = 0.5$, horizontal velocity profile (u) at $x = 0.5$ and the local Nusselt number at the hot wall for different Reynolds and Bingham numbers at Pr = 1 and Re=1000·

and therefore heat transfer enhances. However, it can be observed that the Prandtl number alterations do not create significant changes in the streamlines. In fact, the Prandtl number just influences the flow field in the added force term in Eq. (5.4.14), for the temperature modification affects it. The absence of the Prandl number parameter in the shear stresses in Eqs. (5.4.13 - 5.4.14) causes the unyielded/yielded zones to be the same for various Prandtl numbers. However, the Reynolds number has a crucial role in the shapes of the unyielded regions; see Eqs. (5.4.13 - 5.4.14), in contrast with the natural convection in which the Prandtl number plays the significant role. That is, the Prandtl number affects the streamlines and unyielded/yielded zones only in natural convection significantly; cf. Huilgol (2015) and Turan et al. (2010).

Next, the figure 5.26 reveals the velocity, temperature and local Nusselt number profiles for different Prandtl numbers at Bn = 10 and Re = 100 using the Papanastasiou model with the regularisation parameter $m = 1000$. As mentioned earlier, the Prandtl number influences the vertical velocity with the added force term while the horizontal one is not affected by this parameter (Eq. 5.4.14). These trends are evident in the velocity distributions in the middle of the cavity clearly. The horizontal velocity is nearly the same for different Prandtl numbers while its increase diminshes the vertical velocity drastically. In contrast, the temperature profile curves with the rise of the Prandtl number demonstrating the increase in the convection process. The local Nusselt number also exhibits this pattern for it drops considerably with the enhancement of the Prandtl number although the trend is stronger between Pr = 1 to 10.

The Table 5.9 lists the average Nusselt number and the dimensionless average Nusselt number for various Bingham, Reynolds and Prandtl numbers using the Papanastasiou model with the regularisation parameter $m = 1000$. In typical engineering process calculations, the mean value of the Nusselt number is often required either to estimate the rate of heat transfer between the fluid and the heated surface, or conversely, to evaluate one of the temperatures if the heat flux is known from other considerations. The mean Nusselt number is expected

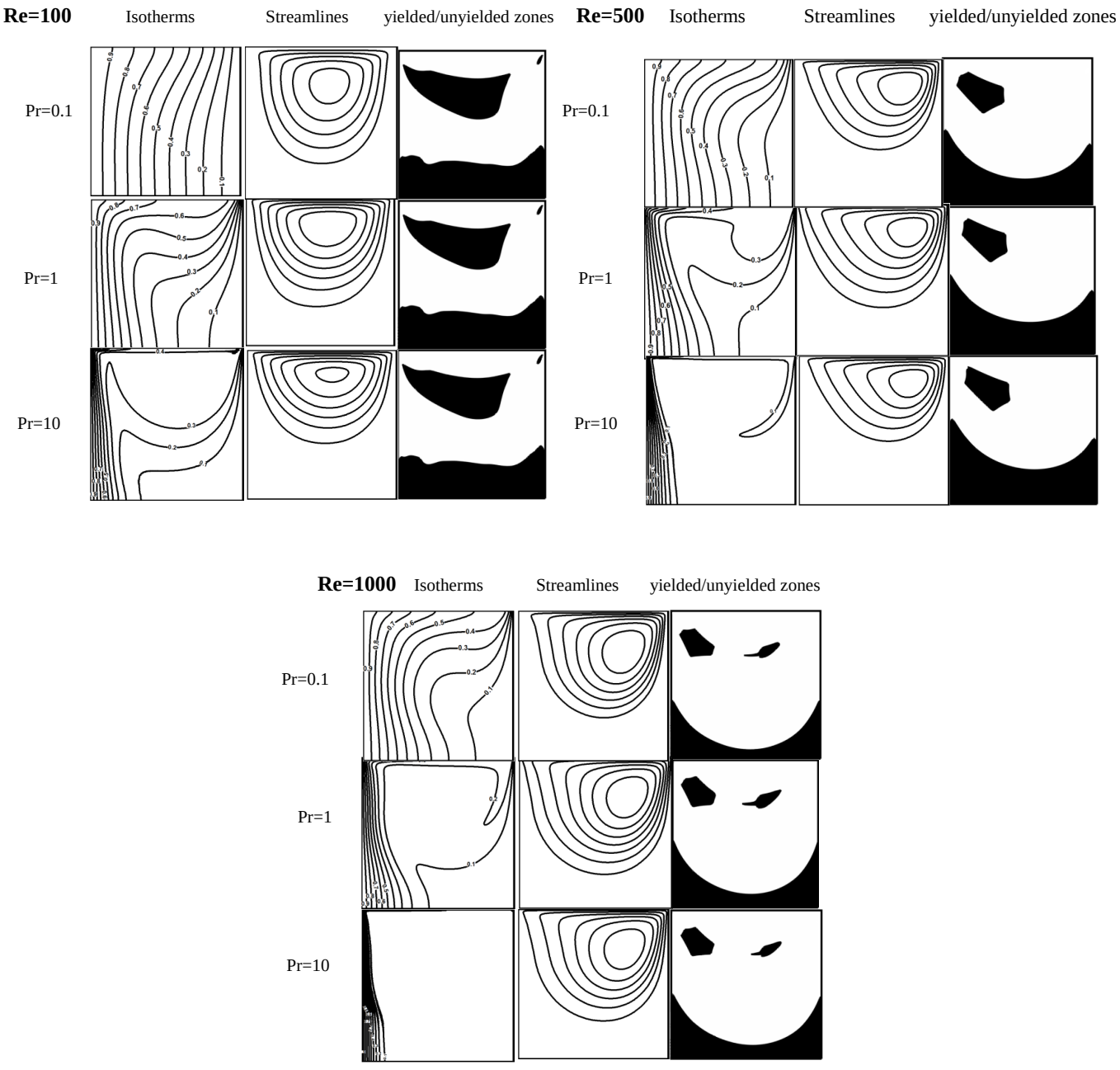

Fig. 5.25 Comparison of the streamlines for different Reynolds and Bingham numbers at Pr = 1·

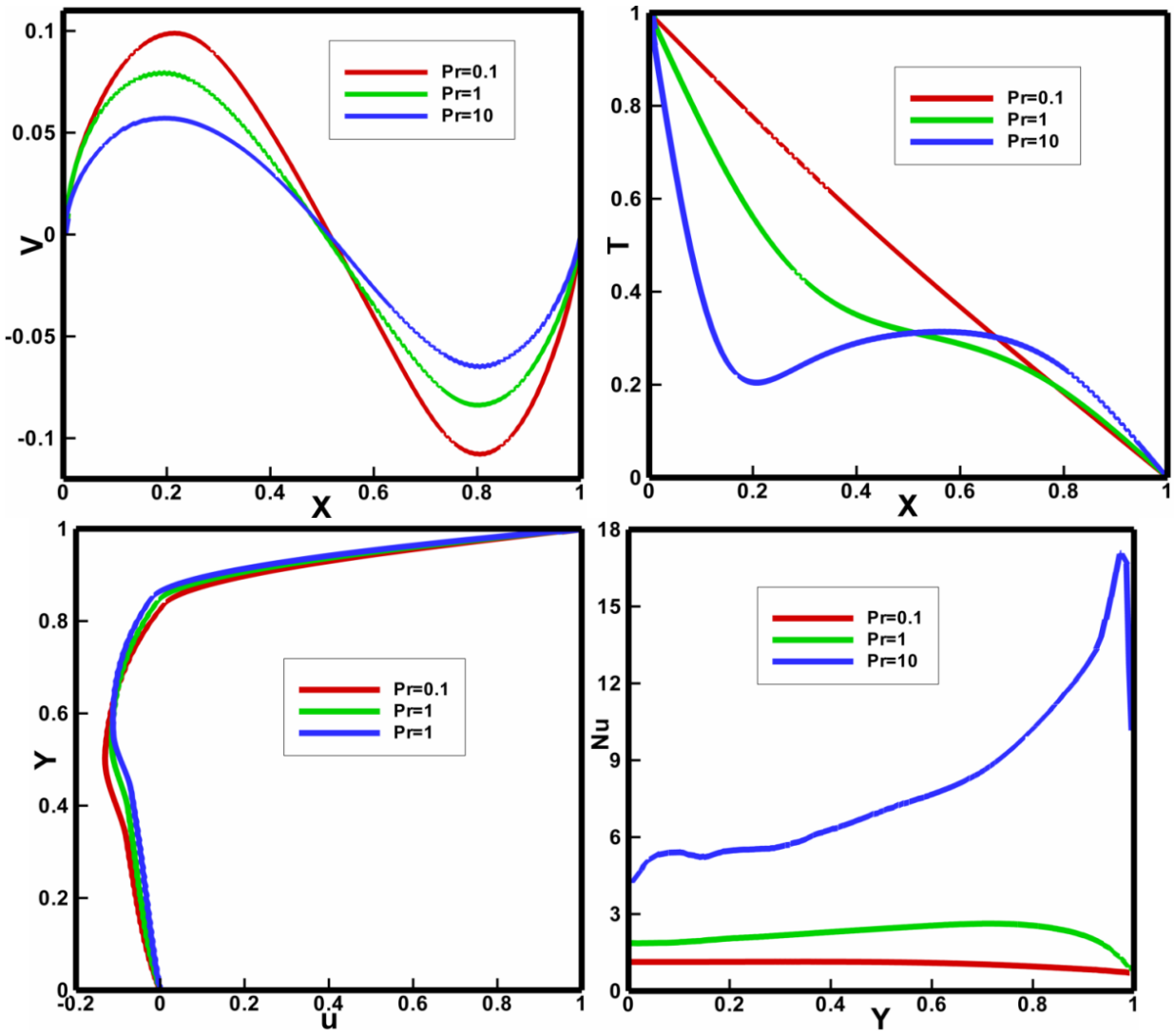

Fig. 5.26 Comparison of the streamlines for different Reynolds and Bingham numbers at Pr = 1·

to be a function of the Reynolds number (Re), the Prandtl number (Pr), and the Bingham number (Bn), offering the reason behind the calculation of the average Nusselt number over a wide ranges of these parameters. The average Nusselt number shows that the heat transfer increases with the rise of the Reynolds number generally. Furthermore, it demonstrates that the rise of the Bingham number decreases the heat transfer markedly. Moreover, the results in Table 5.9 show that the heat transfer increases with the enhancement of the Prandtl number for multitudinous Reynolds and Bingham numbers. However, the effect of the Bingham number on the decrease in heat transfer is different for various Reynolds and Prandtl numbers as shown by the dimensionless average Nusselt numbers. It is obvious the least effect of the Bingham number on the drop of heat transfer is obtained at Pr = 10 for different Reynolds numbers. At Re = 500 and 1000, the increase in the Prandtl number causes the influence of the Bingham number on heat transfer to decrease in general.

Finally, the Table 5.10 shows that the average Nusselt number does not change considerably as the regularisation parameter is altered. Hence, the regularisation parameter of the Papanastasiou model does not play a crucial role in the rate of heat transfer and the size of the yielded/unyielded zones, when the parameter m is varied between 100 and 1000; see Figs. 7 and 8 as well.

Table 5.9 Comparison of the average Nusselt number and dimensionless average Nusselt number on the hot wall for different Reynolds, Bingham and Prandtl numbers

Nu_{avg}		Pr = 0.1	Pr = 1	Pr = 10	$Nu_{avg}*$	Pr = 0.1	Pr = 1	Pr = 10
Re = 100								
	Bn = 0	1.3029	3.33921	9.2580		1	1	1
	Bn = 1	1.2346	3.1330	8.7821		0.9476	0.9382	0.9486
	Bn = 5	1.0941	2.5078	7.7273		0.8379	0.7510	0.8347
	Bn = 10	1.0537	2.2385	7.7126		0.8087	0.6704	0.8331
Re = 500								
	Bn = 0	2.3469	6.4231	17.8781		1	1	1
	Bn = 1	2.1510	6.0129	16.9603		0.9165	0.9361	0.9866
	Bn = 5	1.500	4.6243	13.9534		0.6391	0.7199	0.7805
	Bn = 10	1.3495	4.3866	13.9534		0.5750	0.6829	0.7654
Re = 1000								
	Bn = 0	3.2552	8.9140	24.1483		1	1	1
	Bn = 1	3.0916	8.5491	22.9788		0.9497	0.9591	0.9516
	Bn = 5	2.1668	6.5581	18.6648		0.6656	0.7357	0.7729
	Bn = 10	1.7301	5.9815	17.7998		0.5315	0.6710	0.7371

Table 5.10 Comparison of average Nusselt number for various regularisation parameters (m) and Bingham numbers (Bn)

Bn = 10				
	m	100	500	1000
	Nu_{avg}	4.3783	4.3866	4.3866

5.4.7 Concluding Remarks

The mixed convection of a Bingham fluid in a lid-driven cavity has been analysed by the Thermal Finite Difference Discrete Flux Method (TFDDFM) based on the Lattice Boltzmann Method (LBM). The present study has been conducted with the main parameters lying in the following ranges: the Reynolds number, Re = 100 to 1000, the Bingham number between Bn = 0 and 10, the Prandtl number from Pr = 0.1 to 10 while the Grashof number is fixed at Gr = 10000. In addition, a comparison between the predictions of the Bingham model and the

Papanastasiou model has been made.This investigation is performed for various values of the mentioned parameters and the conclusions are summarised as follows:

a) The agreement with the previous numerical investigations demonstrates that the applied method is appropriate for the studied problem.

b) The enhancement of the Reynolds number increases the heat transfer for different Prandtl and Bingham numbers and causes the yielded/unyielded sections to alter.

c) The rise of the Prandtl number augments the heat transfer while it does not influence the yielded/unyielded zones.

d) The augmentation of the Bingham number reduces the heat transfer and increases the unyielded section in the cavity.

e) The least effect of the Bingham number on heat transfer is observed at Pr = 10 among the studied Prandtl numbers.

f) The comparison between the Bingham model and the Papanastasiou model demonstrates that divergences exist between the predictions of the two models when the Bingham number is large, which is as expected.

References

Abdelkhalek, M. (2008). Mixed convection in a square cavity by a perturbation technique. *Comp. Mater. Sci*, 42:212–219.

Aposporidis, A., Haber, E., Olshanskii, M. A., and Veneziani, A. (2011). A mixed formulation of the Bingham fluid flow problem: Analysis and numerical solution. *Comput. Methods Appl. Mech. Engrg.*, 200:2434–2446.

Atkinson, C. and El-Ali, K. (1992). Some boundary value problems for the Bingham model. *J. Non-Newt. Fluid Mech.*, 41:339–363.

Bercovier, M. and Engelman, M. (1980). A finite-element method for incompressible non-newtonian flows. *J. Comput. Phys.*, 36:313–326.

Bhatnagar, P. L., Gross, E. P., and Krook, M. (1954). A priori derivation of the lattice Boltzmann equation. *Phys. Rev. Ser. 2*, 94:511–525.

Bingham, E. (1922). Fluidity and Plasticity. McGraw-Hill, New York.

Blazek, J. (2001). Computational Fluid Dynamics: Principles and Applications, pp. 347–350. Elsevier, Amsterdam.

Botella, O. and Peyret, R. (1998). Benchmark spectral results on the lid-driven cavity flow. *J Comput Phys*, 27:421–433.

Boyd, J., Buick, J., and Green, S. (2006). A second-order accurate lattice Boltzmann non-Newtonian flow model. *Journal of Physics A*, 39:14241–14247.

Bruneau, C. and Jouron, C. (1990). An efficient scheme for solving steady incompressible Navier-Stokes equations. *J Comput Phys*, 89:389–413.

Buick, J. (2009). Lattice Boltzmann simulation of power-law fluid flow in the mixing section of a single-screw extruder. *Chem. Eng. Sci.*, 64:52–58.

Cebeci, T., Shao, J. P., Kafyeke, F., and Laurendeau, E. (2005). Computational Fluid Dynamics for Engineers, pp. 311–320. Springer-Verlag, New York.

Chenoweth, D. and Paolucci, S. (1985). Gas flow in vertical slots with large horizontal temperature differences. *Phys. Fluids*, 28:2365–2374.

Chenoweth, D. and Paolucci, S. (1986). Natural convection in an enclosed vertical air layer with large horizontal temperature differences. *J. Fluid Mech.*, 169:173–210.

Damianou, Y. and Georgiou, G. C. (2014). Viscoplastic Poiseuille flow in a rectangular duct with wall slip. *J. Non-Newt. Fluid Mech.*, 214:88–105.

Damianou, Y., Kaoullas, G., and Georgiou, G. C. (2015). Cessation of viscoplastic Poiseuille flow in a square duct with wall slip. *J. Non-Newt. Fluid Mech.*, (In press):1–14.

Davis, P. J. and Rabinowitz, P. (1984). Methods of Numerical Integration. *Academic Press,New York*.

de Vahl Davis, G. (1983). Natural convection of air in a square cavity: a bench mark numerical solution. *Int. J. Numer. Meth. Fluids.*, 3:249–264.

Dean, E. and Glowinski, R. (2002). Operator-splitting methods for the simulation of Bingham visco-plastic flow. *Chin. Ann. Math.*, 23B:187–204.

Dean, E. J., Glowinski, R., and Guidoboni, G. (2007). On the numerical simulation of Bingham visco-plastic flow: Old and new results. *J. Non-Newt. Fluid Mech.*, 142:36–62.

Deng, G. B., Piquet, J., Queutey, P., and Visonneau, M. (1994). Incompressible-flow calculations with a consistent physical interpolation finite-volume approach. *Computers and Fluids*, 23:1029–1047.

Dimakopoulos, M., Pavlidis, M., and Tsamopoulos, J. (2013). Steady bubble rise in Herschel-Bulkley fluids and comparisons of predictions via the augmented Lagrangian method with those via the Papanastasiou model. *J. Non-Newt. Fluid. Mech.*, 200:34–51.

Dubois, F. (2008). Equivalent partial differential equations of a lattice Boltzmann scheme. *Comp. Math. Appl.*, 55:1441–1449.

Dubois, F. (2009). Third order equivalent equation of lattice Boltzmann scheme. *Discrete Cont. Dyn. Syst.*, 23:221–248.

Dubois, F. and Lallemand, P. (2009). Towards higher order lattice Boltzmann scheme. *J. Stat. Mech.*, doi:10.1088/1742-5468/2009/06/P06006.

Duvaut, G. and Lions, J. L. (1972). Transfert de chaleur dans un fluide de Bingham dont la viscosité dépend de la température. *J. Funct. Anal.*, 11:93–110.

Duvaut, G. and Lions, J.-L. (1976). Inequalities in Mechanics and Physics. Springer-Verlag, New York.

Fortin, M. and Glowinski, R. (1983). Augmented Lagrangian Methods: Applications to the Numerical Solution of Boundary-Value Problems. North-Holland, Amsterdam.

Frigaard, I. (1998). Stratified exchange flows of two Bingham fluids in an inclined slot. *J. Non-Newt. Fluid Mech.*, 78:61–87.

Frisch, U., d'Humeres, D., Hasslacher, B., Lallemand, P., Pomeau, Y., and Rivet, J.-P. (1987). Lattice gas hydrodynamics in two and three dimensions. *Complex Syst*, 1:649–707.

Frisch, U., Hasslacher, B., and Pomeau, Y. (1986). Lattice-gas automata for the Navier-Stokes equations. *Phys. Rev. Lett.*, 56:1505–1510.

Fu, S. C. and So, R. M. C. (2009). Modeled Lattice Boltzmann Equation and the Constant Density Assumption. *AIAA Journal*, 47:3038–3042.

Fu, S. C., So, R. M. C., and Leung, R. M. C. (2012). Linearized-Boltzmann-type-equation-based fnite difference method for thermal incompressible flow. *Computers and Fluids*, 6:67–80.

Gabbanelli, S., Drazer, G., and Koplik, J. (2005). Lattice Boltzmann method for non-Newtonian (powerlaw) fluids. *Phys. Rev E*, 72:046312.

Gartling, D. K. and Hickox, C. B. (1985). A numerical study of the applicability of the Boussinesq approximation for a fluid saturated porous medium. *Int. J. Numer. Meth. Fluids*, 5:995–1013.

Ghia, U., Ghia, K. N., and Shin, C. T. (1982). High-Reynolds number solutions for incompressible flow using the Navier-Stokes equations and a multigrid method. *J Comput Phys*, 48:387–411.

Glowinski, R. (1984). Numerical Methods for Nonlinear Variational Problem. Springer-Verlag, New York.

Glowinski, R. (2003). Finite element methods for incompressible viscous flow. In Ciarlet, P. and Lions, J., editors, *Handbook of Numerical Analysis*, volume 9, pp. 3–1176. Elsevier, Amsterdam.

Gray, D. D. and Giorgini, A. (1976). The validity of the Boussinesq approximation for liquids and gases. *Int. J. Heat Mass Transfer*, 19:545–551.

Guo, Z., Shi, B., and Wang, N. (2000). Lattice BGK model for incompressible Navier-Stokes equation. *J. Comp. Phys.*, 165:288–306.

Guo, Z., Shi, B., and Zheng, C. (2002). A coupled lattice BGK model for the Boussinesq equations. *Int. J. Numer. Methods Fluids*, 39:325–342.

Hardy, J., Pomeau, Y., and de Pazzis, O. (1973). Time evolution of a two-dimensional classical lattice system. *Phys. Rev. Lett*, 31:276–280.

He, X. and Luo, L.-S. (1997). A priori derivation of the lattice Boltzmann equation. *Phys.Rev. E*, 55:R6333–R6336.

Hou, S., Zou, Q., Chen, S., Doolen, G., and Cogley, A. (1995). Simulation of cavity flow by the lattice Boltzmann method. *J. Comput. Phys.*, 118:329–347.

Huilgol, R. R. (2006). A systematic procedure to determine the minimum pressure gradient required for the flow of viscoplastic fluids in pipes of symmetric cross-section. *J. Non-Newt. Fluid Mech.*, 136:140–146.

Huilgol, R. R. (2009). On the definition of pressure in rheology. *Rheol. Bull.*, 78(2):12, 14–15, 29.

Huilgol, R. R. (2015). Fluid Mechanics of Viscoplasticity. Springer, Berlin Heidelberg.

Huilgol, R. R. and Kefayati, G. H. R. (2015). Natural convection problem in a Bingham fluid using the operator-splitting method. *J. Non-Newt. Fluid Mech.*, 220:22–32.

Huilgol, R. R. and Panizza, M. (1995). On the determination of the plug flow region in Bingham fluids through the application of variational inequalities. *J. Non-Newt. Fluid Mech.*, 58:207–211.

Huilgol, R. R. and You, Z. (2005). Application of the augmented Lagrangian method to steady pipe flows of Bingham, Casson, and Herschel–Bulkley fluids. *J. Non-Newt. Fluid Mech.*, 128:126–143.

Huilgol, R. R. and You, Z. (2009). Prolegomena to variational inequalities and numerical schemes for compressible viscoplastic fluids. *J. Non-Newt. Fluid Mech.*, 158:113–126.

Iwatsu, R., Hyun, J., and Kuwahara, K. (1993). Mixed convection in a driven cavity with a stable vertical temperature gradient. *Int.J. Heat and Mass Transfer*, 36:1601–1608.

Junk, M., Klar, A., and Luo, L.-S. (2005). Asymptotic analysis of the lattice Boltzmann equation. *J. Comp. Phys.*, 210:676–704.

Junk, M. and Yong, W.-A. (2003). Rigorous Navier-Stokes limit of the lattice Boltzmann equation. *Asymptotic Analysis*, 35:165–186.

Karimfazli, I., Frigaard, I. A., and Wachs, A. (2015). A novel heat transfer switch using the yield stress. *J. Fluid Mech.*, 783:526–566.

Kennedy, P. and Zheng, R. (2013). Flow Analysis of Injection Molds, pp. 10–20. Hanser, Munich.

Khanafer, K., Al-Amiri, A., and Pop, I. (2007). Numerical simulation of unsteady mixed convection in a driven cavity, using an externally excited sliding lid. *Eur. J. Mech. B-Fluid*, 26:669–687.

Khanafer, K. and Chamkha, A. (1999). Mixed convection flow in a lid-driven enclosure filled with a fluid-saturated porous medium. *Int.J. Heat and Mass Transfer*, 42:2465–2481.

Lallemand, P. and Luo, L.-S. (2003). Theory of the lattice Boltzmann method: Acoustic and thermal properties in two and three dimensions. *Phys. Rev E*, 68:036706.

Lax, P. D. and Wendroff, B. (1960). Systems of conservation laws. *Comm. Pure Appl. Math.*, 13:217–237.

Li, C.-H. and Glowinski, R. (1996). Modelling and numerical simulation of low-Mach number compressible flows. *Int. J. Numer. Meth. Fluids*, 23:77–103.

McNamara, G. and Zanetti, G. (1988). Use of the Boltzmann equation to simulate Lattice-Gas Automata. *Phys. Rev. Lett*, 20:2332–2335.

Mendes, P. R. S. and Dutra, E. E. S. (2004). Viscosity function for yield-stress liquids. *Appl. Rheol.*, 14:296–302.

Mitsoulis, E. (2007). Flows of viscoplastic materials: Models and computations. *Rheology Reviews*, 2007:135–178.

Mitsoulis, E. and Zisis, T. (2001). Flow of Bingham plastics in a lid-driven square cavity. *J. Non-Newtonian Fluid Mech.*, 101:173–180.

Mosolov, P. and Miasnikov, V. (1965). Variational methods in the theory of the fluidity of a viscous-plastic medium. *PMM, J. Mech. Appl. Math.*, 29:545–577.

Mosolov, P. and Miasnikov, V. (1966). On stagnant flow regions of a viscous-plastic medium in pipes. *PMM, J. Mech. Appl. Math.*, 30:841–854.

Mosolov, P. and Miasnikov, V. (1967). On qualitative singularities of the flow of a viscoplastic medium in pipes. *PMM, J. Mech. Appl. Math.*, 31:609–613.

Moyers-Gonzalez, M. and Frigaard, I. (2004). Numerical solution of duct flows of multiple visco-plastic fluids. *J. Non-Newt. Fluid Mech.*, 12:227–241.

Muravleva, L. (2015). Uzawa-like methods for numerical modeling of unsteady viscoplastic Bingham medium flows. *Appl. Numer. Math.*, 93:140–149.

Nejat, A., Abdollahi, V., and Vahidkhah, K. (2011). Lattice Boltzmann simulation of non-Newtonian flows past confined cylinders. *J. Non-Newt. Fluid. Mech.*, 166:689–697.

Neofytou, P. (2005). A 3rd order upwind finite volume method for generalised Newtonian fluid fows. *Adv. Eng. Softw.*, 36:664–680.

O'Donovan, E. J. and Tanner, R. I. (1984). Numerical study of the Bingham squeeze film problem. *J. Non-Newt. Fluid Mech.*, 15:75–83.

Ohta, M., Nakamura, T., Yoshida, Y., and Matsukuma, Y. (2011). Lattice Boltzmann simulations of viscoplastic fluid flows through complex flow channels. *J. Non-Newt. Fluid Mech.*, 166:404–412.

Olshanskii, M. A. (2009). Analysis of semi-staggered finite-difference method with application to Bingham flows. *Comput. Methods Appl. Mech. Engrg.*, 198:975–985.

Papanastasiou, T. C. (1987). Flow of materials with yield. *J. Rheol.*, 31:385–404.

Patankar, S. V. (1981). A calculation procedure for two-dimensional elliptic situations. *Numer. Heat Transfer*, 4:409–425.

Patankar, S. V. and Spalding, D. B. (1972). A calculation procedure for heat, mass and momentum transfer in three-dimensional parabolic flows. *Int. J. Heat Mass Transfer*, 15:1787–1806.

Pham, T. and Mitsoulis, E. (1998). Viscoplastic flows in ducts. *Can. J. Chem. Eng.*, 76:120–125.

Psihogios, J., Kainourgiakis, M., Yiotis, A., Papaioannou, A., and Stubos, A. K. (2007). A lattice Boltzmann study of non-Newtonian flow in digitally reconstructed porous domains. *Trans. Porous Media*, 70:279–292.

Quéré, P. L. (1991). Accurate solutions to the square thermally driven cavity at high Rayleigh number. *Computers & Fluids*, 20:29–41.

Quéré, P. L. and de Roquefort, T. A. (1985). Computation of natural convection in two-dimensional cavities with Chebyshev polynomials. *J. Comput. Phys.*, 57:210–228.

Rajagopal, K. R. and Srinivasa, A. R. (2005). On the nature of constraints for continua undergoing dissipative processes. *Proc. R. Soc.*, A461:2785–2795.

Rivlin, R. S. and Ericksen, J. L. (1955). Stress deformation relations for isotropic materials. *J. Rational Mech. Anal.*, 4:323–425.

Sahin, M. and Owens, G. R. (2003). A novel fully implicit finite volume method applied to the lid-driven cavity problem: High Reynolds number flow calculations. *Int. J. Numer. Meth. Fluids*, 42:57–77.

Sanchez, F. (1998). Application of a first-order operator splitting method to Bingham fluid flow simulation. *Comput. Math. Appl.*, 36:71–86.

Santos, D., Frey, S., Naccache, M., and Mendes, P. (2011). Numerical approximations for flow of viscoplastic fluids in a lid-driven cavity. *J. Non-Newt. Fluid Mech.*, 166:667–679.

Saramito, P. and Roquet, N. (2001). An adaptive finite element method for viscoplastic flows in pipes. *Comput. Methods Appl. Mech. Eng.*, 190:5391–5412.

Sharif, M. (2007). Laminar mixed convection in shallow inclined driven cavities with hot moving lid on top and cooled from bottom. *Appl. Therm. Eng.*, 27:1036–1042.

Sullivan, S., Gladden, L., and Johns, M. (2006). Simulation of powerlaw fluid flow through porous media using lattice Boltzmann techniques. *J. Non-Newt. Fluid. Mech.*, 133:91–98.

Sullivan, S., Sederman, A., Johns, M., and Gladden, L. (2007). Verification of shear thinning lb simulations in complex geometries. *J. Non-Newt. Fluid. Mech.*, 143:59–63.

Syrakos, A., Georgiou, G. C., and Alexandrou, A. N. (2013). Solution of the square lid-driven cavity flow of a Bingham plastic using the finite volume method. *J. Non-Newt. Fluid Mech.*, 195:19–31.

Syrakos, A., Georgiou, G. C., and Alexandrou, A. N. (2014). Performance of the finite volume method in solving regularised Bingham flows: inertia effects in the lid-driven cavity flow. *J. Non-Newt. Fluid Mech.*, 208-209:88–107.

Tang, G., Wang, S., Ye, P., and Tao, W. (2011). Bingham fluid simulation with the incompressible lattice Boltzmann model. *J. Non-Newt. Fluid Mech.*, 166:145–151.

Tanner, R. I. (2000). Engineering Rheology. 2nd Ed. Oxford University Press, Oxford.

Taylor, A. and Wilson, S. (1997). Conduit flow of an incompressible yield stress fluid. *J. Rheol.*, 41:93–101.

Tiwari, R. and Das, M. (2007). Heat transfer augmentation in a two-sided lid-driven differentially heated square cavity utilizing nanofluids. *Int.J. Heat and Mass Transfer.*, 50:2002–2018.

Toro, E. F. (1999). Riemann solvers and numerical methods for fluid dynamics: a practical introduction. 2nd Ed. Springer-Verlag, New York.

Turan, O., Chakraborty, N., and Poole, R. (2010). Laminar natural convection of Bingham fluids in a square enclosure with differentially heated side walls. *J. Non-Newt. Fluid Mech.*, 165:901–913.

Turan, O., Chakraborty, N., and Poole, R. (2012). Laminar Rayleigh-Bénard convection of yield stress fluids in a square enclosure. *J. Non-Newt. Fluid Mech.*, 171-172:83–96.

Turan, O., Poole, R., and Chakraborty, N. (2011). Aspect ratio effects in laminar natural convection of Bingham fluids in rectangular enclosures with differentially heated side walls. *J. Non-Newt. Fluid Mech.*, 166:208–230.

Vikhansky, A. (2010). On the onset of natural convection of Bingham liquid in rectangular enclosures. *J. Non-Newt. Fluid Mech.*, 165:1713–1716.

Vola, D., Boscardin, L., and Latche, J. (2003). Laminar unsteady flows of Bingham fluids: a numerical strategy and some benchmark results. *J. Comput. Phys.*, 187:441–456.

Waheed, M. (2009). Mixed convective heat transfer in rectangular enclosures driven by a continuously moving horizontal plate. *Int.J. Heat and Mass Transfer*, 52:5055–5063.

Wang, C. and Ho, J. (2008). Lattice Boltzmann modeling of Bingham plastics. *Physica A*, 387:4740–4748.

Wang, Y. (1998). Axial flow of generalized viscoplastic fluids in non-circular ducts. *Chem. Eng. Commun.*, 168:13–43.

Welander, P. (1954). On the temperature jump in a rarefied gas. *Ark. Fysik*, 7:507–5553.

Wolfram, S. (1986). Cellular automaton fluids 1: Basic theory. *J. Stat. Phys.*, 45:471–526.

Yoshino, M., Hotta, Y., Hirozane, T., and Endo, M. (2007). A numerical method for incompressible non-Newtonian fluid flows based on the lattice Boltzmann method. *J. Non-Newt. Fluid. Mech.*, 147:69–78.

Zhang, J. (2010). An augmented Lagrangian approach to Bingham fluid flows in a lid-driven square cavity with piecewise linear equal-order finite elements. *Comput. Methods Appl. Mech. Engrg.*, 199:3051–3057.

Zou, Q. and He, X. (1997). On pressure and velocity boundary conditions for the lattice Boltzmann BGK model. *Phys. Fluids*, 9:1591–1598.

Appendix A

The non-dimensional constant r^*

From the constitutive equation Eq. (5.2.1), we see that the tensor $\mathbf{\Lambda}$ is dimensionless. Thus, from Eq. (5.2.6), where the projection operator $P_{\mathscr{M}}$ is defined, we see that $r\tau_y\mathbf{A}(\mathbf{v})$ must be non-dimensional. Since $\mathbf{A}(\mathbf{v})$ is of dimension $U/L = t^{-1}$, where t denotes time, one can find quite easily that r has the dimension $M^{-1}Lt^3$. The question is how one can define this constant r. From Eq. (5.2.15), we have the following:

$$\mathrm{Bn} = \frac{\sqrt{2}\tau_y L}{\eta U}, \quad \mathrm{Ra} = \frac{g\beta\rho L^3\delta T}{\alpha\eta}, \quad \mathrm{Pr} = \frac{\eta c_p}{k}. \tag{A.0.1}$$

It is easy to show that

$$\mathrm{Bn}\cdot\mathrm{Pr} = \frac{c_p}{k}\cdot\frac{\sqrt{2}\tau_y L}{U}. \tag{A.0.2}$$

Obviously,

$$\frac{k}{c_p}\cdot\frac{\mathrm{Bn}\cdot\mathrm{Pr}}{\sqrt{2}}\cdot\frac{U^2}{L^2} = \tau_y\frac{U}{L}. \tag{A.0.3}$$

Here, the Bingham and Prandtl numbers are dimensionless. Since $U = \sqrt{gL\beta\delta T}$, we find that $r\tau_y(U/L)$ is dimensionless if

$$r = \frac{\sqrt{2}c_p}{k}\cdot\frac{L^2}{U^2} = \frac{\sqrt{2}c_p}{k}\cdot\frac{L}{g\beta\delta T}. \tag{A.0.4}$$

When we want to replace τ_y by Bn, and $\mathbf{A}(\mathbf{v})$ by its non-dimensional version, we begin with $\nabla_{\mathbf{x}}\mathbf{v}$ and obtain that it is equal to $(U/L)\nabla_{\mathbf{x}^*}\mathbf{v}^*$, where the latter gradient is of zero dimension. See Eq. (5.2.16) in this connection.

Thus, in Eq. (5.2.26), we need

$$r\tau_y\mathbf{A}(\mathbf{u}) = r\tau_y(U/L)\mathbf{A}^*(\mathbf{u}^*) = r^*\mathrm{Bn}\mathbf{A}^*(\mathbf{u}^*), \tag{A.0.5}$$

from which it follows that

$$r^* = \frac{\eta U^2}{\sqrt{2}L^2}r = \frac{\eta U^2}{\sqrt{2}L^2}\cdot\frac{\sqrt{2}c_p}{k}\cdot\frac{L}{g\beta\delta T} = \frac{\eta c_p}{k} = \mathrm{Pr}. \tag{A.0.6}$$

That is, the constant r^* in Eq. (5.2.26) is the Prandtl number.

Appendix B

Publications

In this Appendix, the first pages of the three journal articles are attached.

Journal of Non-Newtonian Fluid Mechanics 220 (2015) 22–32

Contents lists available at ScienceDirect

Journal of Non-Newtonian Fluid Mechanics

journal homepage: http://www.elsevier.com/locate/jnnfm

Natural convection problem in a Bingham fluid using the operator-splitting method

R.R. Huilgol *, G.H.R. Kefayati

School of Computer Science, Engineering and Mathematics, Flinders University of South Australia, GPO Box 2100, Adelaide, SA 5001, Australia

ARTICLE INFO

Article history:
Received 3 April 2014
Received in revised form 3 June 2014
Accepted 11 June 2014
Available online 24 June 2014

Keywords:
Natural convection
Bingham fluid
Operator-splitting method
Cavity flow

ABSTRACT

In this paper, natural convection in a square cavity with differentially heated vertical sides and filled with a Bingham fluid has been studied without any regularisation. The finite element method (FEM) based on the operator splitting method is utilised to solve the problem. This study has been conducted for the pertinent parameters in the following ranges: Rayleigh number $Ra = 10^3$–10^5 and the Prandtl number between 0.1 and 10. Moreover, the Bingham number is studied in wide ranges for different Prandtl and Rayleigh numbers. Results indicate that the heat transfer increases with the enhancement of the Rayleigh number, with a decrease in the size of the unyielded zones. For specific Rayleigh and Prandtl numbers, the increase in the Bingham number decreases the heat transfer. Furthermore, as expected, the growth of the Bingham number expands the unyielded sections in the cavity. Finally, for fixed Rayleigh and Bingham numbers, the unyielded regions grow with the augmentation of the Prandtl number. Comparisons with the previously published work, based on the augmented Lagrangian method, and the bi-viscosity model respectively are made.

1. Introduction

For nearly three decades, it has been recognised that the buoyancy-driven flow in a square cavity with vertical sides which are differentially heated is a bench mark problem [1] for testing and validating numerical schemes for a wide variety of practical problems such as ventilation of rooms, air flow inside a combustion engine, crystal growth, nuclear reactors, and electronic cooling devices, to name a few. This natural convection problem has inspired much research, especially since 1983, in the field of Newtonian and power-law fluid mechanics.

For instance, de Vahl Davis [1] adopted the stream function-vorticity formulation and obtained some benchmark solutions using a second-order finite difference scheme as well as the Richardson extrapolation. The results in the Rayleigh number range $Ra = 10^3 - 10^6$ were presented. Subsequently, Le Quéré and Alziary de Roquefort [2], and Le Quéré [3] produced their solutions to the same problem but with a totally different method, i.e., the semi-implicit Chebyshev spectral method. Chenoweth and Paolucci [4,5] employed an explicit predictor–corrector finite difference method on the staggered grid to examine the gas motion in a cavity, including the effect of the aspect ratio A ($1 \leqslant A \leqslant 10^2$). Barakos et al. [6] studied both laminar and turbulent flows in the cavity using a finite volume approach for $Ra = 10^3$–10^{10}. Zienkiewicz et al. [7] developed a characteristic-based split algorithm combined with the finite element method and applied it to the square cavity flow. The non-uniform structured mesh was used in their computation. More recently, Gjesdal et al. [8] performed spectral element simulations on both square and rectangular cavities. For square cavity problem, some results under $Ra = 10^4$–10^8 were listed. El-Amrani and Seaïd [9] used a semi-Lagrangian Galerkin-characteristic method on the natural convection problem in a square cavity and compared results with those from Eulerian-based Galerkin finite element solvers. They provided results in the range $Ra = 10^3$–10^8.

In a similar vein, Lamsaadi et al. [10–12] have examined the flow of power law fluids in vertical and tilted rectangular slots, and when the fluid is subjected to both horizontal and vertical uniform heat fluxes. More recently, Turan et al. [13] have studied the convection problem for a power law fluid in a square cavity.

While the above methods are eminently suitable for solving the cavity flow problems for a variety of Boussinesq incompressible fluids under steady conditions, they cannot be applied directly to the flows of viscoplastic fluids. The main reason is that in the flows of Bingham and other yield stress fluids, the flow domain is decomposed into two disjoint regions: one where the fluid has yielded

* Corresponding author.
E-mail addresses: Raj.Huilgol@flinders.edu.au (R.R. Huilgol), Gholamreza.kefayati@flinders.edu.au (G.H.R. Kefayati).

http://dx.doi.org/10.1016/j.jnnfm.2014.06.005
0377-0257/

Journal of Non-Newtonian Fluid Mechanics 233 (2016) 146–154

Contents lists available at ScienceDirect

Journal of Non-Newtonian Fluid Mechanics

journal homepage: www.elsevier.com/locate/jnnfm

From mesoscopic models to continuum mechanics: Newtonian and non-newtonian fluids

R.R. Huilgol*, G.H.R. Kefayati

School of Computer Science, Engineering and Mathematics, Flinders University of South Australia, GPO Box 2100, Adelaide, SA 5001, Australia

ARTICLE INFO

Article history:
Received 1 September 2015
Revised 2 March 2016
Accepted 3 March 2016
Available online 22 March 2016

Keywords:
Lattice Boltzmann equation
BGK approximation
Particle distribution function
Continuum mechanics

ABSTRACT

A review of the BGK approximation to obtain the equations of motion for an incompressible fluid is presented and its drawbacks are revealed. In order to overcome these inherent problems, new models for the particle distribution functions are needed. Using the Finite Difference Lattice Boltzmann Method (FDLBM) due to Fu and So (2009) [1] and the Thermal Difference Discrete Flux Method (TDDFM) proposed by Fu et al. 2012 [2], it is shown that the newer distribution functions lead to the mass conservation equation, the equations of motion and the energy balance equation for incompressible fluids in two dimensions, employing the D2Q9 lattice as the model. This derivation is extended to compressible fluids as well. Next, using the D3Q15 lattice as an example, the three dimensional equations of continuum mechanics are derived. Since no restrictions are placed on the constitutive equations, the theoretical development applies to all fluids, whether they be Newtonian, or power law fluids, or viscoelastic and viscoplastic fluids. Finally, some comments are offered regarding the numerical scheme to calculate the particle distribution functions to determine the velocity and temperature fields.

1. Introduction

From the Lattice Boltzmann equation, it is possible to derive the continuity equation and Cauchy's equations of motion for a compressible medium, when one uses the Bhatnagar–Gross–Krook (BGK) approximation. From this, one can obtain equations relevant to incompressible fluids. However, these require that the pressure be proportional to the density and the viscosity be dependent on the collision relaxation time [3]; see Section 2 below. Clearly, these restrictions on the pressure and the viscosity are unacceptable in modeling the flows of non-Newtonian, incompressible fluids.

In order to overcome these inherent problems, new models for the particle distribution functions are needed. In the Finite Difference Lattice Boltzmann Method (FDLBM) due to Fu and So [1], the particle distribution function leads to the conservation of mass and the equations of motion applicable to incompressible fluids, when the flows are assumed to occur in a two dimensional setting underpinned by a D2Q9 lattice. Our derivation of these results is succinct and is more transparent, for it uses vector analysis and linear algebra. In addition, the energy equation is also obtained from the Thermal Difference Discrete Flux Method (TDDFM) proposed by Fu et al. [2]; once again, simple results from vector analysis and linear algebra are employed. The important point to note is that the previous restrictions on the pressure and the viscosity are eliminated in these derivations, meaning that one is free to choose a constitutive equation. That is, one can model a Newtonian fluid, or power law fluids, or viscoelastic and viscoplastic fluids. Moreover, we point out in Section 3 that it is quite easy to incorporate Dirichlet type boundary conditions into the numerical scheme to determine the particle distribution functions for the velocity and temperature fields.

In Section 4, the method is extended to the flows of all fluids in three dimensions, using the D3Q15 lattice as an example. Once again, the particle distribution functions are such that every type of fluid, compressible or incompressible, can be employed.

Finally, in Section 5, some remarks are offered on the numerical scheme employed to determine the particle distribution functions for the velocity and the temperature fields. The CFL condition for the stability of the numerical scheme is also derived.

2. BGK approximation to continuum mechanics

Beginning in 1986, Lattice Boltzmann equation (LBE) models evolved from their Boolean counterparts, viz., the lattice-gas-automata. The theoretical framework of the LBE was underpinned by the Chapman–Enskog analysis of the LGA models (Frisch et al [4,5]; Wolfram [6]). That is, the statistical mechanics of the LGA played a crucial role in these developments. A decade later, He and

* Corresponding author. Tel.: +61882012938.
E-mail address: Raj.Huilgol@flinders.edu.au (R.R. Huilgol).

http://dx.doi.org/10.1016/j.jnnfm.2016.03.002
0377-0257/

International Journal of Heat and Mass Transfer 103 (2016) 725–743

Contents lists available at ScienceDirect

International Journal of Heat and Mass Transfer

journal homepage: www.elsevier.com/locate/ijhmt

Lattice Boltzmann Method for simulation of mixed convection of a Bingham fluid in a lid-driven cavity

G.H.R. Kefayati *, R.R. Huilgol

School of Computer Science, Engineering and Mathematics, Flinders University of South Australia, GPO Box 2100, Adelaide, SA 5001, Australia

ARTICLE INFO

Article history:
Received 23 June 2016
Received in revised form 28 July 2016
Accepted 28 July 2016

Keywords:
Mixed convection
Bingham fluid
Lid-driven cavity
Lattice Boltzmann Method

ABSTRACT

In this paper, a two-dimensional simulation of steady mixed convection in a square enclosure with differentially heated sidewalls has been performed when the enclosure is filled with a Bingham fluid. The problem has been solved by the Bingham model without any regularisations and also by applying the regularised Papanatasiou model. An innovative approach based on a modification of the Lattice Boltzmann Method (LBM) has been applied to solve the problem. Yield stress effects on heat and momentum transport using the Papanatasiou model are investigated for certain pertinent parameters of the Reynolds number (Re = 100, 500, and 1000), the Prandtl number (Pr = 0.1, 1, and 10) and the Bingham number (Bn = 0, 1, 5 and 10), when the Grashof number is fixed at Gr = 10,000. Results show that a rise in the Reynolds number augments the heat transfer and changes the extent of the unyielded section. Furthermore, for fixed Reynolds and Prandtl numbers, an increase in the Bingham number decreases the heat transfer while enlarging the unyielded section. Although an increase in the Prandtl number enhances heat transfer, it does not affect the proportions of the unyielded/yielded regions in the cavity. Finally, the results of the Bingham and Papanatasiou models are compared and it is found that there is a visible difference between the two models especially in the yielded/unyielded sections.

1. Introduction

Convection involving both free and forced convection is generally referred to as mixed convection, which occurs when buoyancy effects are superposed on a forced flow. Mixed convection in fluid-filled square cavities plays an important role in the area of heat and mass transfer and has been given a considerable attention over the past several years due to the wide variety of applications in science and engineering [1–7]. For example, the flow is present in materials processing, flow and heat transfer in solar ponds, dynamics of lakes, reservoirs and cooling ponds, crystal growing, float glass production, metal casting, food processing, galvanizing, and metal coating. However, most of the research has been limited to incompressible Newtonian fluids, although in a few cases, non-Newtonian fluids have also been considered. Viscoplastic fluids form a special sub-class of non-Newtonian fluids in which the flow field is divided into two regions: the first is an unyielded zone where the fluid is at rest or undergoes a rigid motion, and the second where the fluid flows like a viscous liquid. In the unyielded zone, the second invariant of the extra stress is less than or equal to the yield stress and in the yielded region, this invariant exceeds the yield stress. Thus, the location and shape of the yield surface(s), i.e. the interface between these two sets, is also a part of the solution of flow problems of such fluids. This is a challenging problem and research has been divided into using the Bingham model without any regularisations, or the modification due to Papanastasiou [8], or the bi-viscosity model due to O'Donovan and Tanner [9].

Here, we solve the flow of a Bingham fluid in a lid driven square cavity with differentially heated sidewalls using a new numerical approach, based on the Lattice Boltzmann Method (LBM). This technique is applied to the Bingham model and the Papnasatasiou model so that a comparison between their predictions can be made. As far as the LBM is concerned, it has been demonstrated to be a very effective mesoscopic numerical method to model a broad variety of complex fluid flow phenomena. It has developed into an alternative powerful numerical solver for the Navier–Stokes (N–S) equations applicable to incompressible Newtonian fluids. In comparison with traditional methods in the field, the LBM algorithms are much easier to implement, especially in complex geometries and multi-component flows. This is because the main equation of the LBM is hyperbolic and can be solved locally, explicitly, and efficiently on parallel computers. However, it has had to overcome three main drawbacks in passing from the compressible to incompressible models. The first one arises

* Corresponding author.
E-mail addresses: gholamreza.kefayati@flinders.edu.au (G.H.R. Kefayati), Raj.Huilgol@flinders.edu.au (R.R. Huilgol).

http://dx.doi.org/10.1016/j.ijheatmasstransfer.2016.07.102
0017-9310/